POLITECNICO DI TORINO

Corso di Laurea Magistrale in Ingegneria Civile

FINITE ELEMENT ANALYSIS OF THE STRUCTURAL BEHAVIOUR OF THE PORTREATH HARBOUR WALL UNDER WAVE LOADING

Relatore:

Prof.ssa Cecilia Surace (Politecnico di Torino)

Correlatori:

Prof.ssa Alison Raby (University of Plymouth)

Dr Dassa Dassanayake (University of Plymouth)

Ing. Rinto Roy (Politecnico di Torino)

Candidato:

Luigi Figliomeni

Dicembre 2019

a mia Madre e a mio Padre,

per Tutto

Abstract

The Portreath Harbour wall is today what remains of the vital Portreath Harbour, one of the busiest harbours of Cornwall in the past. The structure was damaged during a storm in 2014, which washed away the iconic Monkey Hut at the top of the wall, and again in 2018 when storm Eleanor completely destroyed the toe of the structure. Repair works were undertaken during the years, which rebuilt the Monkey Hut, the destroyed part of the wall and increased the stiffness of the structure. In this work, a study of the Portreath harbour wall structural behaviour under wave loading is presented.

After the review of an appropriate literature, a preliminary investigation of the structure's material and of the geometry has been conducted by an in situ survey. Particularly, a Schmidt hammer test was performed. Analysis has been carried out by creating a FEM model of both the damaged parts of the wall and results were analysed and discussed.

For the model of the front of the wall, which regards the part damaged in 2014, a 3D model of the structure was created and both blocks and mortar were modelled. It has been found that the collapse was due to a progressive damage of the masonry. Indeed, the highest storm wave generated stresses below the material strength properties.

For the part damaged in 2018, a parametric study was conducted in order to define the failure load. Since no wave theories were applicable in that part, a CFD analysis was run and the actual wave load was calculated. Again, it was below the failure load. The failure load was also used for testing the rebuilt wall.

The study is a preliminary work and further investigation with appropriate theories are required for a better understanding.

List of Contents

List of Figures

List of Tables

Introduction

Harbour wall around the England coast have been suffering the impact of the waves for years. Over the course of time the material degradation has increased giving rise to fairly severe damage to these iconic structures making currently necessary to intervene in order to recover them.

Harbour walls on the British coast are of importance for the protection of the village. For example, in the case of Portreath, a village on the north coast of Cornwall, in England. The village extends along both sides of a stream valley and is centred on the harbour and beach. The Portreath harbour was one of Cornwall's most important and busiest port and nowadays is within the UNESCO Cornish Mining World Heritage site. Particularly, the harbour wall protects homes and business in Portreath against the risk of flooding. For this reason, it has a very important strategic meaning as well as being an historical monument for the region.

In its history the harbour wall has been damaged many times by waves and in addition to the economic damage there have been many social consequences. Recently, the Portreath harbour wall was damaged by significant waves by a storm in January 2014 (Cornwall Council, 2014). The storm caused severe external damage to the wall, assaulted by 10 meters high waves. It emerged that huge volumes inside the structure had become vacated due to tide action and aggregate wash out. Natural abrasion of the material and wave action caused the loss of the wall structural thickness. As consequence a few areas of the wall surface were found to be weak. The waves also destroyed the Monkey Hut above the wall, now rebuilt again. The structure losses and the total repair were estimated to have cost £500,000. CORMAC undertook the work and additional blocks were added on top of those high damaged already in place to increase the defence. The strengthening and consolidation of the structure required injection grouting (shotcrete) on the wall and other operations were planned to exclude the water from the structure prior to grouting it (ICE, 2016).

Nevertheless, as reported by BBC (2018) and Cornwall Live (2018), in 2018 the wall was damaged again and the last 20 meters toward the village collapsed during Storm Eleanor and some 12 meters square of masonry was displaced and pressed back into the core of the wall. The repair works estimated to cost £990,000. On the collapsed part, CORMAC built a new reinforced concrete wall and covered it with stone to hold with the current wall (CORMAC, 2018; Environment Agency, 2018).

A study of the harbour wall is so vital to improve its defence. The aim of this dissertation is to analyse and evaluate the structural behaviour of the Portreath harbour wall under dynamic loading arising from waves, through a Finite Element analysis. To achieve it, the following objectives have been set:

- identify all the geometrical properties of the wall and the useful information about the soil;
- determine the material properties of the block by in situ test and empirical correlations;
- create a FE model as close as possible to the actual wall using all the information obtained in the previous points and choosing the right discretization and the appropriate support conditions;
- estimate a conceivable value for the wave loading using an appropriate theory;

- extract from the FE model all the information about the behaviour of the harbour wall under that load and the most critical scenarios;
- predict all the hypothetical future scenarios on the harbour wall and indicate possible interventions.

In order to create an FEM model it has been necessary to investigate the geometry of the wall and its material properties. The geometry was acquired from data provided by the Environment Agency (drawing) and by the LIDAR data from the Coastal Channel Observatory. Using a GIS software (ArcMap) all the sections of the harbour wall have been obtained. An in-situ survey confirmed the found geometry. The material properties have been determined by a Schmidt hammer test on the wall. Analysis started from a first rough model of a generic section of the wall in order to find the worst load case for its structural behaviour and they led to a finer final model. Results were analysed and discussed on the basis of an appropriate literature review.

1. Literature review

Wolters et al (2004) investigated pressure pulses, induced by wave impact, and their transmission through an air-water field into cracks and fissures of coastal structures at large model and field scale. The study was carried out on the Admiralty breakwater on the Island of Alderney and large-scale model tests in the Large Wave Channel (GWK) in Hanover. A detailed description of the two cases is reported in the publication.

As claimed by the authors, especially in old coastal structures, the wave impact and its propagation in the material introduces high pressures into cracks and fissures. Indeed, the water travelling inside the crack of marine structure causes a pressure difference between the impact face and the interior of the structure. That pressure difference creates the seaward expulsion of several blocks.

According to their experimental results, the impact pressure has a very localized nature: the pressure value can change from the ambient value to the peak one over distances from 0.2 to 0.4m. Because of this, coastal structures are vulnerable to wave attack but only in few locally weakened zones. Obviously, the wave impact pressures change in time. Usually the wave impact moves up the wall over time. It has been seen that the highest pressure value recorded was 3.5 MPa, with the pressure time history increasing to this maximum in a relatively slow time of around 0.5 ms. The pressure value inside the crack is usually close to the external one in the impact area. Differences in the values can be found in the case of impact waves with a high rapidly rising impact pressure.

Considering the Alderney experiment, it has been observed how the wave impact pressure enters by the water in the crack. The pressure in the crack is generally higher than the pressure at the crack entrance and for a long time the pressure pulsations are continued within the crack. The impact pressure effect is transformed within the cracks into a softer, extended periodic pulsation. Variations in breaker shape could create big changes in the pulsation characteristic.

The pressure rise time changes with pressure in the cracks and the front wall. Usually a higher aeration content is associated with a longer pressure rise time.

In the GWK case, one of the most important observation is that the wave pressure that enter in the crack is strongly attenuated by values up to 90%. This is due to the rise time of the pressure and to the boundary condition on the front of the wall that create an energy dissipation (turbulence at the wall, geometrical and acoustic spreading, etc.). Once the pressure enters in the crack, the dissipation is drastically reduced. The lower is the impact pressure and the bigger are the pressure losses. Anyway, the crack pressure is strongly non-linear and the pressure value is about 150 to 300 times the hydrostatic water pressure.

Usually the higher values of pressure are either at the crack entrance or at the crack end with the same order of magnitude while it is very unusual to find the largest pressure in the middle of the crack because of the attenuation of the pressure pulsation along the crack. In the GWK experiment it has been seen how the results change with the crack dimension. In small cracks (1mm) the pressure is almost completely attenuated within the crack reaching an almost zero pressure value at the crack end. However, in bigger cracks (10mm) the pressure can be amplified within the crack reaching at the crack end values up to 200% of the one at the crack entrance. In the Alderney experiment, at the crack end it has always been noted that the pressure is bigger than at the crack entrance by up to 33%.

After a wave impact on the front wall, the water that enters into the crack acts a seaward/outward pressure bigger than the one acting in the front wall. This is because on the front wall the pressure has already diminished while inside the crack the propagated impulse has still a high intensity. On that way, an outward pressure gradient is created. This gradient can be the reason why the block are removed seaward. A lasting seaward pressure can be found also after few hundreds of milliseconds from the initial impact. A formulation for calculate the maximum breaking wave induced pressure at the end of a crack is proposed by the authors.

Within the crack, the pressure propagation velocity is quite variable due to the different filled condition inside the cracks: completely or partially filled with water; moreover, the water inside the crack can have different degrees of aeration due to the turbulence at the crack entrance. Impact pressure, by compressing the air in the water, increases the bulk modulus of the air-water material with an increasing of the propagation speed. It has been observed that the variation of the aeration degree and its percentage is higher in the smaller crack because of the capillary force within the crack which retain the air.

In conclusion, the study says that different scale effects have to be considered. The most important of these is the nonlinearity in the pulse propagation which is due to the crack aeration, filling conditions and variation in water compression due to an impact loading. In summary:

- Wave impact has as consequence a pressure pulse propagation into structural filled crack
- Pressure pulse propagation velocity depends on crack size, water depth and water aeration. High values can be reached (hundreds of kPa) and they are of longer duration than the impact pressure
- Scale effect have to be considered (the variation between the reality values and the one obtained from this study have a nonlinear behaviour)

Bullock's study on the same masonry breakwater in Alderney outs many investigations on the effect of air on wave effects in coastal structure. See Bird et al (1998) for all the experiment and equipment description.

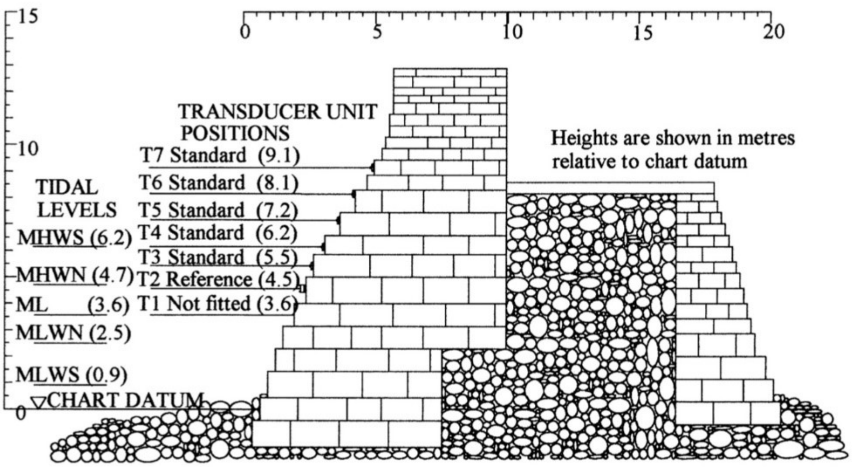

Figure 1.1. Admiralty Breakwater with the transducer used in the experiment (Bullock et al, 2001)

According to Bullock et al (2000) a wave impact can be divided into 2 parts: an initial impulsive one (with a high impact pressure of short duration) followed by a quasi-static part (with lower pressure during a longer time). It has been seen how the magnitude and the rise time of the impact pressure are linked to the air entrapped in the water wave. Particularly, the higher the value of the air in the water, the longer is the rise time of the impact pressure while the magnitude is, on the contrary, lower.

In summary the results showed that the maximum pressure decreases with the level of aeration. The results may change between fresh water and seawater: generally, the bubbles formed in seawater are smaller than those generated in freshwater. The biggest bubble in freshwater tends to coalesce and so there are less bubbles overall while the salt tends to stabilise bubbles in seawater. However, even a small air percentage might lead to a consistent reduction in peak pressures. Anyway, it can be said that fresh and seawater waves caused the same overall impulsive load on the structure. The results also shown that there is a quick reduction in void ratio just before the extreme impact pressure is achieved. It can be assumed that air, rather than water, is responsible for the initial increase in pressure. It might be thought that air-water interaction could cause unexpected behaviour on breakwater. The initial impact has a slower rise and as soon as the water enters in contact with the aeration units the signal falls fast.

The impact on a wall created by waves which break on it is very larger considering the impact due to non-breaking waves. The biggest impact pressure occurs when the front of the breaker is parallel to the wall at the impact time. The impact pressure is very localised in both space and time. If the wave breaks on the wall, it can trap an air pocket while if the wave has already broken a high percentage of air can be entrained and a turbulent air-water combination hits the wall. In both cases, the air affects the dynamic of the structure by reducing the maximum pressure. On the other way, the air can also distribute the impact in wider way that might increase the impulse (Bullock et al, 2007).

The authors divided the wave impacts in 4 families:

- slightly-breaking wave impact. It represents the transition between near breaking waves and well established impact conditions;
- Low-aeration impact. It is characterised by high peak pressures and short rise time and pressure spike localised in both space and time. In that case the wave crest turns over slightly and traps a small pocket of air;
- High-aeration impact. It is characterised by a higher level of trapped air pocket and pressure spike are less localised. Because of the air cushioning effect, it can be found a longer rise time. After the pressure peak, that impact shows a sub-atmospheric pressure and, because of the time leg in the propagation of wave impact pressures within crack, a pressure differential is established. Consequently, huge seaward forces can be produced with a resulting removal of the blocks from the masonry structure. The alternate air compression and expansion generate damped oscillations in both pressure and void ratio;
- Broken wave impact. In that case, the wave breaks before it reaches the structure producing a highly aerated turbulent bore. Over the usual pressure variation there is a superposition of high frequency fluctuations due to the oscillation of small bubbles.

The highest force is associated with the low-aeration impact. Anyway, high impact pressure can occur despite the presence of significant quantities of air. Generally, the higher impact pressures have been seen when the breaking waves trapped a small pocket of air. However, an important air quantity does not avoid the generation of high pressures. Slightly-breaking waves seem less probable to generate significant impulses than broken waves. The study also shows how the highest pressure was generated by a low-aeration impact and most of the other impacts produced pressures considerably below the highest. Low-aeration impact were found to occur more often that high-aeration impact. Moreover, the research observes how an introduction of a slope in the wall can significantly reduce the maximum force on a wall, while the impulses do not change significantly.

In the case of aerated wave impact a particular event called “flip-through” impact is seen: the jet up the wall ‘flips’ through the fast closing gap between the overturning crest and the wall and so the front of the wave and the wall, in this impact, never make direct contact. That impact type is associated with a high acceleration and huge pressure that moves up the wall. The study found that as the height of the wall increase the first violent impact will be of the flip-through form with slight air entrapment while the time of maximum pressure is almost identical for all the wall elevations. High pressures spread away from the impact zone as a pressure wave with a more or less semi-circular front. It can be said that impulses increase monotonically with the wave height over a height of 1.45 meters. For higher values, the increase in the impulse is due to the trend of the force peak to growth with the size of the trapped air pocket (Bredmose et al, 2009).

Violent breaking waves usually happen when previous events have already caused the entrainment of a significant volume of air in the water and further air may well be trapped between the wave and the structure against which it breaks. Maximum impact pressure is highly sensitivity to wave conditions, and it is very high in the impact zone. Pressure waves can propagate down from the impact zone causing high pressure at the base of the structure. Once the wave reaches the free surface, it goes through a reflection and a dissipating wave returns back toward the mound. The pressure wave that moves down the wall might develop into a shock wave for bigger wall dimensions. As the wall scale increases the air pocket becomes more compressed and the maximum impact pressure increases with respect to the predicted values.

Air escape causes an initial decline in the air pocket oscillations. Bubbles smaller than 2 mm in diameter were unlike to break up. After the main peak there are oscillatory fluctuations in pressure. The response changes as a function of the scale. At small scale the air pocket has very little influence in the scaling effect because of its relatively high stiffness. The impact pressure propagates down the wall more rapidly at large scale. Except for the smallest scale, the high-aeration impact are larger than for the flip-through and low-aeration impact. For larger values of initial aeration, the positive impact pressures that propagates down the wall compensate the negative air pocket pressures. Deviations may be caused by an increasing of the Mach number for the aerated water (Bredmose et al, 2015).

The surrounding water, because of its aeration, can reduce the maximum pressure because it will be quasi-static in shape at the time of maximum compression (the air pocket is otherwise deformable). In this circumstance, the aeration of the surrounding water will still cushion the large pressure at the air-water interface like on a rigid wall. Both the impact pressure and the Mach number depend on scale and aeration. Some combinations of impact type, scale and aeration, can lead to resonance between the air pocket oscillations and the reflected pressure waves. So higher pressure values than those caused by the original impact may follow. Aeration brought a decrease in the impact pressure while the effect of scale keeps and eventually increase the Froude scaled impact pressures.

Latham et al (2008) conclude the review in this study. Their work focuses on a rubble-mound breakwater covered by armour layer of concrete units. Using a FEM (Finite Element Method) program the structural response of the unit, under static and dynamic loading condition, has been studied. In order to capture also the multi-body loading of all the contacts existing, a DEM (Discrete Element Method) model has been linked. In the FEMDEM method, FEM formulation simulate continuum deformations while DEM formulations simulate the multi-body interaction. The structural integrity of concrete armour under dynamic and extreme loading conditions was examined by applying a new three dimensional fracture model (Guo et al, 2014). The whole structure was modelled considering a multi-body system in which each discrete body was a discrete element and was further discretised into a finite element mesh. Elements were linked by joint element defined by the Mohr-Coulomb criterion.

Figure 1.2. Breakwater covered by Dolosse units (Guo et al, 2015)

For the DEM model, a multi-sphere approach was adopted: a small sphere replaces each surface voxel of a given particle. The particles can interact via contact forces only when the surface spheres of different particles overlap. The connectivity between components making up the solid frame is not improved by changing the shapes. On the other hand, a higher porosity associated with the shape would allow greater penetration of water into the breakwater and consequently, turbulence dissipative effects may be more effective. DEM does not allow shape deformations (assumption of rigid body).

It has been observed that units develop a pull out force approximately from 1.8 to 8 times their weight. Cross elements showed a higher pull out force with respect to the cubic ones. Tensile spalling cracks can develop in the walls and base of bottom arm with a small chance of important compressive shear cracking and the probability that damage does not being transferred to the whole unit. Compressive strength of the concrete unit is able to support the dynamic stresses while the tensile strength is usually smaller respect to the tensile stresses that arise after an impact. This led to spalling cracks with a lot of damage in the impact area but without transmission to the whole unit of further damage. Anyway the unit might become useless after the impact. The study also makes it easy to understand why units at the base of a structure are carrying too high stresses while other units are carrying very low ones.

The authors showed how the fracture propagation first starts from pre-existing surface crack tips in the upper stem-fluke corner, afterwards in the lower corner with consequently bigger area of new fractures in the upper corner than the lower corner. Moreover, surface cracks do not have an important effect on the material strength but they can affect the long term durability of the units. Most of the fractures are caused by a combination of excessive tensile stresses and differential stresses; all the fractures are initiated by collision, and they are always accompanied by energy loss. The packing density is one of the main parameters that influences the stability of an armour layer though unit orientation may also influence it (Anastasaki et al, 2015).

Waves on structures may be simulated more realistically by coupling the FEMDEM model (in which the wave impact is simplified as a cyclic load and forces are applied in order to simulate the wave effects) with a CFD (Computational Fluid Dynamics) model which simulates the actual wave action. One mesh is used across the whole solution domain on which the fluids equations are solved and the second mesh contains a finite element representation of the solid structures. In order to simulate the damage of breakwaters during a storm, adaptive mesh will track the armour units. FEMDEM analysis are required when stresses within concrete units are important and angular and faceted shapes are involved (Latham et al, 2009).

Loraoux (2013) studied the dynamic behaviour of La Jument lighthouse in France under wave load. It has been observed that the response of the structure depends on the pressure loading time and that a sudden change of behaviour occurs when that time goes from 0.05s to 0.1s. Very rapid loading times cause strong accelerations on the structure, but which are safe for the wall, while very slow loading times cause large oscillations that can damage the structure. Oscillations can also make the cracks to close and open continually. The stiffness of the structure falls after the first wave and decreases again with much stronger waves

2. The Portreath harbour wall

Portreath was one of the earliest ports in Cornwall. The harbour history, reported by the Portreath Harbour Association (2019), starts in 1713 when Samuel Nott was engaged to build a quay. It is unknown when and how it was destroyed, but from that quay only the foundation remains today completely under the sand.

The harbour that we can see today was begun in 1760 consequently to the developing ore industry in the area: Portreath became a viable port. By 1800 there was a need to expand the port. The outer basin was excavated in 1801 to provide additional space. The part of the harbour wall toward the see, the long pier and the Monkey Hut at its end, was built in 1824 to protect vessels entering the port extending the rest of the wall previously built (The Quarterly Journal for British Industrial and Transport History, 1994). In 1837 the port was connected to the Portreath branch of the Hayle Railway and increased traffic required the building of a second basin. The inner basin was added in 1846 while in the late 1860s the new basin was constructed. In order to convey ore from Poldice mine to the harbour at Portreath, a tram road was built. By the 1840s Portreath was handling about 700 shiploads per year. In 1886 Portreath was made a free port and the harbour's business amounted to £10,000 (British Railway Journal, 1990). These numbers have been diminishing in the years especially after the copper trade collapse that led Portreath to the bankrupt in 1886. However timber and other mining materials were still imported and so the port survived. In that time also the fishing industry was growing. In 1887 David Wise Brain started building up his own fleet of steamers and the importance of the port in the 19th century led to development of ship building and at least 14 vessels were built there. Following the depression of the 1920s and growing competition from rail and road transport, the port had all but ceased to trade by the 1960s.

The harbour was property of the Beynon Shipping Company until June 1980 when it was donated to the current Cornwall Council from whom the Portreath Harbour Association rent the basin, slipway, docks and hard-standing along with the boat shed and the bait hut.

Figure 2.1. Historical photo in about 1905 (The Quaterly Journal for British Industrial and Transport History, 1994)

2.1. Structure description

The wall is characterised by a first part (toward the sea) 60 meters long. At the beginning of that part, on the top of the wall, there is the so called Monkey Hut historically used for housing by the harbour pilots who would wave flags or lanterns to guide ships into harbour, or advise if conditions were too unsafe. The thickness goes from a value of 6 m on the top to a value of 10 m at the base. After the first part, the wall has a slight reduction in the thickness and a change in the direction as shown in Figure 2.1.1. The length of the second part of the wall is 116 m. At the end, there is a third part where the thickness decreases further and the direction changes again. The third part forks into two parts. The part labelled as *3rd b* was completely destroyed by Storm Eleanor in 2018 and it was rebuilt by CORMAC in the same year. At the end of the wall there is the harbour basin.

Figure 2.1.1. Maps of the site (Earth 3D Map, 2019)

Along the first part and the most of the second part of the wall there is an outcropping rock on the edge of the wall. The whole wall stands completely clear from the water during the low tide and in the same way the basins are empty. The tide tables published by the Portreath Harbour Association show that the water lever can rise up to 7 m during the high tide. The wall is therefore subjected to a constant variation of the water level during the day and the months. The seaweed on the top of the wall and Figure 2.1.2 demonstrate that the entire structure is usually wet.

On May 17^{th} 2019 a field trip was taken to the site. The aim of the visit was to:

- check the geometry of the wall (height and thickness). Rough values of the geometry were already available by the LIDAR data of the wall. A survey was carried out with a total station using middle point between the car parking and the beach. The survey confirmed the values reported above.
- check the geometry of the blocks and the thickness of the mortar. The survey showed that the geometry of the blocks is irregular. The block dimensions in the front of the pier go from 0.69 to 1.75 m large and to 0.59 to 0.8 m high. In the same way, the mean value of the mortar thickness is between 1 to 2 cm. For this purpose a tape was used.
- Identify Young's modulus of blocks and mortar using the Schmidt Hammer. For this part see the paragraph 2.2.

Figure 2.1.2. Wave height during a storm (Portreath Harbour Association, 2019)

The first part of the wall is made of 9 courses of blocks and, although the block dimensions change slight block by block, the material is completely uniform. Looking at Figure 2.1.3 it is possible to see how the the blocks are linked by strips of metal. Those strips are applied only on the front of the face and in a few blocks on the higher part of the side and they are 52 cm long and 5 cm wide. The aim of the strips is to link the blocks; in one location it is possible to see it goes at least 5 cm into the block. In the same part there are apparently random holes, probably used to install scaffolfing. Most of them are now empty while in a few others there is rebar inside. The holes are 13 cm deep and 4 cm wide.

The second part of the wall is characterized by large irregularities in the material in respect to the first part (see Figure 2.1.7). Same irregularities are also evident between the left and the right side of the wall as shown in Figure 2.1.8. Differencies between the two parts might be explained considering their two different construction times. Moreover, Figure 2.1.9 shows how a few areas repared after the storm damages, are made of concrete. Almost two different concrete ages have been found. This underlines how the repairs were done at different times. In this part, the blocks used in the first part are alternate with regularity with different black blocks using a different arrangement of the one used in the other part. In Figure 2.1.9 it is shown how the materials were used and alternated. Overall, the top coarses are uniform, while the bottom sections are more vertically arranged. The concrete parapet on the top was detached by the waves and it is possible to find the concrete blocks on the ground. On this part the strips are only between the top 3 courses.

Figure 2.1.3 Front face of the wall, location A (Portreath Harbour Association, 2019)

Figure 2.1.4 First part of the wall

In Figure 2.1.4 it is possibile to see the vertical water marks along the wall caused by the tide and, for the top part of the structure, the red spots due to the corrosion of the metal strips in the top courses. The last row of blocks is actually a parapet. Seaweed is diffused along all the wall. In the photo it is possible to see also the outcropping rock. A second concrete parapet (almost destoyed) complete the wall. The parapet goes around the Monkey

Hut. It is worth to observe how the parapet was damaged between the time at which Figure 2.1.3 was taken and the day of the field trip (Figure 2.1.4). How it is shown in the Figure 2.1.5, there is a concrete base between the Monkey Hut (made of masonry) and the top part of the wall.

Figure 2.1.5 Detail of the Monkey Hut

Figure 2.1.6. Material degradation

Figure 2.1.7 Differences between the second and the first part of the wall

In Figure 2.1.6 it is possible to see the superficial degradation of the block. A superficial layer of small seashell is diffused along the whole structure. Looking at Figure 2.1.8 it is evident how the block degradation is higher in the lower course which are the weakest one, especially in the part of the wall with an irregular block arrangement because of the wider concrete and mortar part. The blocks in the top part of the wall appears with a white halo. A huge weak area is observable also at the central top part of Figure 2.1.3. For more datail about the block see paragraph 2.2.2.

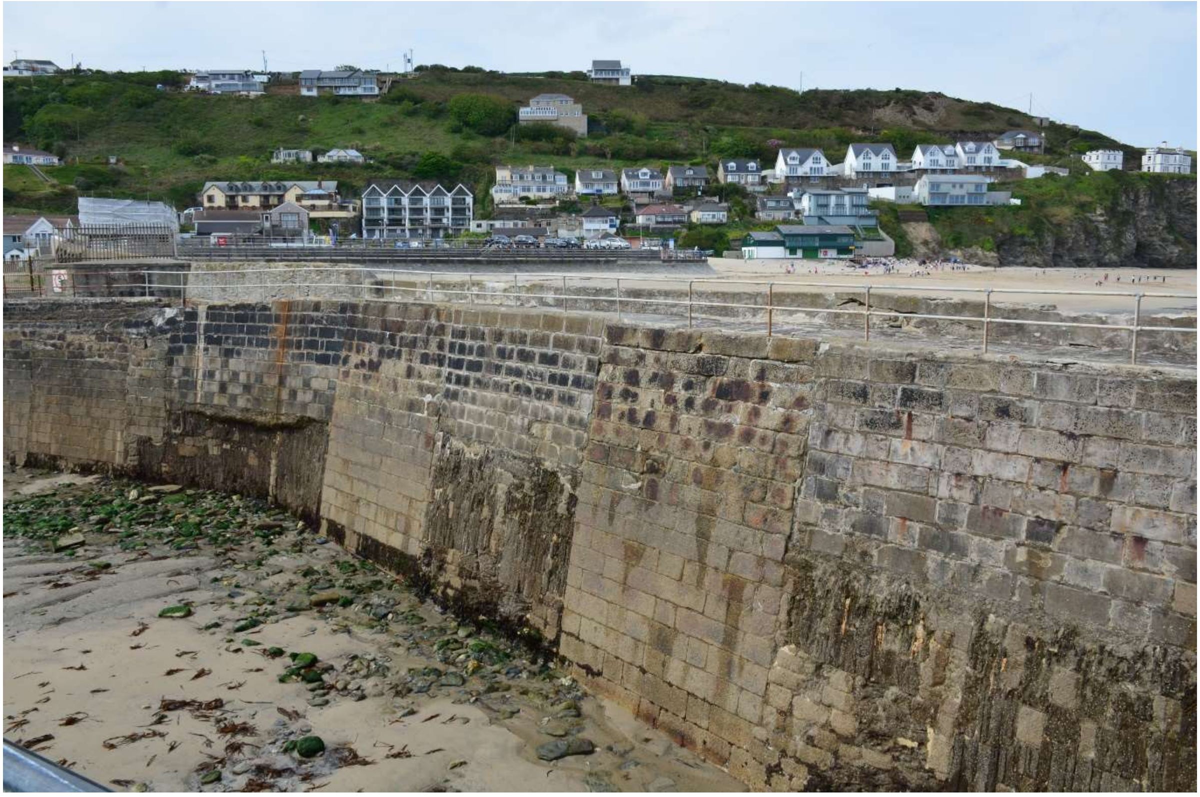

Figure 2.1.8. Right side (looking toward the see) of the second part of the wall in D position

Figure 2.1.9. Concrete repaired part in location C

The actual height of the wall is so unknown because there are not information of the buried wall for the other part of the structure. The section taken from the LIDAR data shown, for the first part of the wall, how the right part of the wall is about 8.5 m over the ground. The height over the ground of the left part changes section by section because of the outcropping rock and is anyway less than 8.5 m.

2.1.1. The 3^{rd}b part of the wall

The length of the destroyed part is about 21 m. Toward the sea, the failure occurred between the last buttress of the wall and the previous one. The buttresses are 0,9 m large and 4 m tall (over the soil). They are 1 m thick. The length of the buttress below the soil is the same of the found wall deep. The buttresses are disposed every 4,5 m. After the last buttress, which is after the first 2 m of the destroyed part, attached to the wall there are the stairs, which connect the beach with the car park. The stairs were rebuilt in 2018 as well. This part of the wall was made of masonry and it was 4 m tall over the soil level and the thickness went from 0,8 m at the top to 0,94 m at the soil level.

In Figure 2.1.11 is shown the third part of the wall which was rebuilt as a reinforced concrete wall coated with blocks. In this occasion, to establish the depth of the wall foundation 3 trial holes were dug with an excavator in the position indicated in Figure 2.1.12. The results are shown in Figures 2.1.13-2.1.15. The trial holes showed that the wall is not founded to a footing. In particular, there was no indication of rock or concrete base but the wall was only buried in the sand. It has been seen how the wall goes at least 3 m under the ground level in one point. This, in addition to the rock basement on the first part of the structure, makes the hypothesis of fixed support close to the real behaviour of the foundation part.

Figure 2.1.10. Damage in the 3^{rd}b part of the wall after the storm in 2018 (Cornwall Live, 2018)

Figure 2.1.11. Rebuilt of the 3rdb part, completely destroyed in 2018

Figure 2.1.12. Indication of the trial holes in the 3rdb part (Environment Agency, 2018)

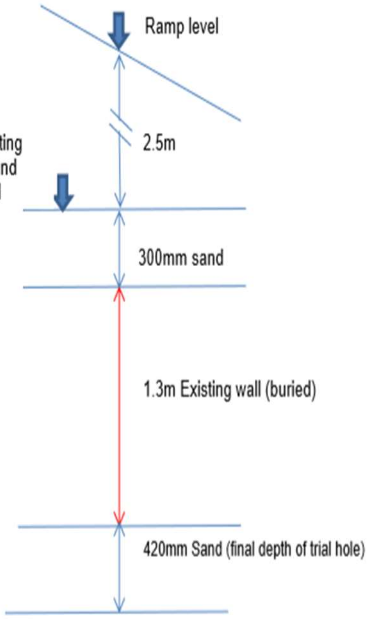

Figure 2.1.13. TH1 results (Environment Agency, 2018)

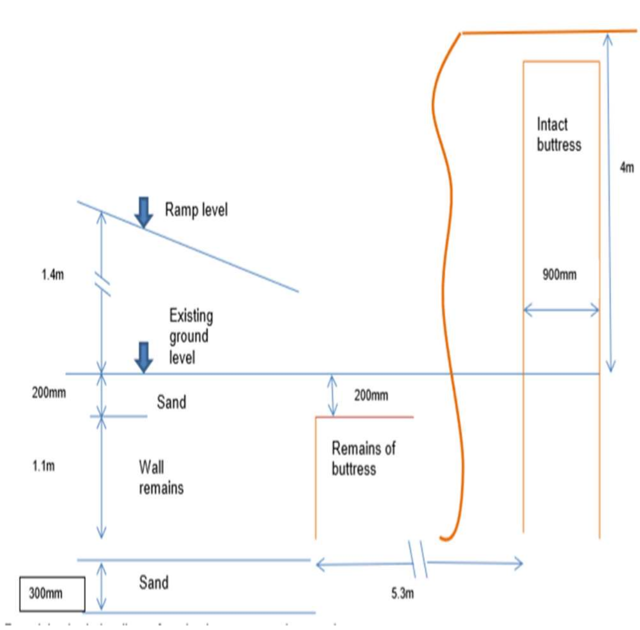

Figure 2.1.14. TH2 results (Environment Agency, 2018)

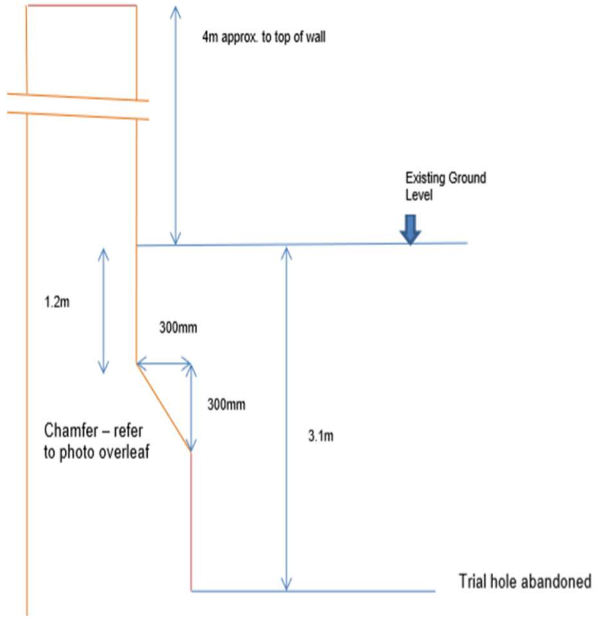

Figure 2.1.15. TH3 results (Environment Agency, 2018)

The geometry of the rebuilt part of the wall is described below.

As shown in Figure 2.1.16 the rebuilt part is a reinforced concrete wall with a sandstone cover linked to the wall as explain in Figure 2.1.17. The concrete used for the wall is a C32/40. Between the foundation of the wall and the soil there is a layer of concrete binding at the bottom and a sacrificial concrete layer at the top right part. The top of the wall is covered with a concrete capping in order to match the existing wall. On the left side, the stone facing is supported by a concrete blockwork. The sandstone used for the cover comes from local quarries. The reinforcement used (Figure 2.1.18) is a B25 with a spacing equals to 150 mm.

Looking at the data coming from the LIDAR section of this part of the wall, in the model it has been assumed that the wall is 4 m above the soil, while 1 m of the wall and the foundation (another 1 m) are buried in the sand. The rebuilt wall is 21 m long.

At both of the two ends of the new wall there are ties that link the new wall with the old one as explained in Figure 2.1.19-2.1.20.

Ties have a diameter equals to 75 mm and they are drilled horizontally into existing masonry wall to a minimum of 500 mm. The wall is divided in two parts (10.5 m long each) linked in the middle of the rebuilt structure by a joint as indicated in Figure 2.1.21.

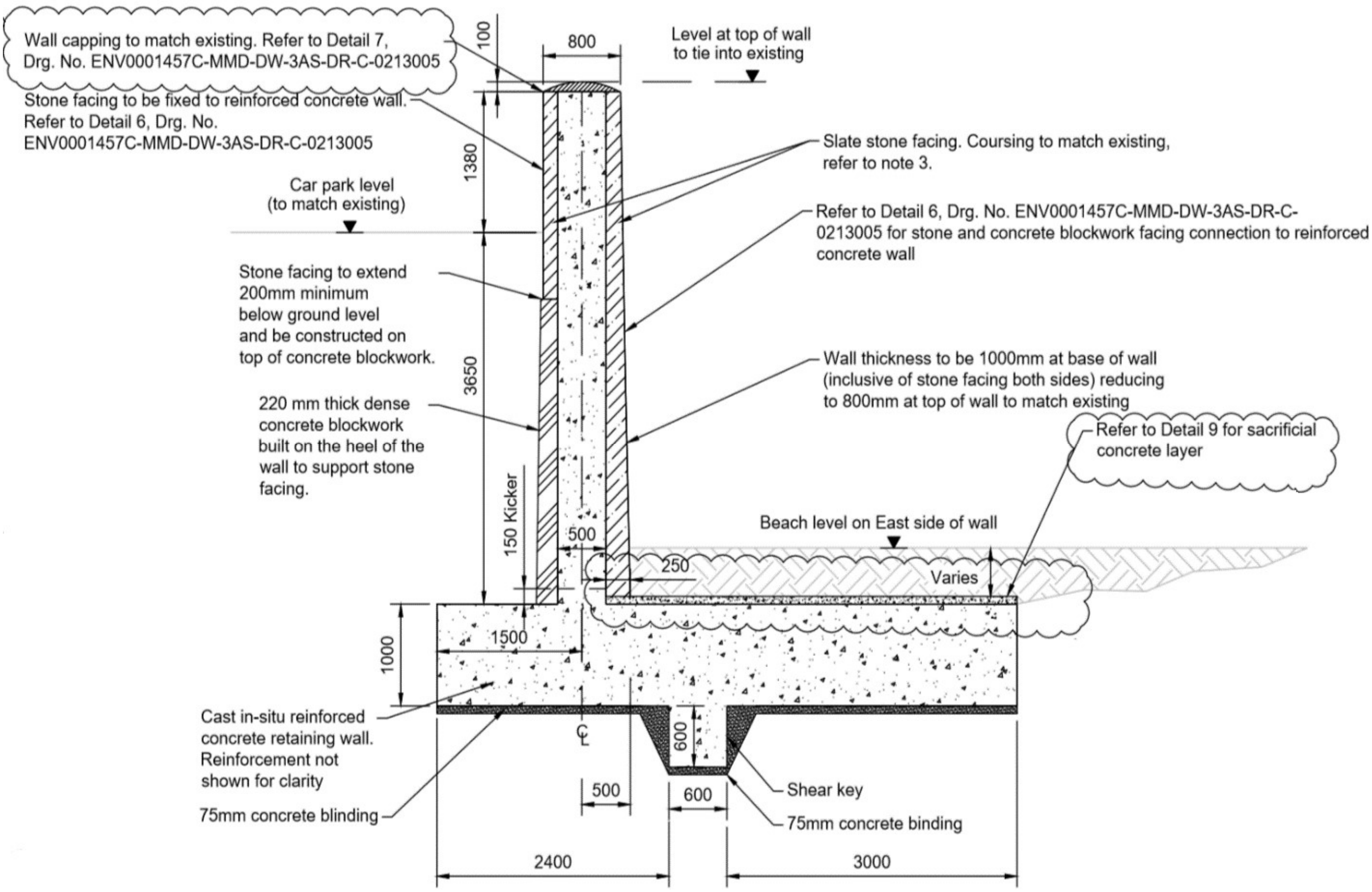

Figure 2.1.16. The rebuilt reinforced concrete wall (Environment Agency, 2018)

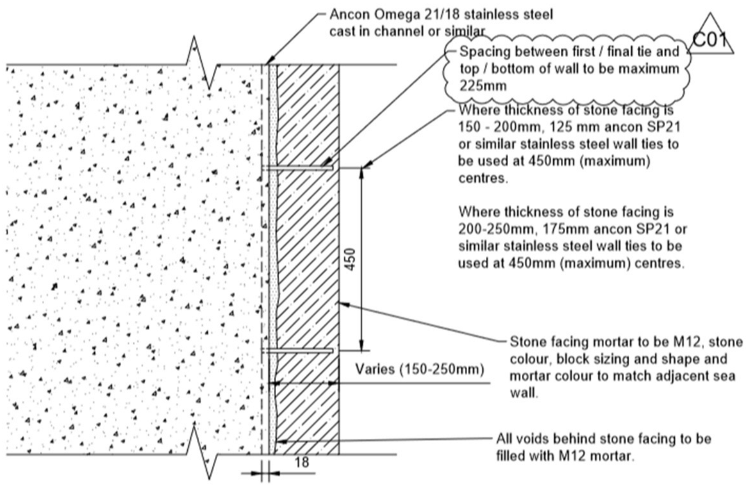

Figure 2.1.17. Detail of the connection between the concrete wall and the stone cover (Environment Agency, 2018)

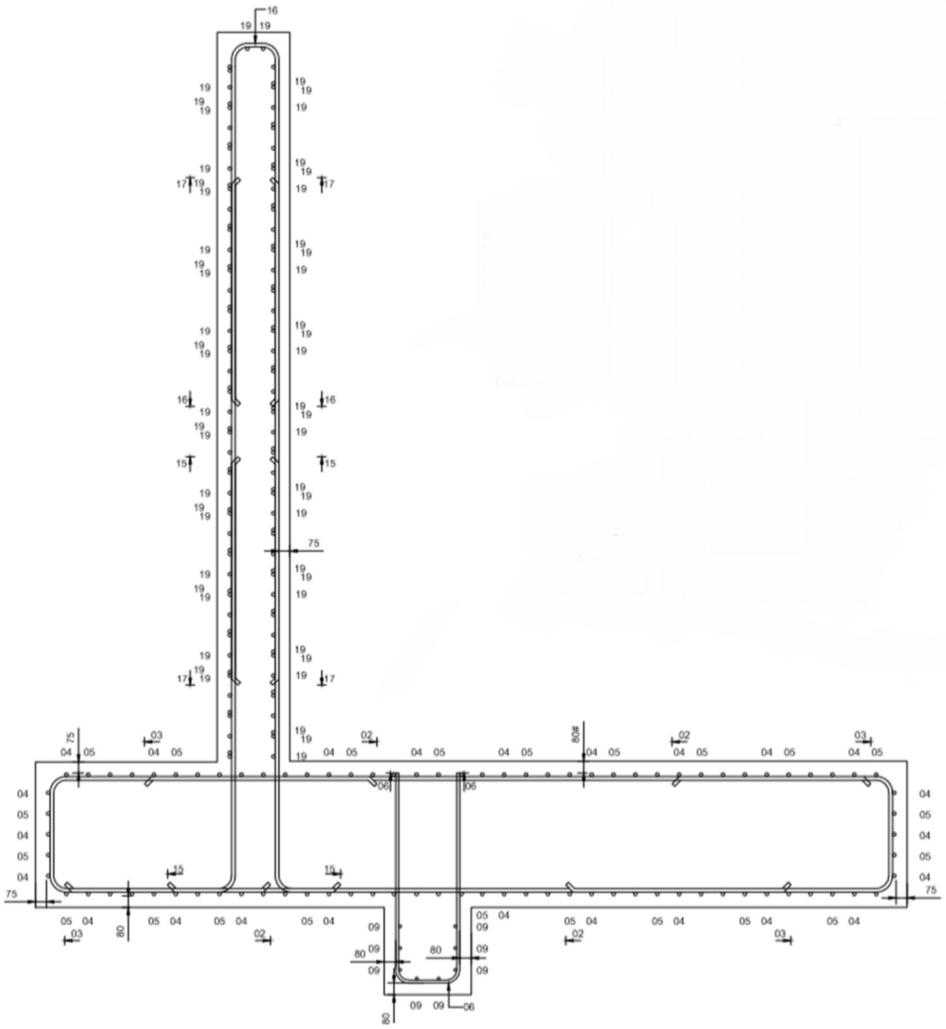

Figure 2.1.18 Steel reinforcement (Environment Agency, 2018)

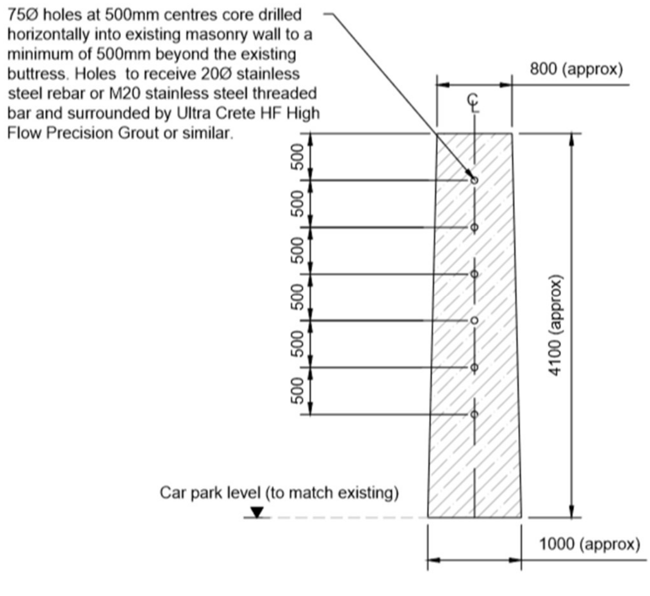

Figure 2.1.19. Connection between new and old wall (Environment Agency, 2018)

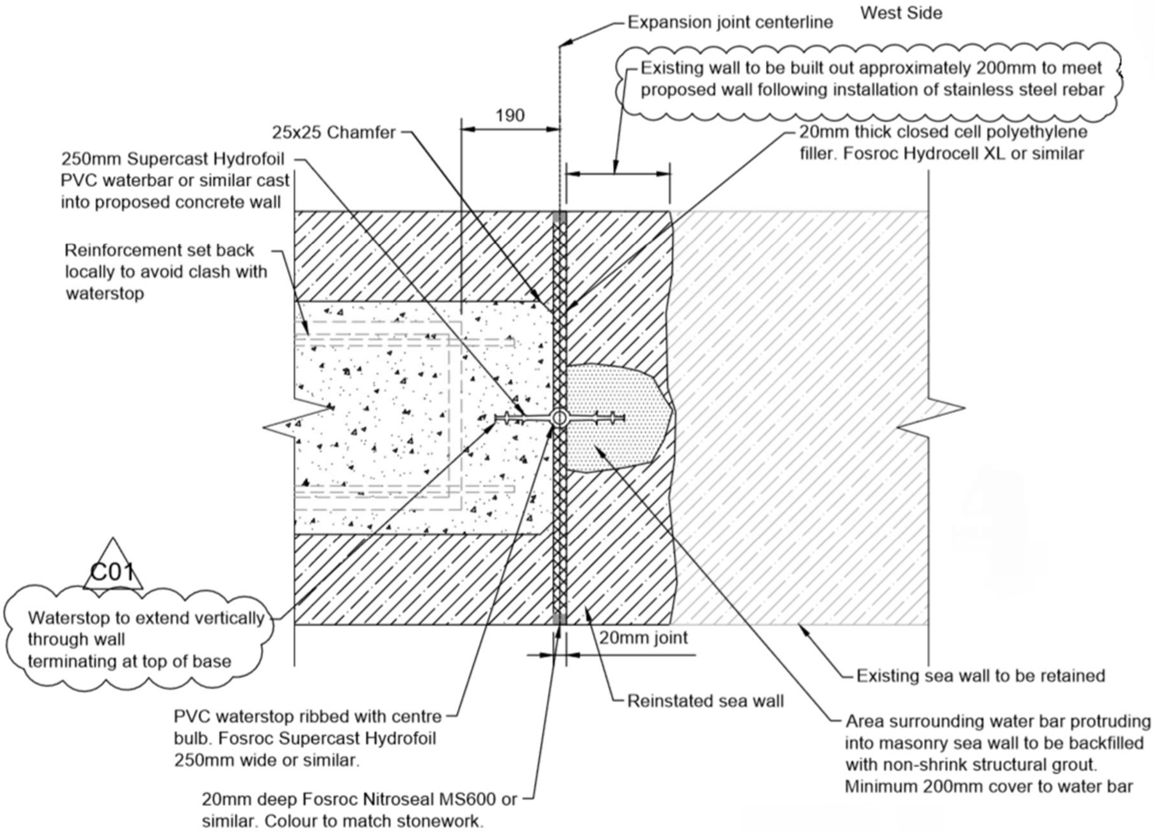

Figure 2.1.20. Detail of the connection between the old and the new wall (Environment Agency, 2018)

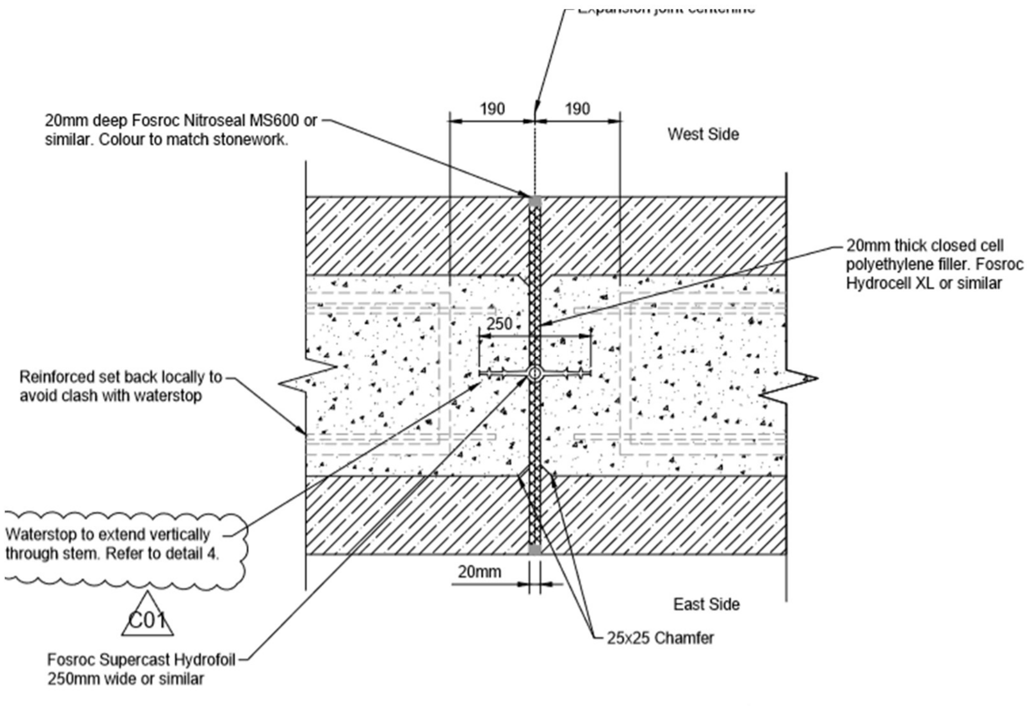

Figure 2.1.21. Joint between the two parts of the wall (Environment Agency, 2018)

2.2. Young's modulus calculation

A Schmidt Hammer was used in order to define the material Young's Modulus values. The Type N Rebound Hammer used (Proceq®) is characterised by an impact energy equal to 2,436 Joule. The hammer is intended for non-destructive testing of concrete quality in a finished structure. From the recorded value, it is possible to know the concrete strength by using conversion curves given with the instrument, calibrated with a several hammer tests on concrete cubes. Those curves also consider the inclination of the hammer, which is calibrated for horizontal impact direction; so vertical surfaces were favoured for the test and the calibration curves were not applied to the results in this study.

The device has a spring-loaded piston which is simply struck against the material surface until the metal rod is completely compressed and automatically on the side of the instrument is indicated the rebound number, R. To read the rebound value it is necessary to press the bottom, which releases the spring mechanism. The value of R goes from 10 (very weak material) to 100 (very strong material).

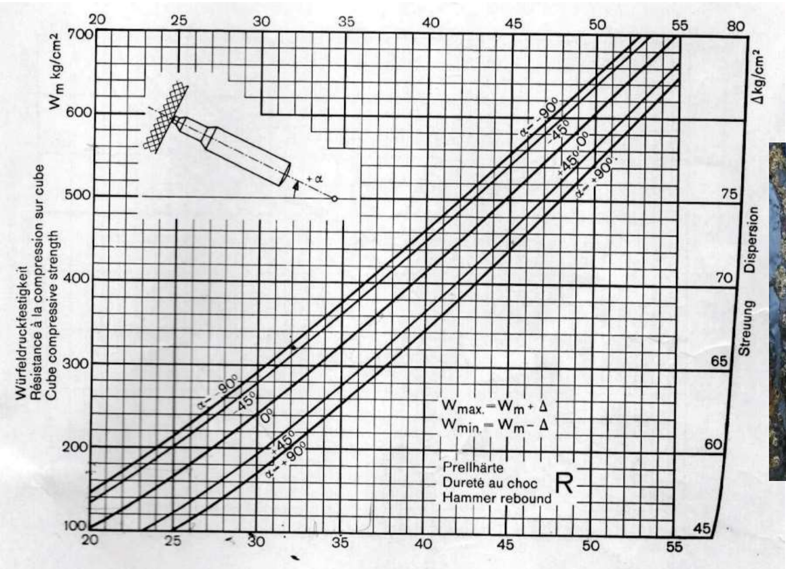

Figure 2.2.1. The instrument

Figure 2.2.2. Cube Compressive Strenght against the Rebound Number (Proceq®)

2.2.1. Research

According to Goudie (2006) the Schmidt Hammer was first used in geomorphological contexts in the 1960s. Since then it has been used for an increasing range of purposes because of its simplicity and advantages. The rebound value read on the hammer is empirically well correlated with other rock properties. It is important to consider that the instrument is strongly sensitive to discontinuities in the material (and so cannot be used on laminated rock), to the moisture contents and by surface texture. The test should be used only on big and heavy rocks. The surface to be tested, requires to be prepared by taking out surface flakes, weathering resides and lichens.

An indicative value of the R number is given for many different rocks (Goudie, 2006). The highest value of R is around 60 for quartzites, very hard limestones and various igneous rocks. The Schmidt Hammer has been used also to determine rock properties such as compressive strength and Young's modulus, and different correlation formulations are given for different kind of rocks (Goudie, 2006). The following two equations (Kats et al., 2000) were adopted for this study. For the material in examination, the authors have indicated strong empirical correlation between the rebound number R and measured Young's Modulus (1) as well as with the uniaxial compressive strength of the rock (2):

$$E = 0.00013R^{3.09074} \ \ [GPa] \quad (1)$$

$$UCS = 2.208e^{0.067R} \ [MPa] \quad (2)$$

Hack and Huisman (2002) state how a large number of Schmidt Hammer tests give a better estimation of the rock strength at different locations than a few number of finer tests. The high variation on the R number usually obtained in different point of the same structure is because of the changes in the mineralogies and lithologies of the material and consequent variation in weathering rates. Moreover, in the case of rocks used as block in structures, because of the sulphation, the development of weathering crust and other effects, the hardness of the block may change. Goudie (2006) also gives a correlation between the rebound value and the material weathering degree.

Furthermore, Mol (2014) states that the amount of thermal stress, the presence of water as well as the development of microbial activity and the cycling of chemicals and salt cause a weakening of the rock surface and, as consequence, erosion. As surface deterioration sets in the cementation between grains, weakens and loss of material arises. In order to assess weathering rates it is necessary take into account different factor such as temperature fluctuations, precipitation levels as well as predisposition to weathering of the bedrock.

Moreover, the readings are affected by the "edge effect" if the measurement is done close to the rock edge or a crack. The results are also depending from the surface irregularities and the user experience. Using a statistical approaches with the data analysis those errors are reduced. Particularly, having done the test on a coastal structure, it is important to remember that the water content in the material and the presence of microbial colonies greatly influence the readings. In addition, for the case in study, many small shells were attached to the surface and this limited the area to be tested.

Viles et. al. (2010) have shown how a wet surface reduces the rebound value and how for small block the Schmidt Hammer is not accurate because of a higher edge effect. The authors also claim that the most used Schmidt Hammer in geomorphology is the N-Type that can be used from a very weak rock to a very strong one. The compressive strength range which can be measured goes from 20 to 250 MPa.

2.2.2. Results

Taking into account all these precautions, the tests were done. Laboratory staff previously calibrated the instrument. Obviously, how it has been said, the values calculated in that way depend by the local composition of the material in the area where the test is done and it is representative of the only superficial properties of the structure. For this reason, a statistical treatment of the measurement is required and different ways are used in practice. In this study, the impact test was carried out at 12 points per testing area (4 point per 3 rows, with a distance of 5 cm between) and a mean of all the values, except the two biggest ones which were taken away (values in orange in Table 2.2.2), was done. In taking the mean, all the values that deviate from the mean of the others by more than 6 units (values in red in table 2.2.1-2.2.2) must to be eliminated and replaced with new reading. For each area where the test was done it is also possible to have the most likely value and the minimum value of the cube compressive strength in kg/cm^2. The same test was done in the following zone of the wall shown in the Figure 2.1 giving the results reported in the Tables 2.2.1-2.2.4.

Table 2.2.1. Rebound values in location A

A				
Measured R values				**R**
Block				
34	40	46	32	42
46	46	42	44	
36	42	46	36	
Mortar				
22	16	24	22	21
Metal				
10	10	10		10
Rusty metal				
32	40	32		35
Bars in the hole				
54	53	40	36	46

Table 2.2.2. Rebound values in location B

B				
Measured R values				**R**
Block				
52	52	44	64	48
44	38	58	45	
50	52	46	60	
Old mortar				
20	20	20	18	20
New mortar (concrete)				
34	28	40	38	37

Table 2.2.3. Rebound values in location C

C				
Measured R values				**R**
Dark stone				
30	33	32	34	32
Light stone				
62	62	62		62
Mortar				
10	10	10		10

Table 2.2.4. Rebound values in location D (left) and correlated concrete properties (right)

D				
Measured R values				**R**
Modern concrete				
35	32	30	34	33
Older concrete				
40	38	42	36	39
35	40	40		
Dark stone				
25	27	24		27
24	30	30		

Modern concrete			
R_{ck} [MPa]	f_{ck} [MPa]	f_{cd} [MPa]	E_{cm} [GPa]
28.5	23.7	13.4	31.1
Older concrete			
R_{ck} [MPa]	f_{ck} [MPa]	f_{cd} [MPa]	E_{cm} [GPa]
39.5	32.8	18.6	33.5

Where the less than 12 points are tested, it is because of the small accessible geometry, which did not make possible to test more points. For both blocks and mortar, the test was done in the front of the wall and in the second part (see Figure 2.1). In the second part the different blocks and two different concrete areas were also tested. In the first part, the test was carried also on the hole and the metal strips for sake of comparison. Only the bare rock surface, far from the edges and holes, were tested. It is worth remembering that all the blocks were wet because of the daily high tide and so the values recorded are smaller than the real ones. On the other hands, the values are also affected by the material age. Anyway, the Schmidt Hammer should be always coupled with other tests if the recorded properties will be used as design values.

On the front of the wall, the Schmidt hammer test on the blocks gave a rebound number R of 42 while on the mortar the value is 21. These values were increased of 10% in order to consider the effect of superficial humidity and weathering (Pappas et al, 2017) becoming, for the block in part A, 46.6. For the only measurement on rock, the increased values were correlated with the material properties using equations (1) and (2) giving, for the block in location A, a value of the Young's modulus equals to 18.7 GPa and a value of the compressive strength equals to 50 MPa. In the part of the model where has been considered an unique material the Young's Modulus was reduced of 30% in order to consider the effect of the actual geometry with block and mortar which creates orthogonal fractures on the intact block (Pappas et al, 2017; Min and Jing, 2003). Thus, the Young's modulus became 13 GPa instead of 18.6 GPa. On the other hand, the authors showed how the Poisson ratio for a fractured rock is higher than for an intact rock. This is because of the lower shear stiffness of fractures.

In the case of the concrete, using the graph in Figure 2.2.2 it is possible to obtain the cube compressive strength of the concrete (R_{ck}) from the R number. Once that the R_{ck} is known it is possible to calculate the concrete Young's Modulus and the design uniaxial compressive strength by the EUROCODE 2 formulations:

$$f_{ck} = 0{,}83 R_{ck}\ [MPa] \qquad (3)$$

$$E_{cm} = 22 \left(\frac{f_{ck}+8}{10}\right)^{0.3}\ [GPa] \qquad (4)$$

The same graph was used in order to define the compression strength of the mortar. The mortar Young's Modulus was calculated considering it as a concrete.

In Table 2.2.4 it is possible to see how the concrete properties are practically equal to the theoretical ones and it worth to observe that the properties of the older concrete are slightly higher than the ones of the younger concrete as expected.

Figure 2.2.3. Sandstone brick and mortar in part A (it is possible to see also the metal strips and the hole with rebar)

Figure 2.2.4. Sandstone brick and mortar in part B (it is possible to see in the lighter part the new mortar

Figure 2.2.5. Light stone (granite) and mortar in part C

Figure 2.2.6. Dark stone in part C and D

Figure 2.2.7. Older concrete in part D (left part)

Figure 2.2.8. New concrete in part D (left part)

The values for the mortar in location C (see table 2.2.3) confirmed that the new mortar is practically concrete applied on the older mortar, how it was supposed. However, the older mortar is a very weak material high degraded. Indeed the mortar surface was dented during the test.

The results on blocks seem to indicate that in the central part granite blocks were used alternated with the black weaker blocks. A different block was used in the first part, according with the different construction times of the different parts of the wall. See Figure 2.1 for the labels reported in the photos.

The values found seem to confirm that the wall was built with the local materials. Particularly, the first part of the wall seems to be made in sandstone and this is in accordance with the sedimentary bedrock in Portreath made of sandstone and mudstone. In the central part of the wall it might be used granite block (according to the pink shades on the surface) coming from the close granite deposit. The geology of the site is shown in the geological maps available in the British Geological Survey website. In confirmation of that, it should be considered that Portreath possessed a lime kiln, in which limestone was reduced to lime for building purposes. The limestone came from South Wales and from Plymouth by sea. The kiln, as well as other historical structures in Portreath, was constructed from local stone and granite blocks. Moreover, in the harbour there was a local sandstone quarry in the past and hence the blocks with high likelihood come from there.

In the Historical Atlas of South West England (1999) it is also indicated how the traditional building material in Cornwall were basically sandstone, limestone and granite. Especially the sandstone, occurs in a great variety in type, colours and building qualities because of it was laid down in varying continental and marine environments. The Atlas explains how it was really common to combine sandstone with flint and chert in the construction in striking chequered and zig-zag patterns. The black rock used in a few parts of the wall so might be chert. Native Portreath people stated that the core of the wall is made with loose rubble.

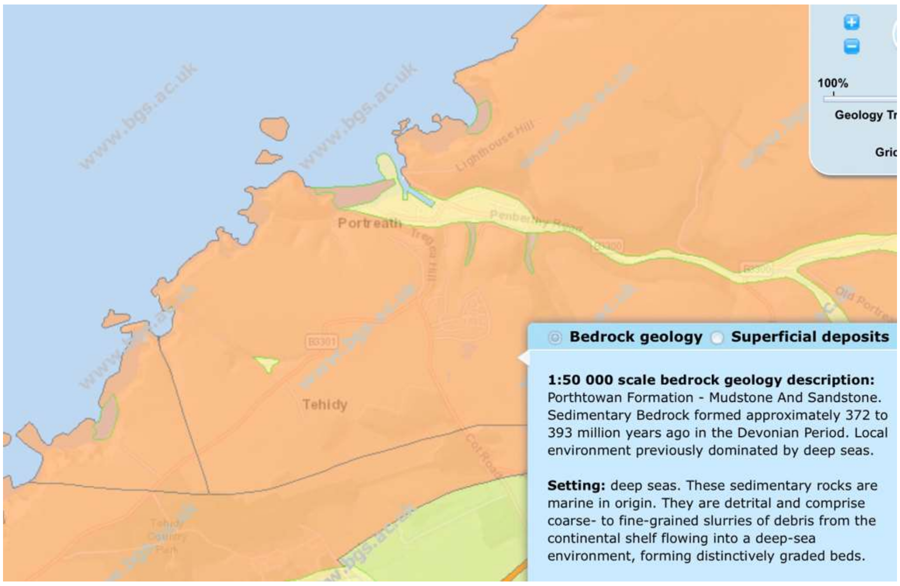

Figure 2.2.9. Portreath bedrock below the harbour wall (Geological British Survey, 2019)

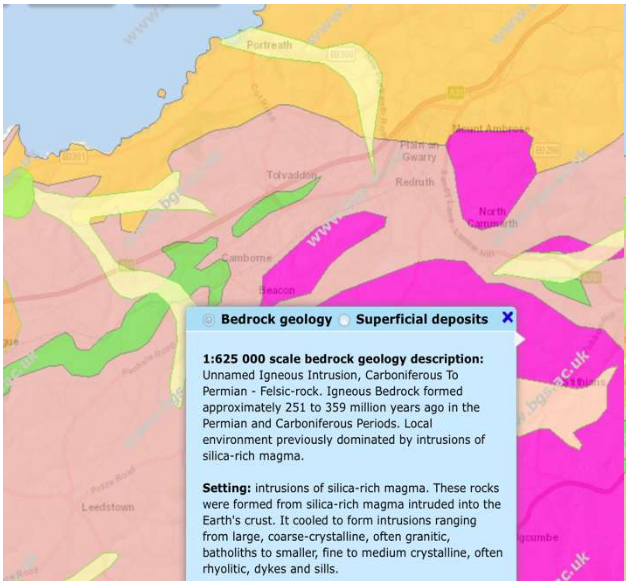

Figure 2.2.10. Igneous bedrock close to Portreath (Geological British Survey, 2019)

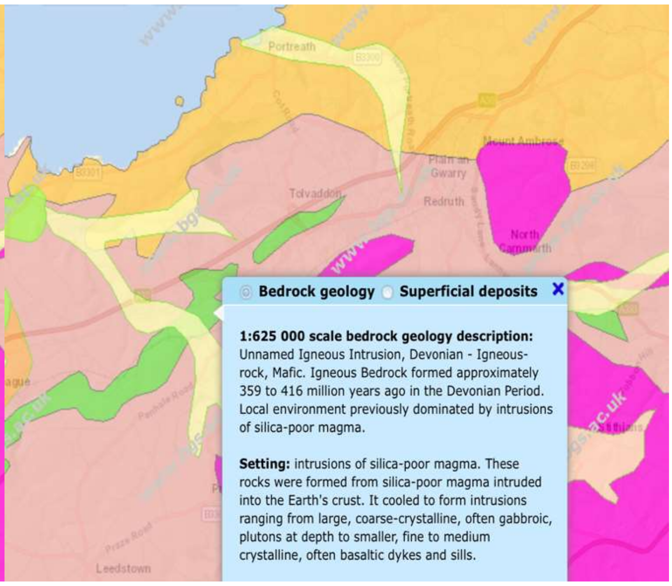

Figure 2.2.11. Igneous bedrock close to Portreath (Geological British Survey, 2019)

3. Finite element model of the first part of the wall

A finite element model of the first part of the wall was created in ANSYS AIM 19.1. Particularly, the Structural section of the program was used. The FEA gives accurate results and makes possible modelling complex geometry with a lot of elements by using an accurate material definition and also performing dynamic and nonlinear analysis. Moreover, because of the intelligent mesh technology, ANSYS is able to create the optimal mesh for every geometry in the model and to adapt it by re-meshing the solution during the analysis (ANSYS, 2019).

3.1. Geometry

The geometry of the wall was drawn in AUTOCAD and then exported into ANSYS using an *.igs* format. Though in this analysis the main interest is on the effect of the waves on the front face of the wall, a 3D model was adopted because of the out of the plane inclination of the front wall. Moreover, in order to see the effect of the waves on the Monkey Hut (because it is known that it was destroyed by the waves in 2014, see Introduction), a portion of the first part of the pier was modelled. The geometry information is indicated in the following pictures. The Monkey Hut has a circular shape with an aperture which acts as a door on the side toward the village.

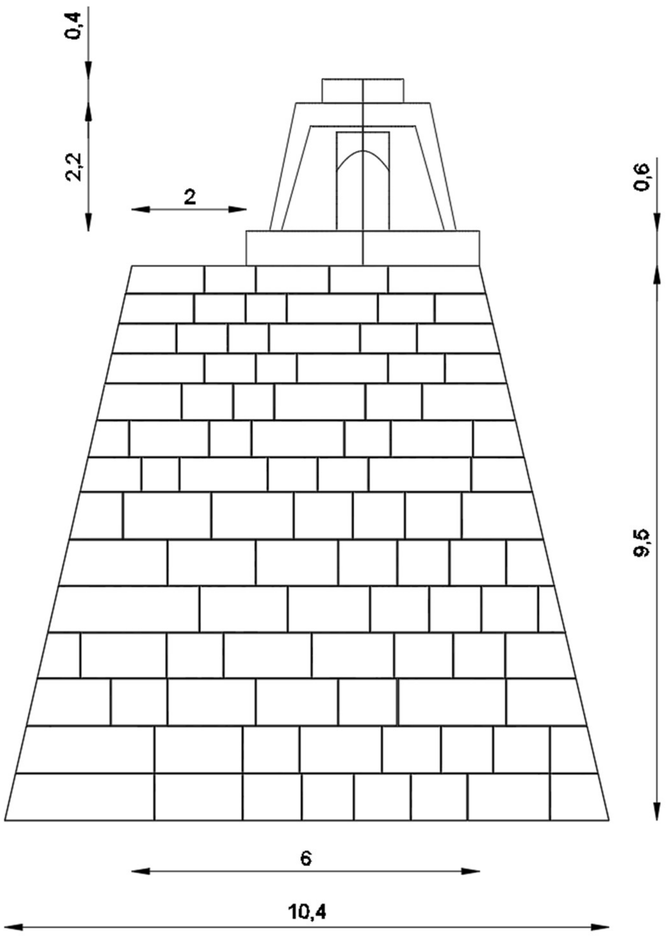

Figure 3.1.1. Geometry of the front of the wall (values in meters)

The blocks on the front of the wall have a depth of 0.5 m. Only on the front of the wall both blocks and mortar have been considered in the model. Because in this part the model is focusing on the front face and in order to simplify the model, all the rest of the structure was modelled as a unique equivalent material. All the edges of the wall are covered with a 0.5 m depth layer of this equivalent material. Hence, there is an internal core made of loose rubble. The mortar has a thickness of 1.5 cm, while the blocks have the dimensions reported in the paragraph 1.1. The first five courses of block are completely under the outcropping rock in the front of the wall while along the pier the outcropping rock is less high.

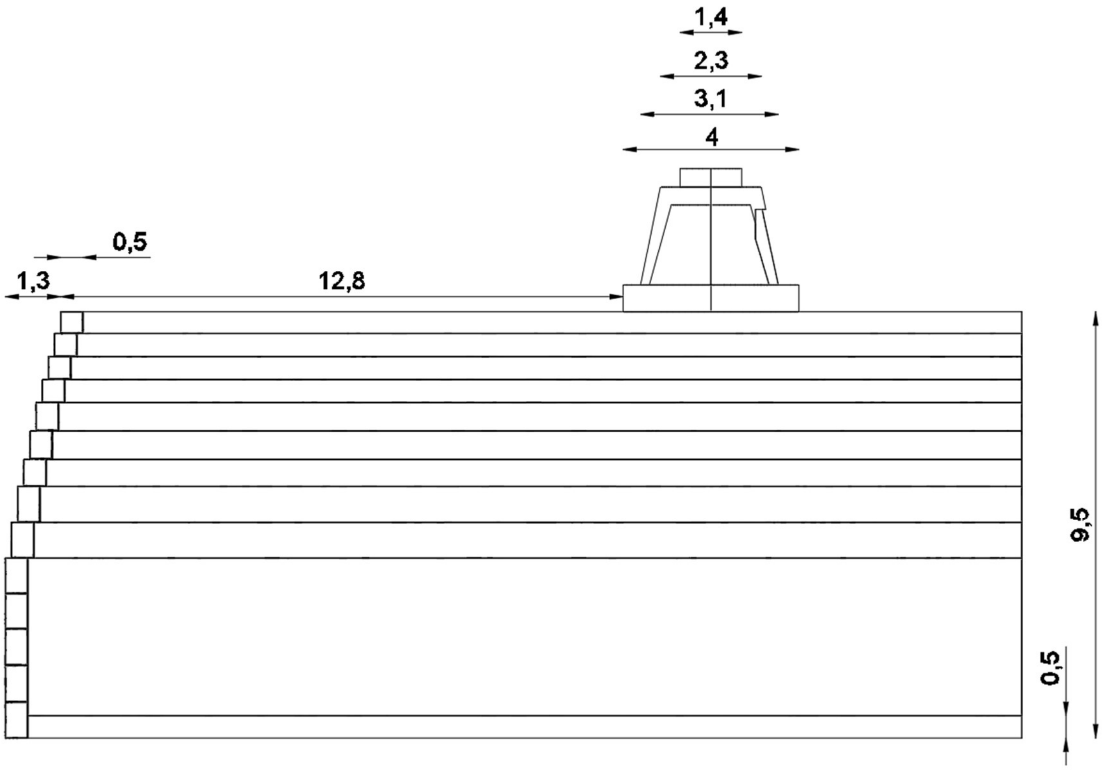

Figure 3.1.2. Geometry of the side of the wall (values in meters)

3.2. Material

Material properties applied to the geometry are defined in the following figures. For the front of the wall, sandstone block and mortar were considered while for the rest of the structure, on the edge for a depth of 0.5 m, an equivalent unique material was applied and all the properties were calculated as defined in the paragraph 1.2. Those properties were further decreased for modelling the internal core in loose rubble. The bottom and the top part of the Monkey Hut are made of concrete, while the masonry structure was modelled with the same proprieties of the internal core. ANSYS has a library with all the properties already defined for all the different materials. Young's Modulus and compressive strength were modified according to the calculated values in paragraph 1.2 and to the main values for these kinds of materials obtained from literature. All the other properties were kept as defined by ANSYS and only modified when they were far from the main values found in literature.

Property	Value	
Material Field Variables	Table	
Density	2000	kg m^-3
Isotropic Elasticity		
Derive from	Young's Modulus and Poisson's Ratio	
Young's Modulus	1.8007E+10	Pa
Poisson's Ratio	0.23391	
Bulk Modulus	1.1278E+10	Pa
Shear Modulus	7.2965E+09	Pa
Bilinear Isotropic Hardening		
Yield Strength	5E+07	Pa
Tangent Modulus	0	Pa

Figure 3.2.1. Sandstone block properties

Property	Value	
Material Field Variables	Table	
Density	2300	kg m^-3
Isotropic Secant Coefficient of Thermal Expansion		
Coefficient of Thermal Expansion	1.4E-05	C^-1
Isotropic Elasticity		
Derive from	Young's Modulus and Poisson's Ratio	
Young's Modulus	1E+10	Pa
Poisson's Ratio	0.2	
Bulk Modulus	5.5556E+09	Pa
Shear Modulus	4.1667E+09	Pa
Bilinear Isotropic Hardening		
Yield Strength	5.4E+06	Pa
Tangent Modulus	0	Pa
Tensile Yield Strength	6E+05	Pa
Compressive Yield Strength	5.4E+06	Pa
Tensile Ultimate Strength	6E+05	Pa
Compressive Ultimate Strength	5.4E+06	Pa

Figure 3.2.2 Mortar properties

Property	Value	
Material Field Variables	Table	
Density	2000	kg m^-3
Isotropic Elasticity		
Derive from	Young's Modulus and Poisson's Ratio	
Young's Modulus	1.3007E+10	Pa
Poisson's Ratio	0.25	
Bulk Modulus	8.671E+09	Pa
Shear Modulus	5.2026E+09	Pa
Bilinear Isotropic Hardening		
Yield Strength	3.5E+07	Pa
Tangent Modulus	0	Pa

Figure 3.2.3 Equivalent material (block + mortar) properties

Property	Value	
Material Field Variables	Table	
Density	2000	kg m^-3
Isotropic Elasticity		
Derive from	Young's Modulus and Poisson's Ratio	
Young's Modulus	1.0036E+10	Pa
Poisson's Ratio	0.32955	
Bulk Modulus	9.8133E+09	Pa
Shear Modulus	3.7744E+09	Pa
Bilinear Isotropic Hardening		
Yield Strength	7E+06	Pa
Tangent Modulus	0	Pa

Figure 3.2.4. Loose rubble properties

Property	Value	
Material Field Variables	Table	
Density	2400	kg m^-3
Isotropic Secant Coefficient of Thermal Expansion		
Coefficient of Thermal Expansion	1.4E-05	C^-1
Isotropic Elasticity		
Derive from	Young's Modulus and Poisson's Ratio	
Young's Modulus	3.2E+10	Pa
Poisson's Ratio	0.19	
Bulk Modulus	1.7204E+10	Pa
Shear Modulus	1.3445E+10	Pa
Bilinear Isotropic Hardening		
Yield Strength	1.8E+07	Pa
Tangent Modulus	0	Pa
Tensile Yield Strength	1.3E+06	Pa
Compressive Yield Strength	1.8E+07	Pa
Tensile Ultimate Strength	1.3E+06	Pa
Compressive Ultimate Strength	1.8E+07	Pa

Figure 3.2.5 Concrete properties

For all the block materials, Mohr-Coulomb criterion was assigned considering an inner friction angle equals to 40º and a cohesion equals to 15 MPa.

3.3. Model

For sake of comparison, a first rough model was created considering everywhere a unique equivalent material (Figure 3.3.1). The results obtained from this model were compared with the results coming from the finer model with the front of the wall modelled with block and mortar and the internal core modelled with a weaker material (Figure 3.3.2-3).

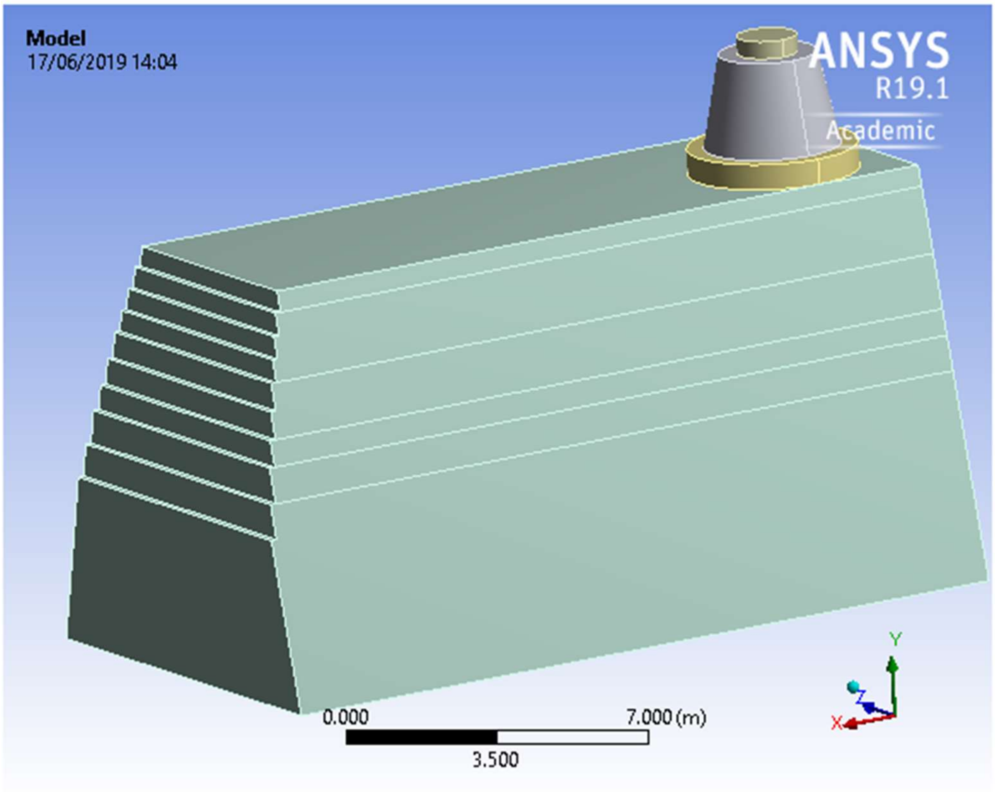

Figure 3.3.1 Rough model

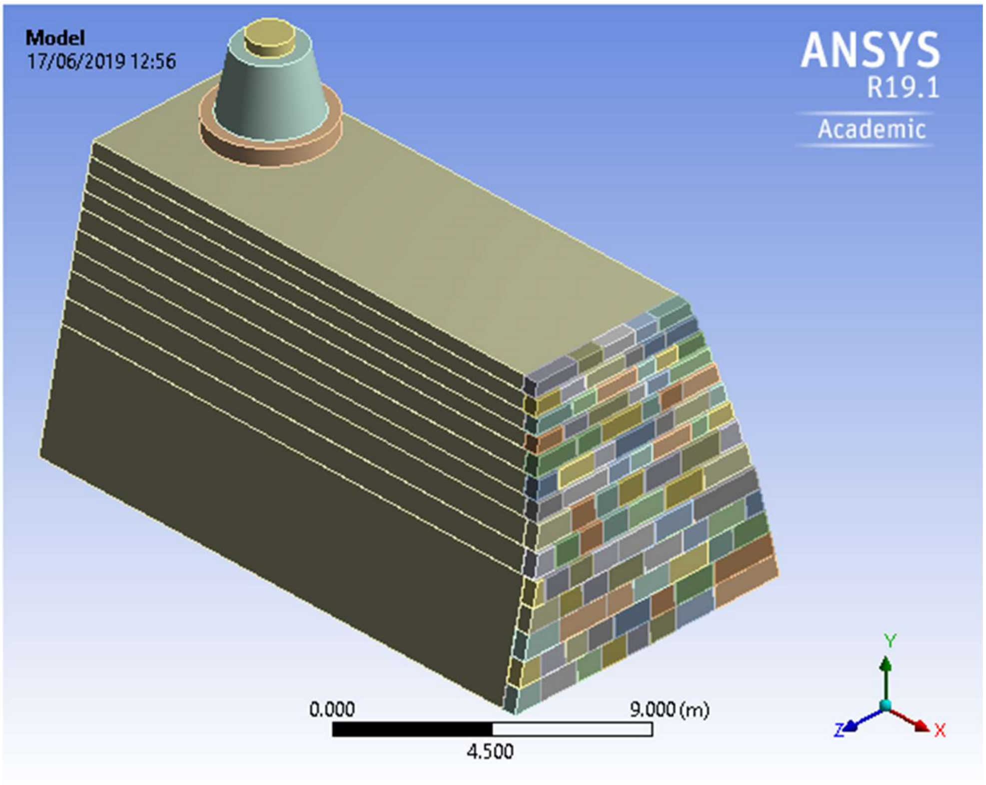

Figure 3.3.2 Finer model

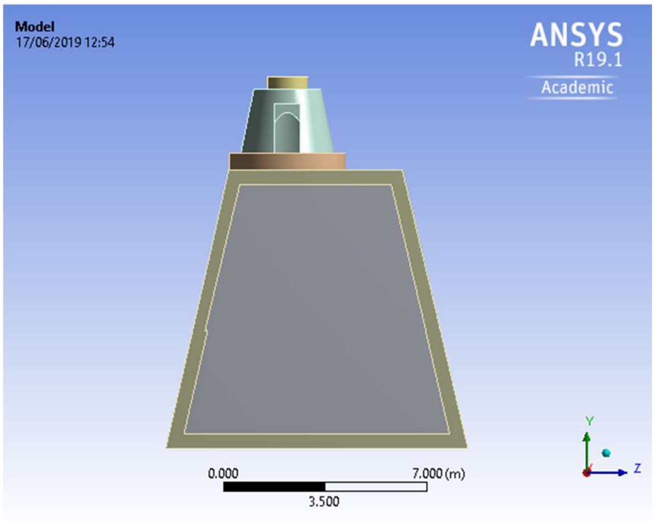

Figure 3.3.3. Internal core in the finer model

3.3.1. Mesh

A mesh was assigned to the models. For the blocks on the front face an element size of 0.2 m was defined using quadratic elements, while for the mortar a finer dimension equals to 0.003 m was preferred. These were the finest element size which has been possible to assign entering in the limits of the ANSYS Academic licence. For all the other elements it was assigned the ANSYS automatic mesh using triangle elements.

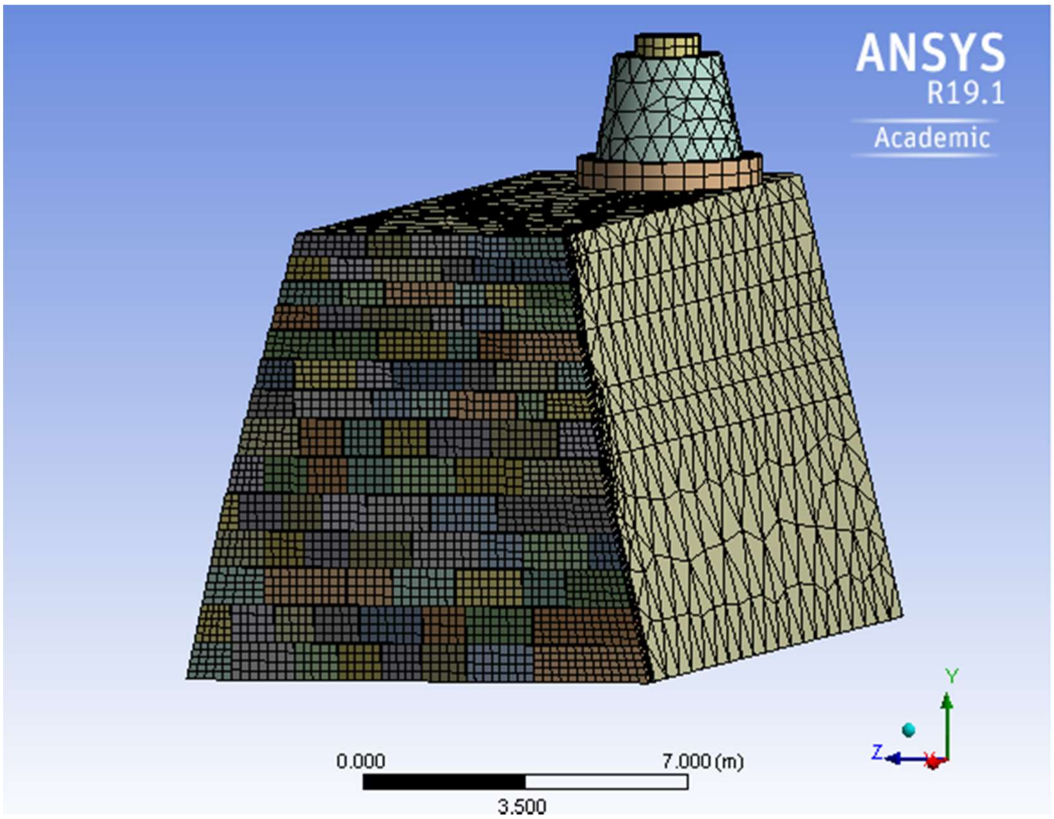

Figure 3.3.4. Mesh

3.3.2. Element type and connections

For the materials, a SOLID186 element was used. This element is a 3D 20 nodes solid with a quadratic displacement behaviour. Each of the 20 nodes has three degrees of freedom in x, y and z direction. As reported in the ANSYS library (ANSYS, 2019): "*the element supports plasticity, hyperelasticity, creep, stress stiffening, large deflection, and large strain capabilities. It also has mixed formulation capability for simulating deformations of nearly incompressible elastoplastic materials, and fully incompressible hyperelastic materials. SOLID186 Homogeneous Structural Solid is well suited to modelling irregular meshes (such as those produced by various CAD/CAM systems)*". For a few areas, the same element but with 10 nodes (SOLID187) was applied.

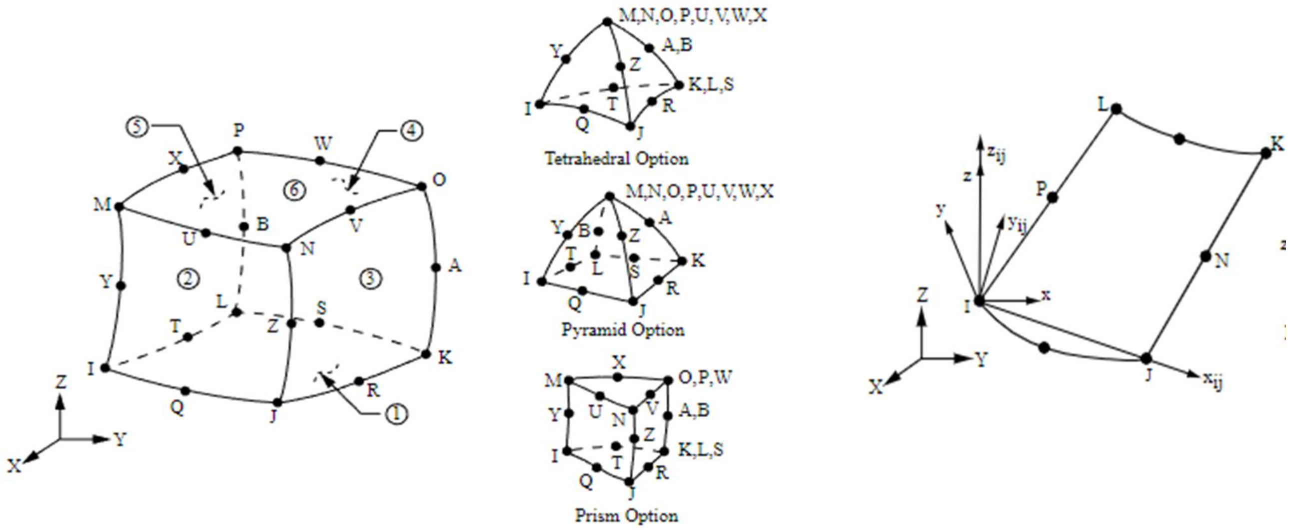

Figure 3.3.5 SOLID186 (left) and SURF154 (right). (ANSYS, 2019)

For the front face a SURF154 element was used. This element is used for different kind of loads and surface effects in a 3D model (ANSYS, 2019).

Connections between the blocks and the mortar (and between the other materials) were realized by assigning a CONTA174 element. This element is able to represent both contact and sliding between 3D surfaces and a deformable surface defined by this element (ANSYS, 2019). The element can model a general contact or also a pair-based contact.

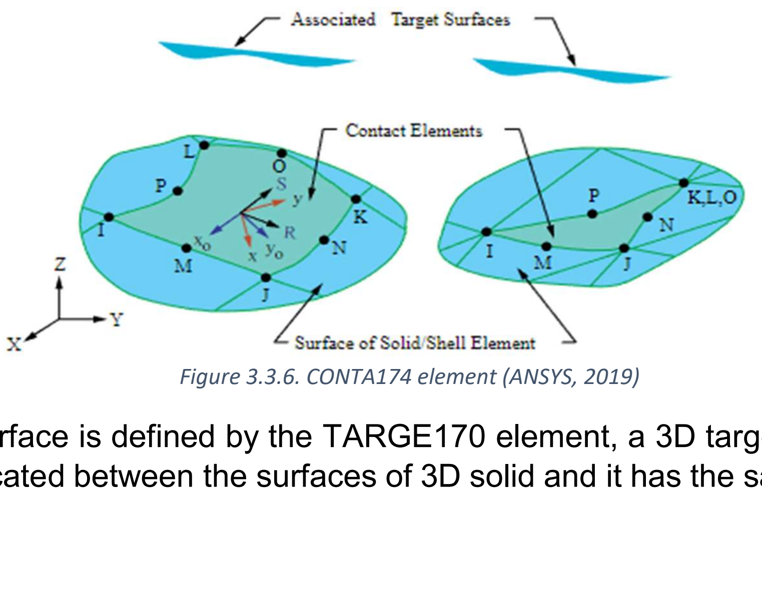

Figure 3.3.6. CONTA174 element (ANSYS, 2019)

The target surface is defined by the TARGE170 element, a 3D target element. CONTA174 element is located between the surfaces of 3D solid and it has the same geometric features of the surface with which is connected. The element supports isotropic, orthotropic Coulomb friction, shear stress friction and user-defined friction between the two solid surfaces. The bonded contact can be separated in order to simulate the interface delamination.

3.3.3. Support

Considering that the wall is based on a bedrock and that at least 3 m of wall are underlying the rock, a fixed support was assigned along all the base of the structure.

In order to simulate the connection between the first and the second part of the wall, a fixed support was also assigned to the section at the end of the model.

3.3.4. Load

Self-weight was assigned to the whole model by defining a gravitational acceleration $g = 9.81\ m/s^2$ and the material densities are indicated in the Figures 3.2.1-3.2.5.

On the front of the wall the following pressure distribution was applied:

Table 3.3.1. Pressure waves on the front of the wall (highest wave height)

p_1 [kPa]	p_2 [kPa]	p_3 [kPa]	p_4 [kPa]
165.1	162.6	158.9	136.8

These pressures simulate the wave action and they were calculated and applied as reported in the following paragraph. Next paragraph also explains how these values are associated to the scenario with the highest wave on the wall (and the associated tide level). The same distribution was also calculated for the case with the highest tide level (design water level at the top of the wall and the associate wave) giving the following value:

Table 3.3.2. Pressure waves on the front of the wall (highest tide level)

p_1 [kPa]	p_2 [kPa]	p_3 [kPa]	p_4 [kPa]
110.1	104.3	100.2	110.1

It is clear that the first scenario is the worst for both the wall and the Monkey Hut, and hence only the results for this case will be discussed.

Considering the comparison between the wave length and the distance between the front face and the Monkey Hut (13 m) the same pressure values calculated for the front face were applied to the Monkey Hut. Especially for the second scenario, it is not unlikely to have wave breaking on the Monkey Hut. The results will be in this way on the safe side and, considering the uncertainty in using the reduction factor, there was the risk to underestimate the values of the pressure on the structure.

The load was applied in the function of time in order to simulate a dynamic load. The force-time series adopted is shown in Figure 3.3.7, which was given by Bullock et al. (2001) from their Alderney experiment discussed in Chapter 2. It can be seen from the figure that the values reported in Table 3.1 are reached 0.2 s after the impact and that the duration of the whole impact event is equals to 0.8 s.

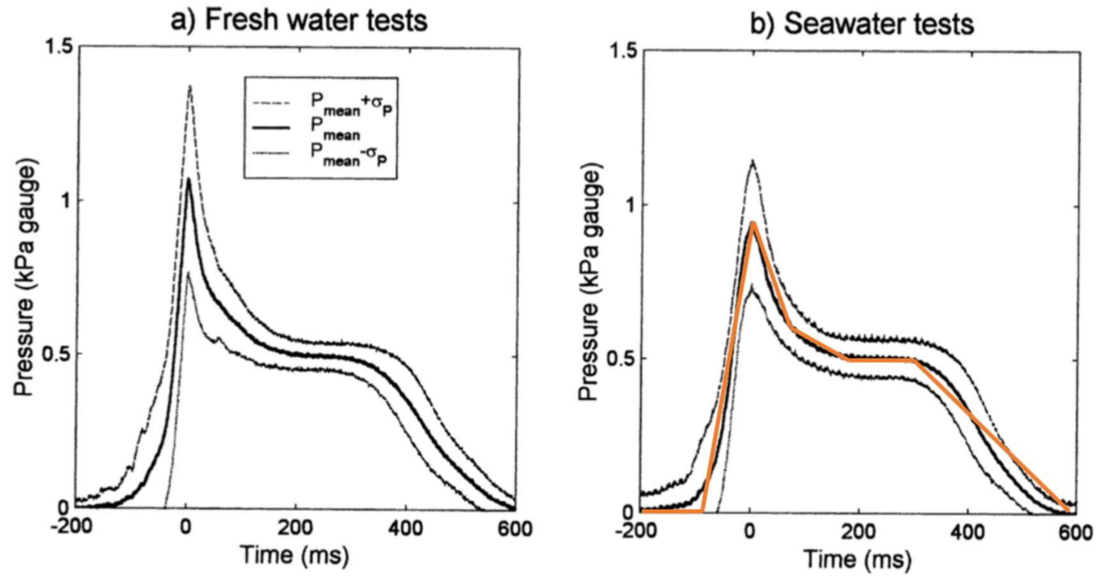

Figure 3.3.7 Variation in pressure based on a sample of 200 regular laboratory waves. (Bullock et al, 2001)

Moreover, the hydrostatic pressure due to the seawater under the design water level was considered too. The hydrostatic pressure was applied only on the front face of the wall, on the two sides of the structure it has the same intensity but opposite direction and so the resultant pressure is zero. The hydrostatic pressure was calculated as follow:

$$q = \rho g h \text{ (4)}$$

where ρ is the seawater density, g is the gravitation acceleration and h is the elevation at which the pressure is calculated.

3.4. Wave pressure on the wall

The wave pressure on the harbour wall has been calculated according to Goda (2010). According to the Theory a trapezoidal pressure distribution along a vertical wall was assumed, as shown in Figure 3.4.1. The information about the bedrock trend is known by the LIDAR data.

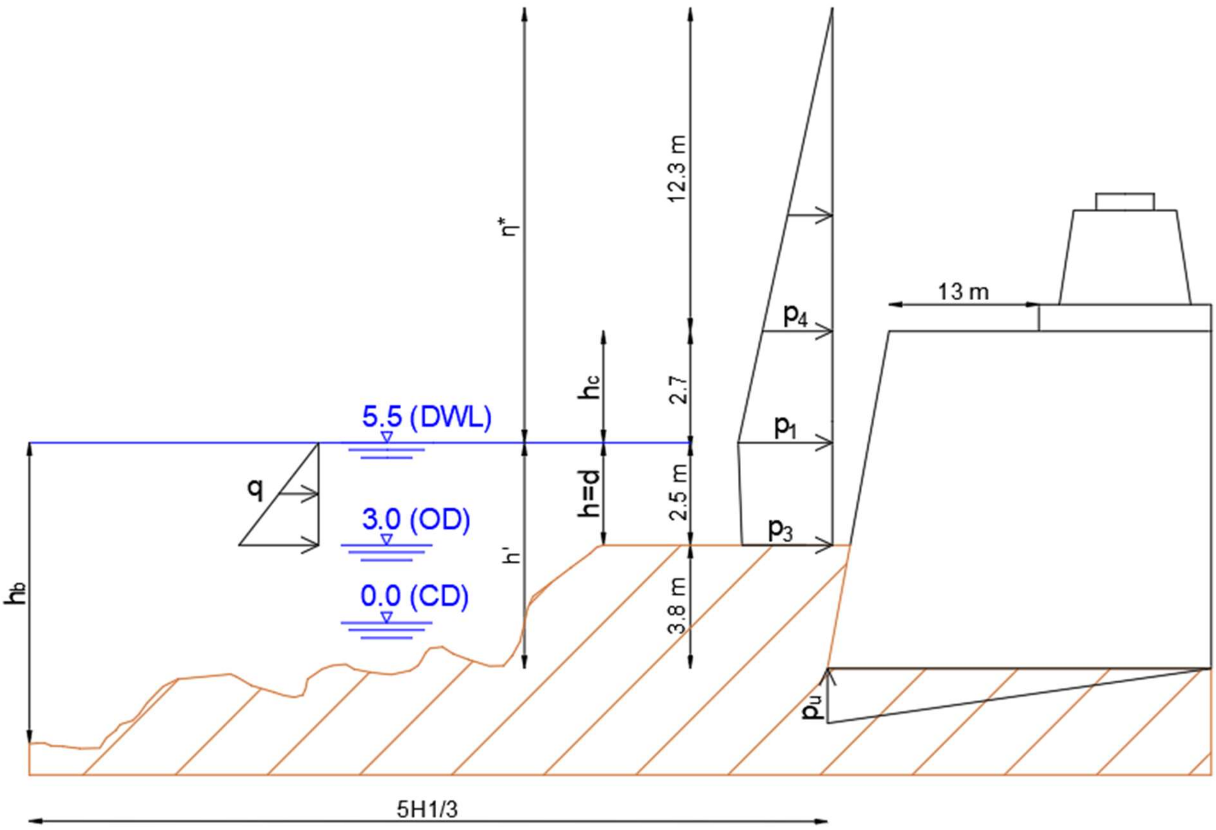

Figure 3.4.1 Parameters on the front of the wall, side view (not in scale). 1st scenario

As explained by the author, in Figure 3.4.1 *h* is the water depth in front of the wall; *d* is the depth above the rock at the base of the wall; *h'* is the distance from the design water level to the bottom of the upright section; h_c is the crest elevation of the breakwater above the design water level and η^* was calculated as followed:

$$\eta^* = 0{,}75(1 + \cos\beta)H_{max} \quad (5)$$

where β indicates the angle between the direction of the wave approach and a line normal to the breakwater. Since there is uncertainty in the estimation of the design wave direction, this should be rotated by an amount of up to 15° toward the line normal to the breakwater from the principal wave direction. A value of $\beta = 14^o$ was calculated as shown in Figure 3.4.2. However, that value does not make difference in the results and so the worst situation with $\beta = 0^o$ was considered in the analysis (wave hits the front of the wall orthogonally). Wave geometric information are available at *Channel Coastal Observatory*. The closest buoy to Portreath that had wave data with the storm of interest was the one in Perranporth, 13 km far from Portreath. Looking at Figure 3.4.3-4 it is possible to see the wave height, the tide level, the wave period and the wave direction for the event on January 3rd 2014.

Particularly, the wave direction is 285° from the North. The event has a return period of 50 years (Channel Coast Observatory, 2019).

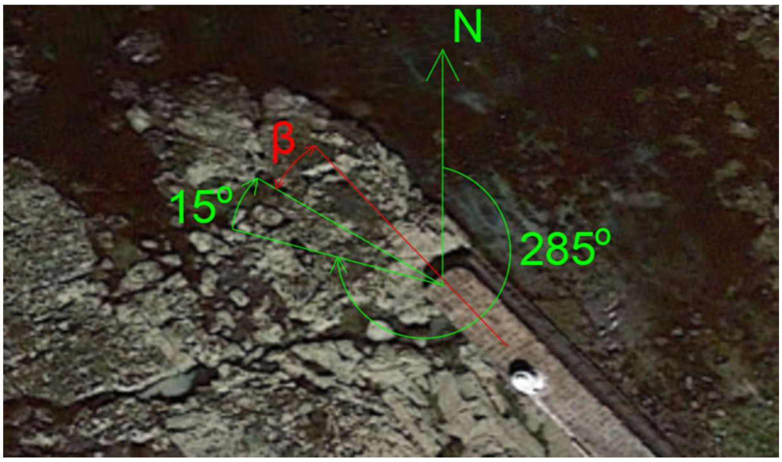

Figure 3.4.2. Wave direction and β calculation

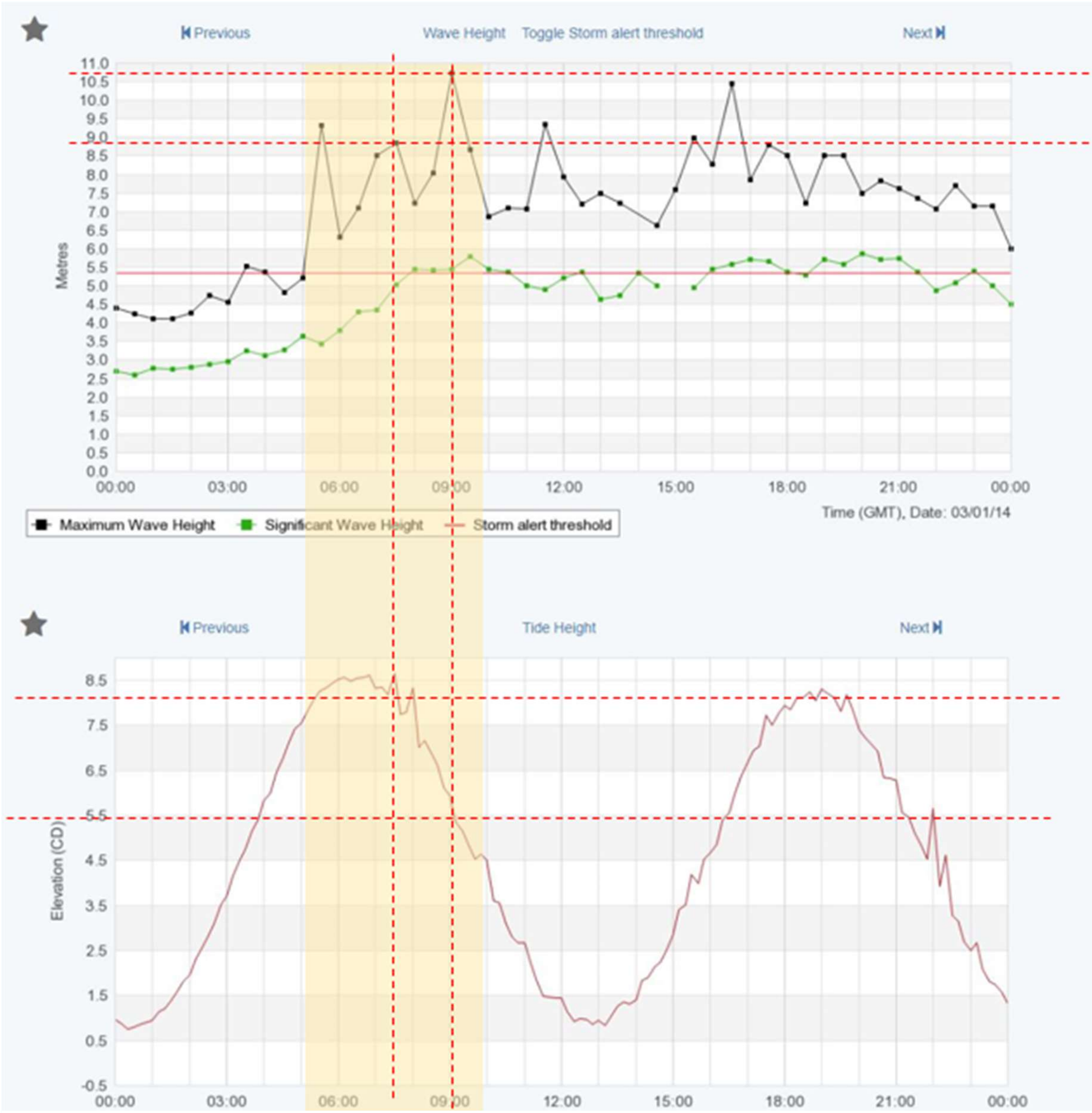

Figure 3.4.3. Wave height (top) and tide level (bottom). (Channel Coastal Observatory, 2019)

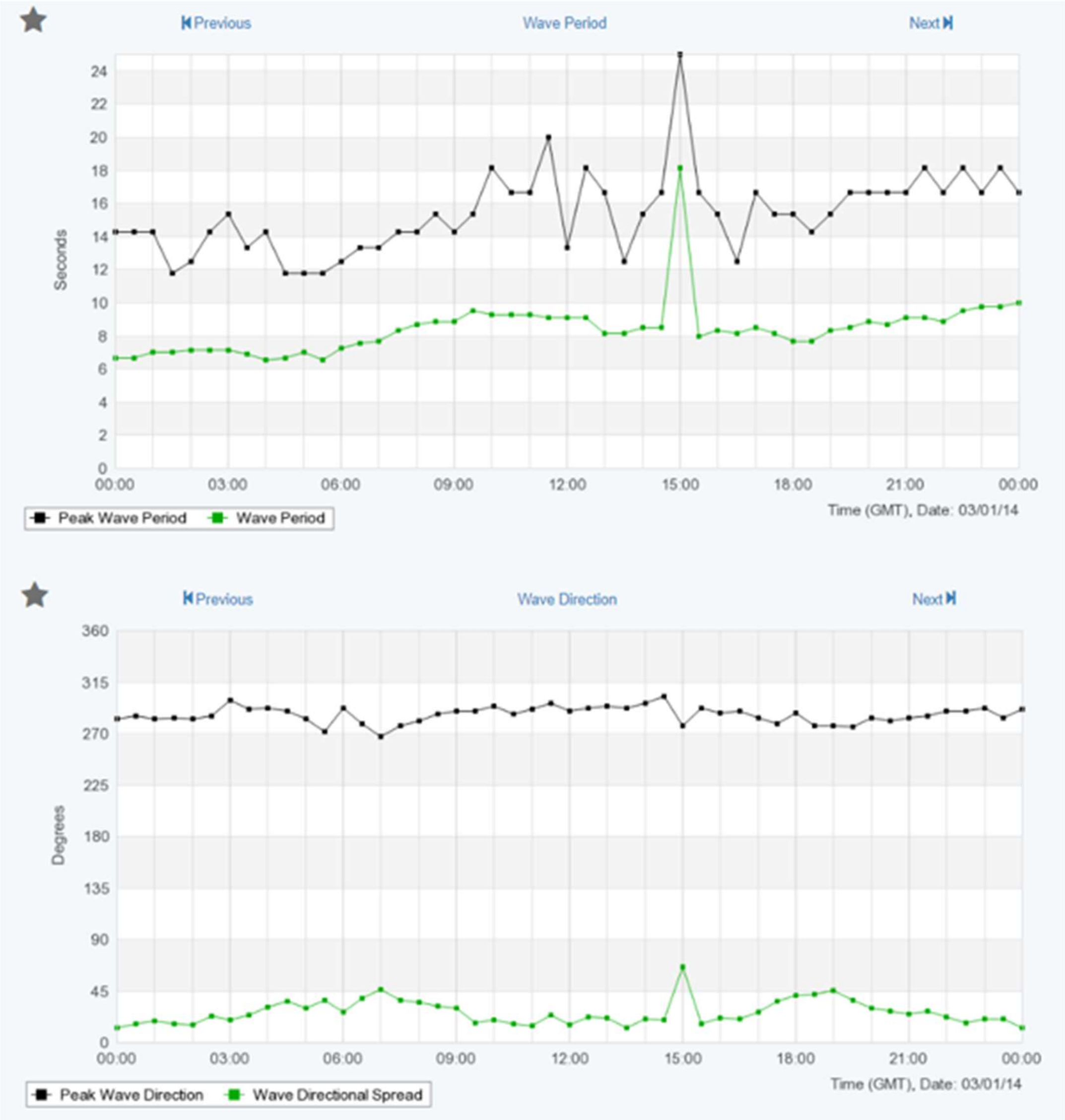

Figure 3.4.4. Wave period (top) and wave direction (bottom). (Channel Coastal Observatory, 2019)

In Figure 3.4.3 it should be observed how the highest wave (10.5 m) is correlated with a tide level equals to 5.5 m while the highest tide level reached is about 8.2 m and is correlated with a wave height equals to 9 m. Figure 3.4.1 refers to the first scenario while the second scenario is shown in Figure 3.4.5. Both cases were considered in the analysis in order to find the worst situation for the front face.

Chart Datum (CD) defines the level of the sea by assuming that the water level is at 0.0 m. However, water level changes several times during the day and months for several reasons. Tides and storm surges are the main causes. That variation is also because the higher wave pressure is exerted not by waves just breaking at the site, but by waves which have already begun to break at a short distance from the wall. In order to take into account all these aspects, an Ordnance Datum (OD) is defined with a value of the water level 3 m higher than the zero level. LIDAR data refers to the Ordnance Datum. The British Oceanographic Data Centre (2019), confirmed that, for the village of Newlyn (the closest village to Portreath where the mensuration was done), the Chart Datum is 3 m below the Ordnance Datum. Nevertheless, in the calculation a design water level (DWL), equals to the actual water level during the event (tide height), was considered. The DWL water level at each time is shown in Figure 3.4.3 (bottom).

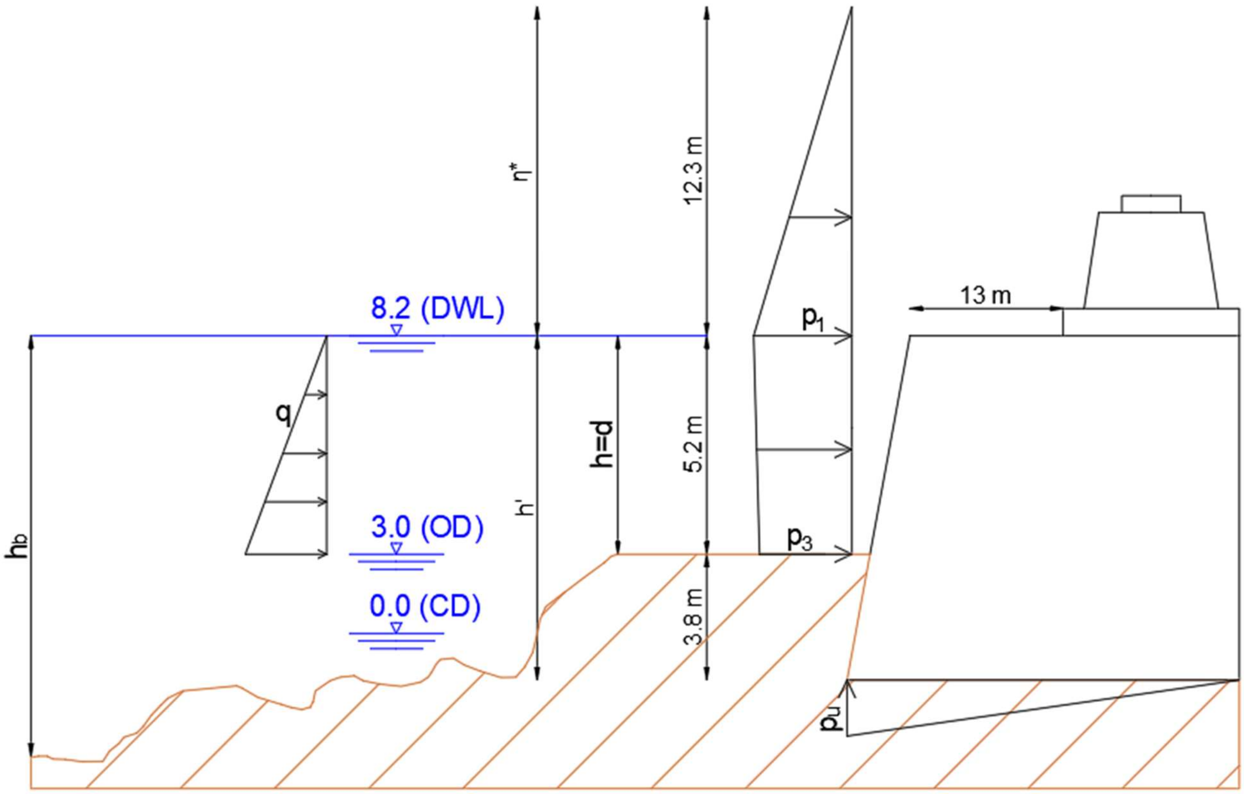

Figure 3.4.5 Parameters on the front of the wall, side view (not in scale). 2nd scenario

The theory assumes $H_{max} = 1{,}8H_{1/3}$ from seaward of the surf zone according to the empirical data. In order to calculate the value of $H_{1/3}$, the wave heights were sorted from the higher value to the lower, and the mean of the first third of the wave heights was taken. $H_{1/3}$ is, thus, the maximum probabilistic value of the wave. Therefore, except when storm waves equivalent to the design condition hit the site, in all the calculations, $H_{max} = 1{,}8H_{1/3}$ was considered a value on the safe side. For this event, $H_{1/3} = 5.8\, m$. In Figure 3.4.1-5 *q* indicates the hydrostatic water pressure while *p* is the wave impact pressure calculated with Goda's theory.

The wave pressure value on the front of the vertical wall was calculated in the following way:

$$p_1 = \frac{1}{2}(1+\cos\beta)(\alpha_1 + \alpha_2 \cos^2\beta)\rho g H_{max} \quad (6)$$

$$p_2 = \frac{p_1}{\cosh\left(\frac{2\pi h}{L}\right)} \quad (7)$$

$$p_3 = \alpha_3 p_1 \quad (8)$$

$$p_4 = \begin{cases} p_1\left(1-\frac{h_c}{\eta^*}\right) & : \ \eta^* > h_c \\ 0 & : \ \eta^* \le h_c \end{cases} \quad (9)$$

in which:

$$\alpha_1 = 0{,}6 + \frac{1}{2}\left[\frac{\frac{4\pi h}{L}}{\sinh\left(\frac{4\pi h}{L}\right)}\right]^2 \quad (10)$$

$$\alpha_2 = \min\left\{\frac{h_b - d}{3h_b}\left(\frac{H_{max}}{d}\right)^2 \middle| \frac{2d}{H_{max}}\right\} \quad (11)$$

$$\alpha_3 = 1 - \frac{h'}{h}\left[1 - \frac{1}{\cosh\left(\frac{2\pi h}{L}\right)}\right] \quad (12)$$

The value of h_b is the water depth at a distance of $5H_{1/3}$ from the wall. The calculated pressure is assumed not to change regardless of wave overtopping. The wavelength, corresponding to the significant period in deep water, is calculated as:

$$L_0 = 1.56T_P^2 \quad (13)$$

where T_P is the period of the wave (equals, in this case, to 14.3 second).

The value of the coefficient α_1 and the value of $\frac{1}{\cosh\left(\frac{2\pi h}{L}\right)}$ in α_3 are obtained from, respectively, Figure 3.4.6 and Figure 3.4.7.

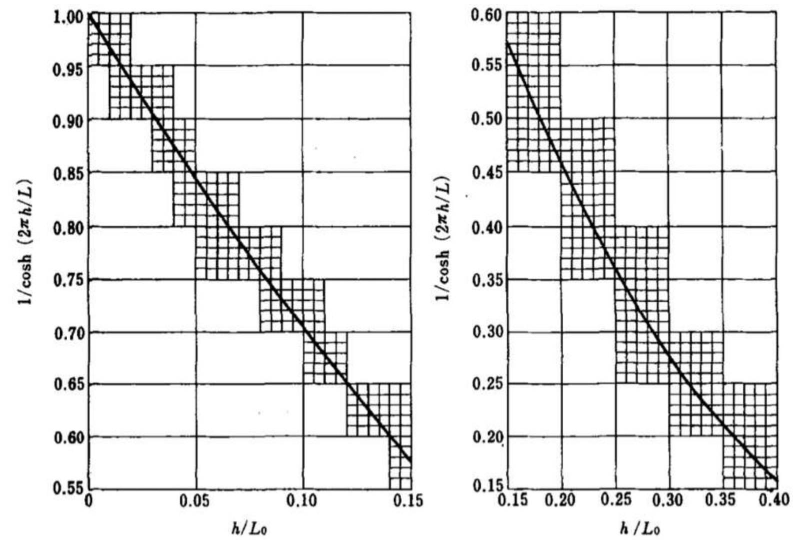

Figure 3.4.6 Calculation diagram for the parameter α_1 (Goda, 2000)

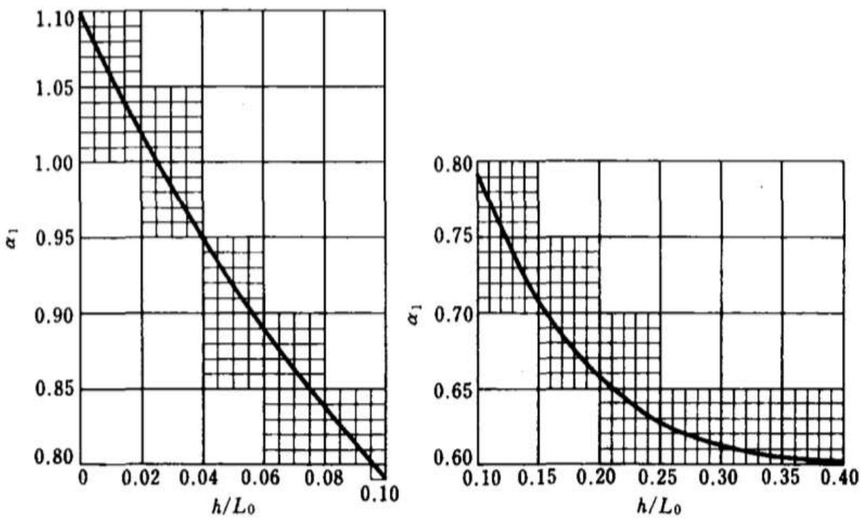

Figure 3.4.7 Calculation diagram for the parameter $1/cosh(2\pi h/L)$ (Goda, 2000)

At the bottom of the upright section, the theory assumes a triangular distribution of the uplift pressure as given by Eq. (14)

$$p_u = \frac{1}{2}(1+\cos\beta)\alpha_1\alpha_3\rho g H_{max} \quad (14)$$

Considering the above pressure distribution, the value of the total wave pressure and its moment around the bottom of an upright section were defined with the following equations:

$$P = \frac{1}{2}(p_1+p_3)h' + \frac{1}{2}(p_1+p_4)h_c^* \quad (15)$$

$$M = \frac{1}{6}(2p_1+p_3)h'^2 + \frac{1}{2}(p_1+p_4)h'h_c^* + \frac{1}{6}(p_1+2p_4){h^*}_c^2 \quad (16)$$

where:

$$h_c^* = \min(\eta^*, h_c) \quad (17)$$

In the same way, for the uplift pressure:

$$U = \frac{1}{2}p_u B \quad (18)$$

$$M_U = \frac{2}{3}UB \quad (19)$$

where B is the width of the bottom of the upright section.

In this study the uplift pressure was not considered.

The pressure here defined (condition of Wave Crest) can change after that the trough of an incident wave hits the wall. The pressure on the wall becomes less than the hydrostatic pressure under the still water level and the vertical wall experiences a net pressure directed offshore (condition of Wave Trough). Since in the study only the condition with wave on the front of the structure is analysed this effect is not considered, indeed the offshore pressure is negligible considering the length of the structure and it makes impossible to have a sliding seaward.

3.5. Analysis and results

3.5.1. Validation of the model

In order to validate the model, an appropriate theory should be considered. The geometry of the structure is quite tricky and a theory to use, in order to calculate physic parameters of the wall (e.g. displacement, strain) to compare with the ANSYS results, was not found. Considering the front of the wall as vertically straight, with a rectangular shape and with the load as uniformly or triangular distributed, it is possible to solve the structure using the theory of the plate. However, the model under these hypotheses is far from our actual problem and anyway solutions are given for boundary conditions different from our case. A way can be to solve the differential equation of the plate theory for the condition in exams in order to have a reasonable correlation but this solution goes beyond the aim of this preliminary work. It should be also considered that our structure is made of block and mortar, and so a homogenization is required for the comparison.

In summary, for this preliminary work, a validation was done considering the only self-weight of the structure, and so without loading the model with the wave pressure, and calculating the elastic vertical strain in a plane vertical section of the structure. In Figure 3.5.1 are reported the values obtained by a hand-calculation versus the values obtained by ANSYS considering different meshes.

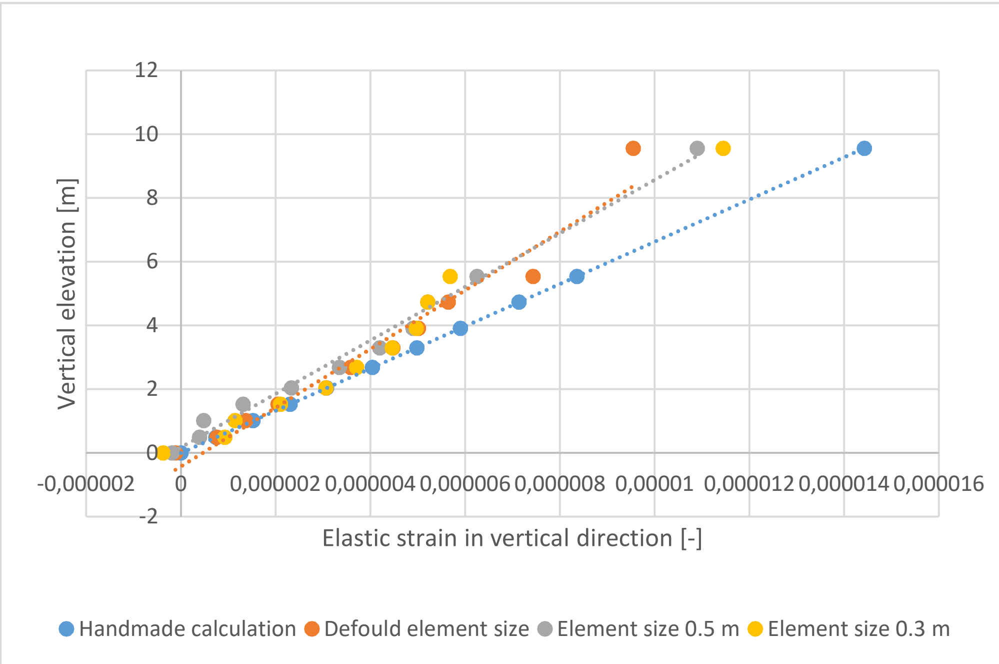

Figure 3.5.1 Correlation for the vertic strain between ANSYS results and the elastic theory

It seems that the results are quite close, and anyway the differences are on average less than 10% with the only exception for the strain at the top of the wall. For this last value, finer results are achieved for finer mesh. It is worth remembering that the section of the model where the results were taken is in the part with only a homogenised material and so for the hand calculation a Young's Modulus (E) equals to 13 GPa was assumed in the following equation:

$$\varepsilon_y = \frac{\rho g x}{E} \quad (20)$$

where ρ is the density of the material (2000 kg/m^3), g is the gravitational acceleration (9.81 m/s^2) and x is the elevation of the wall where the strain is calculated.

Because of the complex geometry on the front of the wall (several blocks with a mortar thickness very small) the mesh element sizes were limited by the running time and the software licence limits. The chosen mesh is described in section 3.3.1.

3.5.2. Analysis

An explicit dynamic analysis is usually used for computing the dynamic response of a structure under dynamic and impact load such as waves. This analysis takes into account the exchange momentum and the inertial effect between the bodies and it also considers all the nonlinearities of the model. However, considering the huge geometry of the wall, the results are practically the same of the ones obtained from a static structural analysis. Moreover, the study is not focusing into the dynamic of the structure. Hence, in order to save running time (the complexity of the front face makes a dynamic analysis quite long), a static structural analysis was performed. The force-time law is anyway used in the model as shown in Figure 3.3.7.

The model was first tested with a simpler analysis. The comparison between the two models, in terms of displacement and normal stress in x direction (the load direction), is reported in the following figures. For the rough model, only consider the results for the front face and not for the Monkey Hut. For both models the same mesh was used.

Figures 3.5.1-2 show how the displacement for the finer model is bigger, probably because of the geometry made of block and mortar and not with one only material. Moreover, in the rough model the displacement is almost constant for each course of block while, in the finer model, it is possible to see that the displacement is higher for the mortar and lower for the blocks and it increases toward the edges of the wall. Looking at the stresses (Figure 3.5.3-4), the values are almost the same for the top part of the structure while big differences are evident on the bottom 5 courses. Overall, it can be said that the loaded part is compressed while the bottom part is tensed. It must be noticed how, though the blocks are compressed, the mortar layer is almost always slightly tensed.

It is worth to see how the structure does not reach the material strength value and it stays for all the analysis into the elastic field. This leads to deduce that the damage on the Monkey Hut were not due to the highest wave load. Indeed, the complete destruction of the structure occurred on Jan 7th, for a smaller wave impact, after that the structure has been resisting to waves for 5 days. The failure of the structure is so due to a fatigue collapse.

In Figure 3.5.6-7 is also shown the maximum principal stresses on the structure and over the Monkey Hut. It can been observed that all values are below the material strength properties.

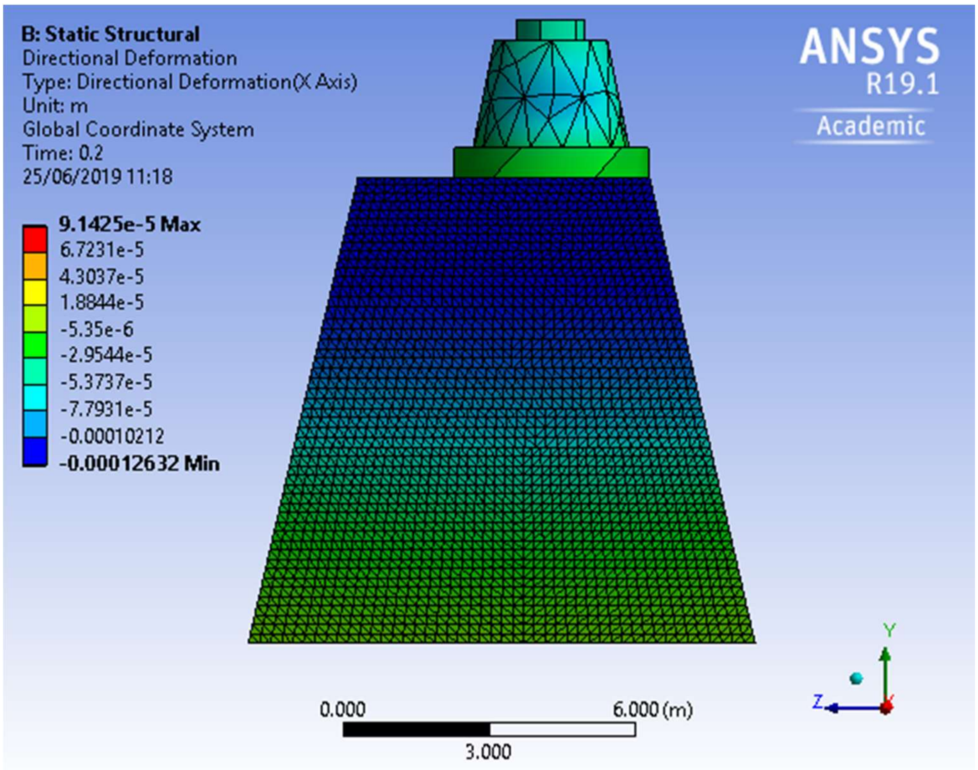

Figure 3.5.1. Deformation in x direction for the rough model

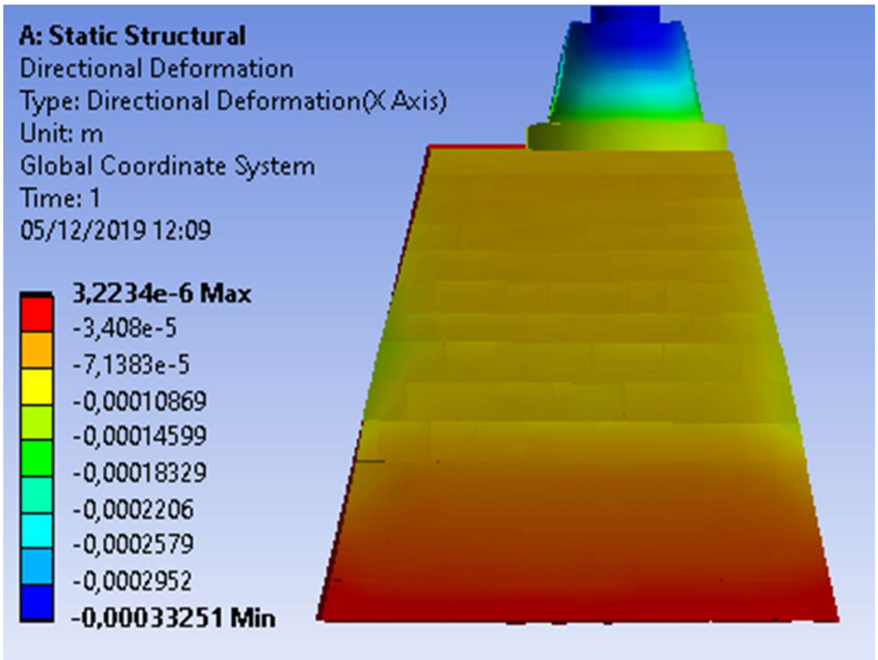

Figure 3.5.2. Deformation in x direction for the finer model

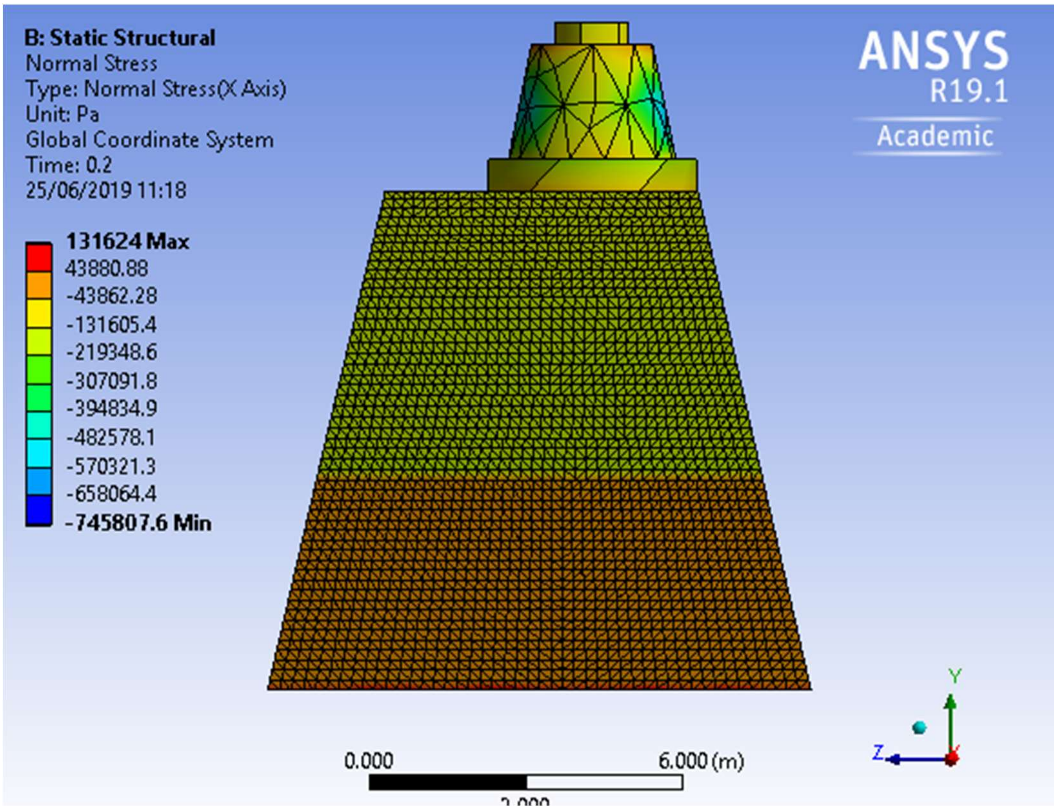

Figure 3.5.3 Stress in x direction for the rough model

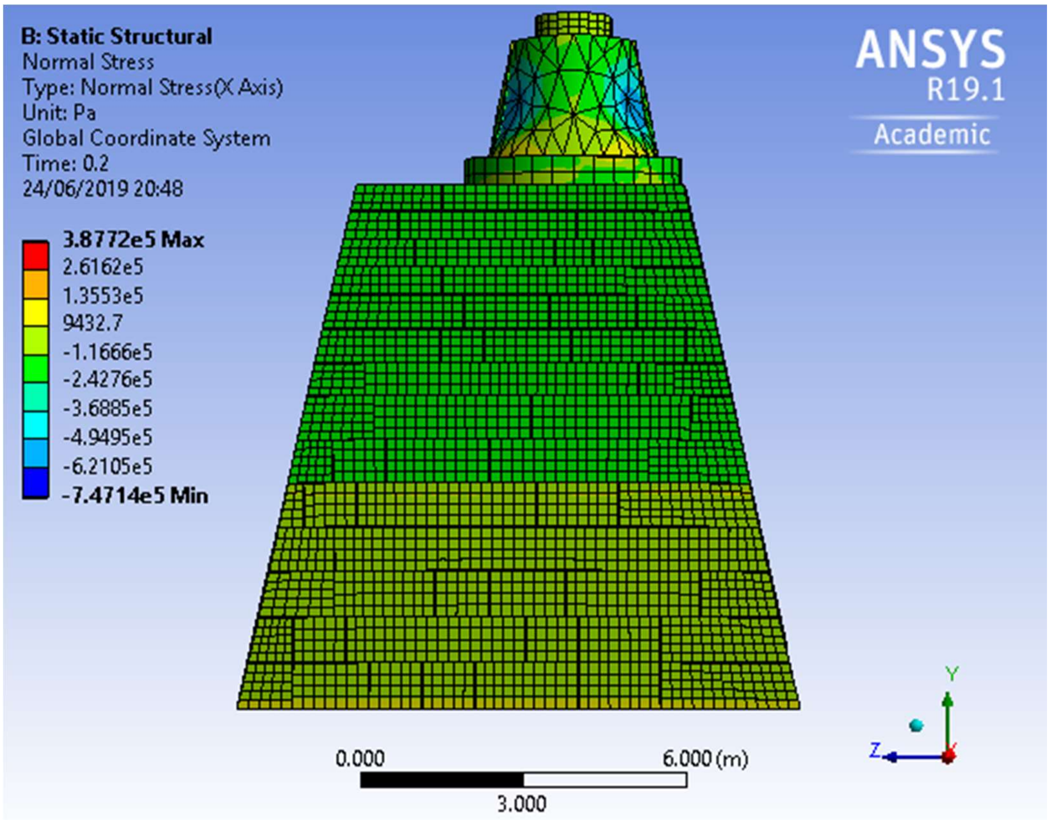

Figure 3.5.4. Normal stress in x direction for the finer model

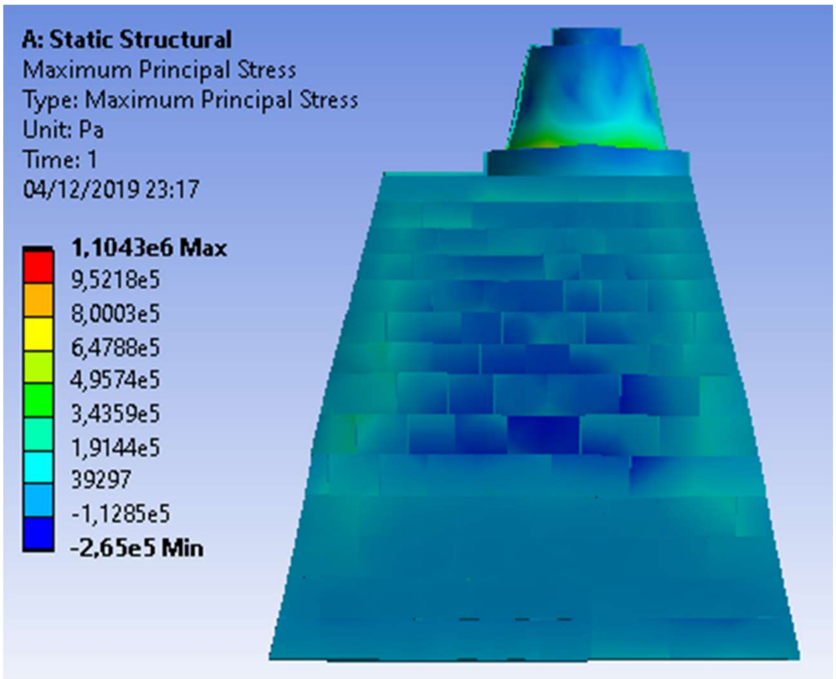

Figure 3.5.6. Maximum principal stress for the finer model

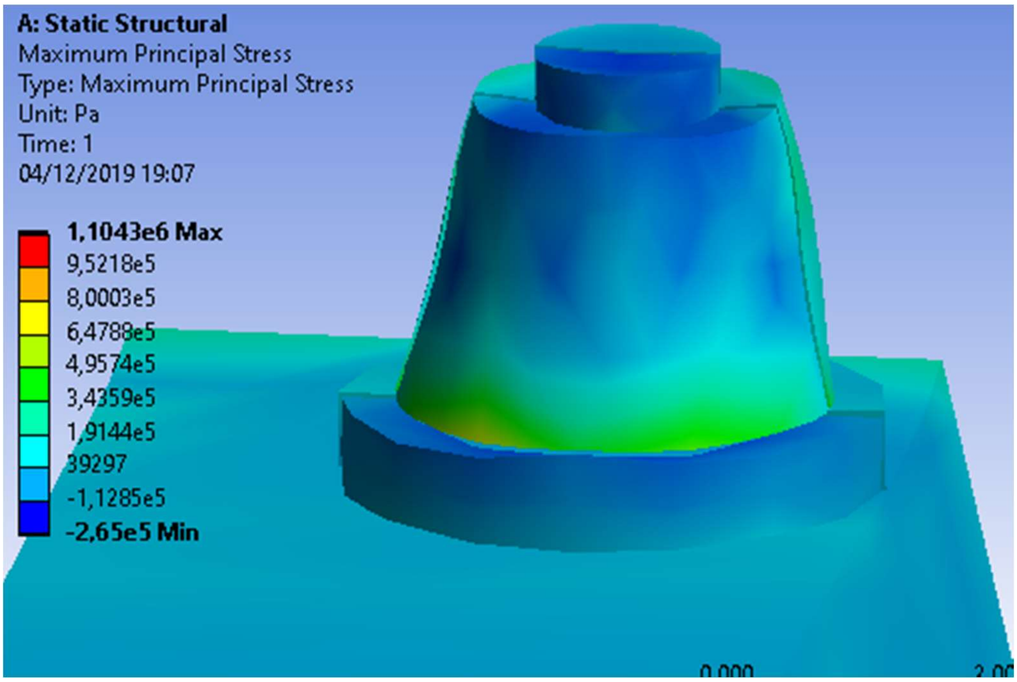

Figure 3.5.7. Maximum principal stress for the Monkey Hut

3.5.3. Verification

Masonry is a very complex material and block and mortar have different structural behaviour. Blocks have a brittle failure while mortar exhibits a more ductile failure. Both elements work well in compression while they have a small resistance in tension. Approximately, the overall behaviour of a masonry structure can be described with the Mohr-Coulomb criterion (Carpinteri, 1993):

$$|\tau| = c - \sigma \cdot tg\varphi \quad (21)$$

where *c* is the cohesion of the material (assumed equals to 15 MPa), φ is the inner friction angle (equals to 40º) and σ is the stress considered (taken from ANSYS). The safe domain of the criterion is represented on the Mohr-Coulomb plane. The safe domain has a cut-off on the compression side (assumed positive) for a value of σ equals to the compression strength of the material and a cut-off on the tensile side (assumed negative) for a value of σ equals to the tensile strength of the material. The bottom and top line of the domain have an inclination equals to $tg\varphi$ and they cut the τ axis for a value of $\tau = c$ according to Equation (21). The highest (positive) compression stress (and the corresponding τ stress) and the lowest (negative) tensile stress (and the corresponding τ stress) were plotted in the domain and it is possible to see how they are quite far from the failure edges. Results are shown in Figure 3.5.8 and Table 3.5.1.

Looking at Figure 3.5.7 it is possible to see how both the maximum principal tensile and compression stresses arise in the Monkey Hut while the rest of the wall does not show material problem and the stresses are quite below its strength properties. Particularly, the highest tensile stress arise in the connection between the Monkey Hut and the concrete base and that is exactly the surface where the waves detached the structure on January 7th 2014.

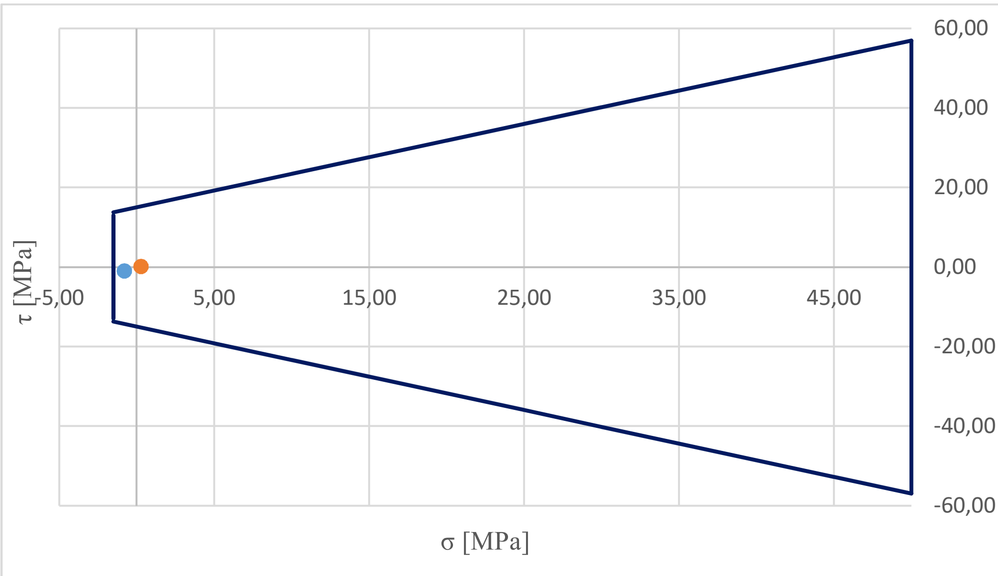

Figure 3.5.8. Mohr-Coulomb domain

Table 3.5.1 Material verification

	ANSYS Stress	Cut-off value	Safe coefficient
Tensile stress	-0,8 MPa	-1,5 MPa	1,9
Compression stress	0.27 MPa	50 MPa	185

Tensile block strength was assumed to be 1/35 of the compressive strength. The material has a large safe coefficient in compression. Anyway, although the tensile safe coefficient is smaller, the structure is not failing for this wave conditions. This can be better explained considering that the Monkey Hut was not detached during on January 3rd 2014 but on January 7th, after four days of storm for a smaller wave impact of the one in analysis as already mentioned. In conclusion, since tensile stresses are already close to the tensile strength of the material, it can be assumed that at some point the material cracked. Once the material cracked, and the material tensile strength started decreasing, the water which filled the fissure started increasing the crack width and as consequence the internal pressure increased too (according to the studies discussed in Chapter 1). Hence, the structural strength has been decreasing while the internal pressure has been increasing for 5 days till the Monkey Hut detached.

The non-linear behaviour of the structure can be better analysed considering other failure criterions, for example the Druncker-Prager criterion.

The bearing capacity at the base of the wall was also verified. Since the wall is based on a rigid bedrock, the ratio between the limit bearing capacity of the sandstone bedrock ($q_{\lim}$) and the load that arrives in foundation from the wall (q_s) gave a safe factor equals to 72. The bearing capacity of the rock was calculated as:

$$q_{\lim} = \frac{1}{2}\gamma B N_{\gamma} \quad (22)$$

where γ is the sandstone bedrock unit weight (19.6 kN/m^3) , *B* is the width of the wall (10 m) and N_{γ} is a parameter function of the bedrock inner friction angle (Lancellotta e Calavera, 2016). q_s was calculated considering the self-weight due to 1 m of wall section divided the base section area.

Considering the scheme in Figure 3.5.9 the overturning and the sliding verification were checked. In both verifications, the vertical stabilizer load was the self-weight of the 1 m section of the wall, while the horizontal destabilizing load was due to the wave pressure. The wave pressure distribution was calculated as explained in paragraph 3.4 considering the geometric condition of the side of the wall.

The overturning verification gave a safe coefficient equals to 1.8 calculated as follows:

$$FS_{overturning} = \frac{V b_V}{F_1 b_1 + F_2 b_2} \quad (23)$$

where $F_{1,2}$ are the resultants of the first and second trapezoidal load and $b_{1,2}$ are the respective level arms (the overturning is calculated respect the bottom left corner of the wall). V is the self-weight of the 1 m section of the wall and b_V is its level arm. In the same way, the sliding verification gave a safe coefficient equals to 1.9 calculated as follow:

$$FS_{sliding} = \frac{V \cdot tg\varphi}{F_1 + F_2} \qquad (24)$$

where φ is the already defined inner friction angle of the block (40°).

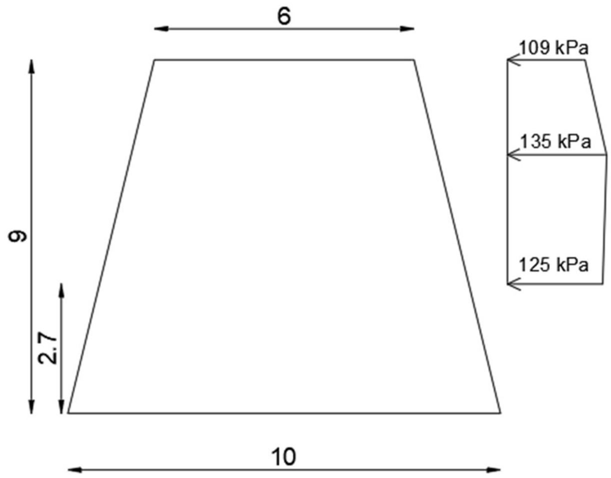

Figure 3.5.9. Overturning and sliding scheme

However, since the wall is not a monolithic structure but is made of course of blocks and mortar, the sliding can appear in other sections and not only at the base section. Moreover, the resistance to the horizontal wave action is assumed to being borne from the only blocks because of the high degradation of the mortar and of its low cohesion.

The overturning and sliding verification were also done on the Monkey Hut. Using Equation (23) the overturning verification was not satisfied, indeed it gave a safe coefficient equals to 0.27 and this justify the destruction of the structure for that wave in 2014. In the same way, using Equation (24) the safe coefficient for the sliding verification was 0.35.

The verifications were done considering the only Monkey Hut without the concrete base between it and the wall, and only for this geometry were calculated the self-weight and the portion of wave load used in the equations. The overturning was calculated respect the opposite point, at the base of the structure, of the one where the load hit the structure. The sliding verification was performed considering a friction between the structure and the concrete base equals to 0.6.

It must be said that all these verifications were done without considering the actual connection grade between the structure and the rest of the wall. This justify the apparent discordance with the FEM results.

4. Finite element model of the 3rdb part of the wall

The second part of this work focuses on the new part of the wall rebuilt after the damage due to Storm Eleanor in 2018. Goda's theory cannot be applied for this second case because the analysed part of the wall is not directly exposed to the wave impact. Indeed, the rebuilt wall is at the toe of the structure and, in normal condition, the water level does not reach this part of the structure. However, during the storm on January 2018, the tide level reaches the car park level and the whole beach was filled of seawater. For this reason, while the front of the structure was still subjected to the wave impact as well as to the hydrostatic pressure, at the toe the loading condition was different.

In order to get the value of the water pressure that destroyed the wall, the only hydrostatic pressure was considered acting on the wall. Looking at Figure 4.3.2 it is possible to see how in addition to the hydrostatic pressure, there is an additional load coming from the deviation toward the structure of the water impacting against the car park wall and canalizing over the stairs. That additional load was progressively increased until the failure of the structure was reached. The found critical load was then used in order to verify the new reinforced concrete wall.

For sake of comparison with the 2014 event, the characteristics of the event in exam happened on January 3rd 2018, are reported in the following Table.

Table 4.1. Storm characteristics (Channel Coastal Observatory, 2019)

Date/Time	H_s (m)	T_p (s)	T_z (s)	Dir. (º)	Water level elevation* (OD)	Tidal stage (hours re. HW)	Tidal range (m)	Tidal surge* (m)	Max. surge* (m)
03-Jan-2018 07:00	7.77	14.3	9.3	286	3.76	HW +1	7.36	0.11	0.42

The values of the wave heights and of the tide levels for the month of January 2018 are displayed in the following graphs:

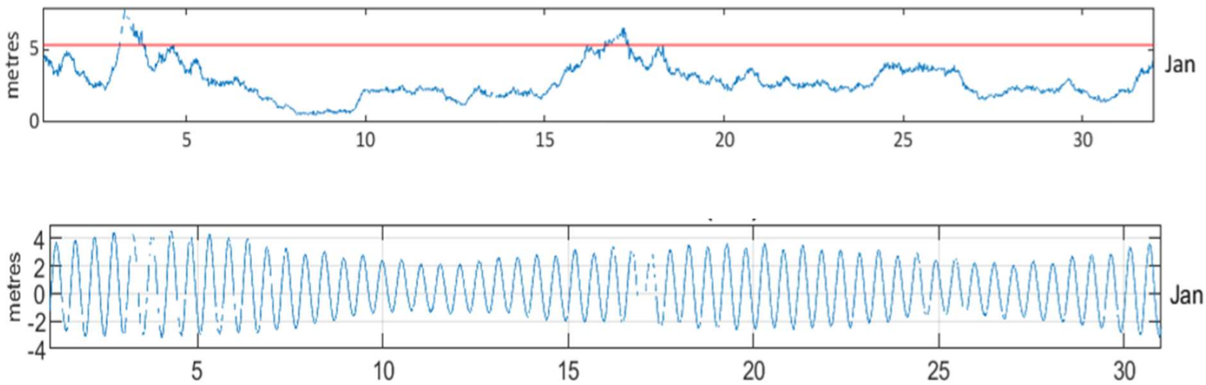

Figure 4.1. Wave height (top) and tide level (bottom) on January 2018 (Channel Coastal Observatory, 2019)

4.1. Geometry

The geometry was drawn in AUTOCAD and then exported into ANSYS exactly as for the previous model. There were modelled 25 m of wall. The failure arose between the two buttresses. The geometric values are reported in paragraph 1.1.1.

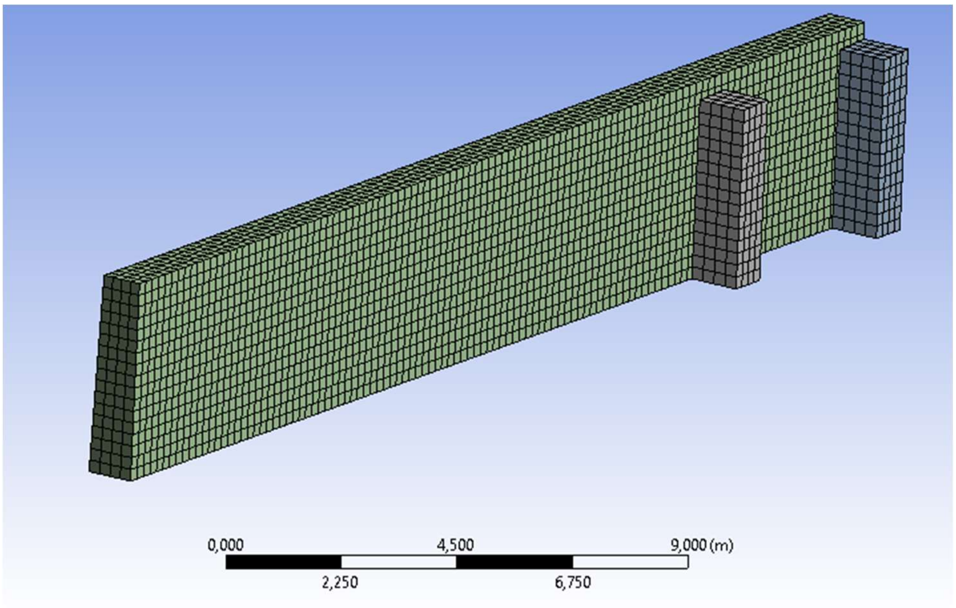

Figure 4.1.1. ANSYS 3D model

Along the length of the structure, the height of the wall above the soil level is always 4 m and only that part it was modelled. Since the soil level increases along the beach, the structure is not straight but it has a slope in order to keep having always the same height at each point.

For the rebuilt reinforced concrete wall a 2D model was crated as shown in Figure 4.1.2. A thickness of 150 mm (equals to the spacing between the rebars) was assigned to the model; in this way only one layer of reinforcement in the middle of the model was disposed (in light green in the picture).

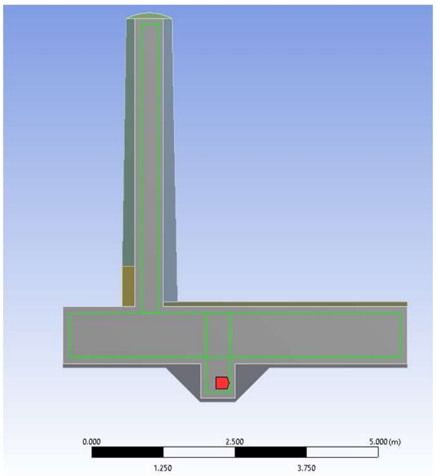

Figure 4.1.2. 2D model

4.2. Material

The model was created considering a unique material with the properties of the masonry assumed to be equal to the "dark stone" properties defined in paragraph 1.2 for the C and D part. The rock properties were reduced in order to consider the masonry properties, made of rock and mortar, as explained in paragraph 1.2.

Property	Value	Unit
Material Field Variables	Table	
Density	2000	kg m^-3
Isotropic Elasticity		
Derive from	Young's Modulu..	
Young's Modulus	3.2E+09	Pa
Poisson's Ratio	0.3077	
Bulk Modulus	2.7734E+09	Pa
Shear Modulus	1.2235E+09	Pa
~~Bilinear Isotropic Hardening~~		
Mohr-Coulomb		
Yield Surface		
Initial Inner Friction Angle	0.6	radian
Initial Cohesion	5E+05	Pa
Dilatancy Angle	0.26	radian
Residual Inner Friction Angle	0.43	radian
Residual Cohesion	50000	Pa

Figure 4.2.1 Masonry properties

For the rebuilt wall, known the concrete used, its properties were assigned to the wall elements as reported in Figure 4.2.3. The steel properties were also calculated known the reinforcement used. The sandstone cover was considered as a unique equivalent material (sandstone + mortar) with the properties shown in Figure 4.2.2 calculated in the same way of the previous model.

Property	Value	
Material Field Variables	Table	
Density	2000	kg m^-3
Isotropic Elasticity		
Derive from	Young's Modulus and Poisson's Ratio	
Young's Modulus	1.3E+09	Pa
Poisson's Ratio	0.23391	
Bulk Modulus	8.1426E+08	Pa
Shear Modulus	5.2678E+08	Pa

Figure 4.2.2 Sandstone cover properties

.

Property	Value	
Material Field Variables	Table	
Density	2400	kg m^-3
Isotropic Secant Coefficient of Thermal Expansion		
Isotropic Elasticity		
Derive from	Young's Modulus and Poisson's Ratio	
Young's Modulus	3.2E+10	Pa
Poisson's Ratio	0.18	
Bulk Modulus	1.6667E+10	Pa
Shear Modulus	1.3559E+10	Pa
Bilinear Isotropic Hardening		
Yield Strength	1.8E+07	Pa
Tangent Modulus	0	Pa
Tensile Yield Strength	3E+06	Pa
Compressive Yield Strength	1.88E+07	Pa
Tensile Ultimate Strength	3E+06	Pa
Compressive Ultimate Strength	1.88E+07	Pa

Figure 4.2.3. Concrete properties

Property	Value	
Material Field Variables	Table	
Density	7850	kg m^-3
Isotropic Secant Coefficient of Thermal Expansion		
Isotropic Elasticity		
Derive from	Young's Modulus and Poisson's Ratio	
Young's Modulus	2E+11	Pa
Poisson's Ratio	0.3	
Bulk Modulus	1.6667E+11	Pa
Shear Modulus	7.6923E+10	Pa
Strain-Life Parameters		
S-N Curve	Tabular	
Tensile Yield Strength	4.3E+08	Pa
Compressive Yield Strength	2.5E+08	Pa
Tensile Ultimate Strength	4.6E+08	Pa
Compressive Ultimate Strength	0	Pa

Figure 4.2.4 Steel properties

4.3. Model

4.3.1. Mesh

A mesh with quadrilateral element was used. The element size is equal to 0.25 m.

4.3.2. Element type and connections

A SOLID186 element was used, and its properties were explained in paragraph 3.3.2.

4.3.3. Support

Fixed supports were applied along the base for both the models. The foundations dimension and its depth below the ground level as well as the shear key justify this assumption. The connection between the modelled part and the rest of the structure was considered assuming no displacement along that direction.

4.3.4. Load

Self-weight was assigned to the whole structure. On the left side of the model (looking toward the sea) the hydrostatic pressure distribution was applied considering a seawater density equals to 1030 kg/m^3 and a gravitational acceleration equals to 9,81 m/s^2. On the same side, a constant pressure was assigned to the whole height, from the end of the structure to the second step of the stair (approximatively after the last buttress), as shown in the following Figure. The reason why this additional load was considered is because, looking at the available online videos of the event (YouTube, 2019), it is clear how the waves turned toward the structure from the car park wall, and flowed over the stairs. The scenario is better explained in Figure 4.3.2. In the picture it is also possible to see the destroyed part (between the red marks). The second step is at the level of the last buttress (into the red dot circle in the picture).

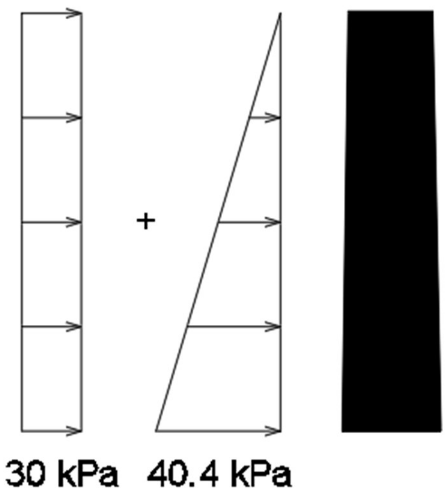

Figure 4.3.1. Load condition

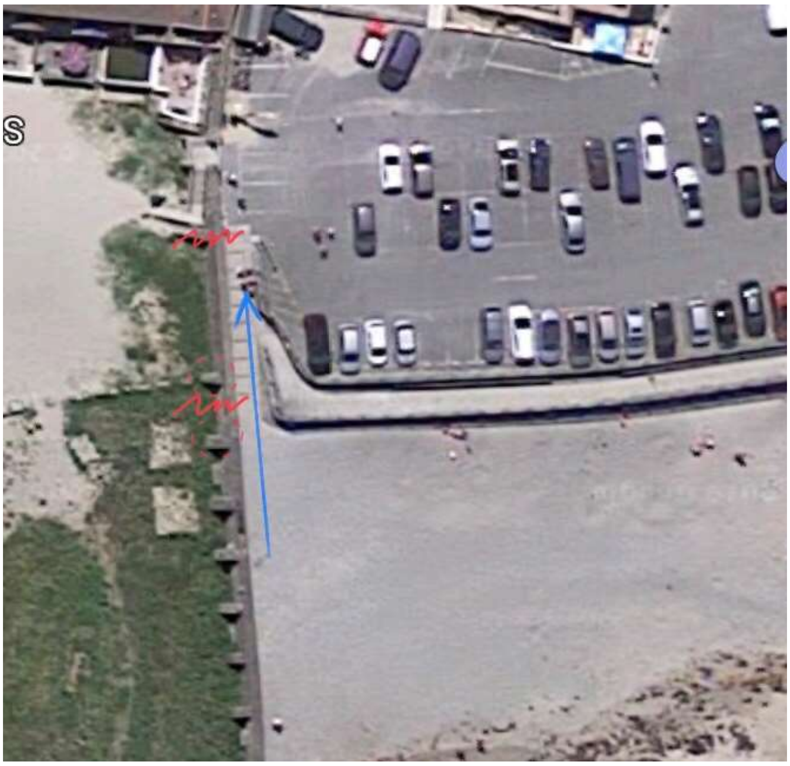

Figure 4.3.2 Wave condition

4.4. Analysis and results

The additional load was increased and an analysis was performed for each increased loading case. For an additional load equals to 10 kPa it was possible to start seeing a few plastic areas in the most critical part. Increasing the load, those plastic areas became bigger and for a load equals to 30 kPa it was possible to see the failure mechanism which probably occurred at the time. The structure shown a shear failure between the last and the previous buttress. Indeed, the shear stresses arisen were bigger than the masonry strength properties. Moreover, the shear mechanism might have been due to the asymmetric load condition: as the stair becomes taller, the hydrostatic load becomes smaller. So the structure was subjected to a triangular hydrostatic load acting only above the stair and to the additional load acting only before the last buttress.

Now that an order of the failure load has been got, the load should be calculated with an appropriate theory and a CFC analysis is required if more accurate results are requested. The results of the analysis are reported in the following plots.

It can be noticed that the assumed shear strength of the masonry is equals to 0.5 MPa while the structure reaches a shear stress slightly higher exactly in the section where the failure arose. Obviously, for the chosen load, verifications are not satisfied. The model can be validated considering the wall as a cantilever beam fixed into the soil. The displacements are obtained from the following equation (Carpinteri, 1993):

$$\delta = \frac{q}{EI}\left(\frac{z^4}{12} - \frac{z^3}{3}L + \frac{z^2}{2}l^2\right) \qquad (25)$$

where E is the masonry Young's Modulus, I is the moment of inertia, q is the distributed load (assumed to be uniform), z is the vertical elevation and L is the height of the structure.

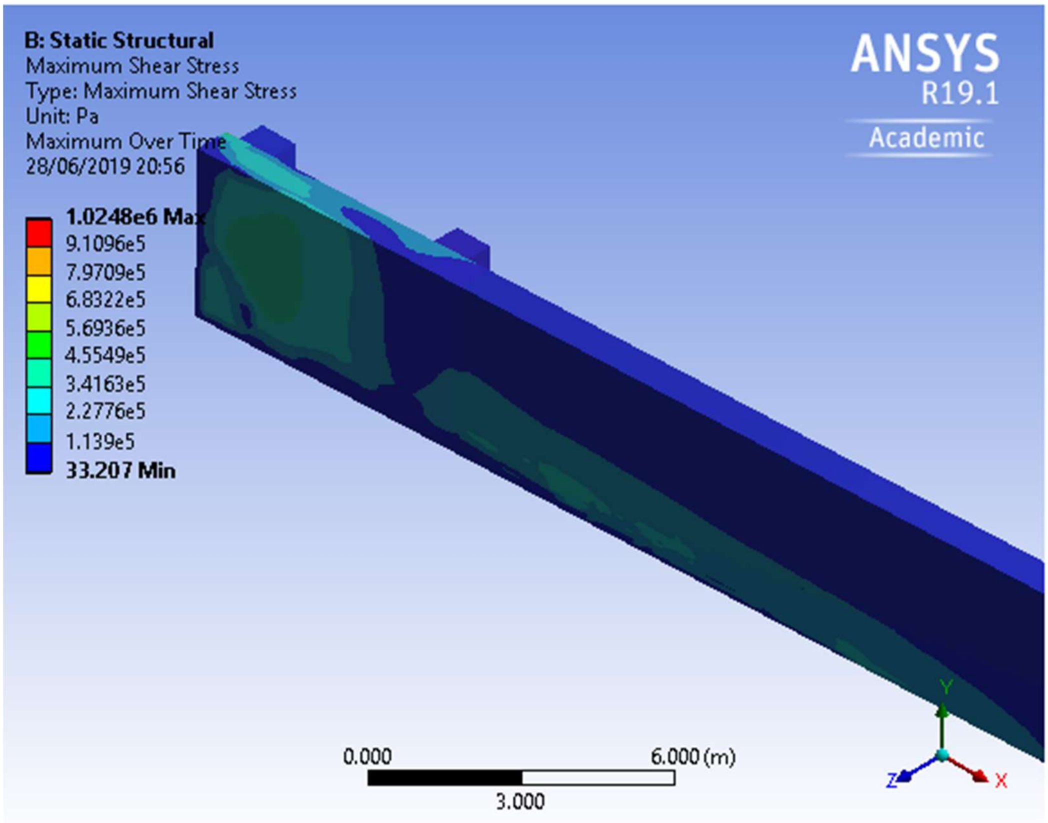

Figure 4.4.1 Maximum shear stress (old wall)

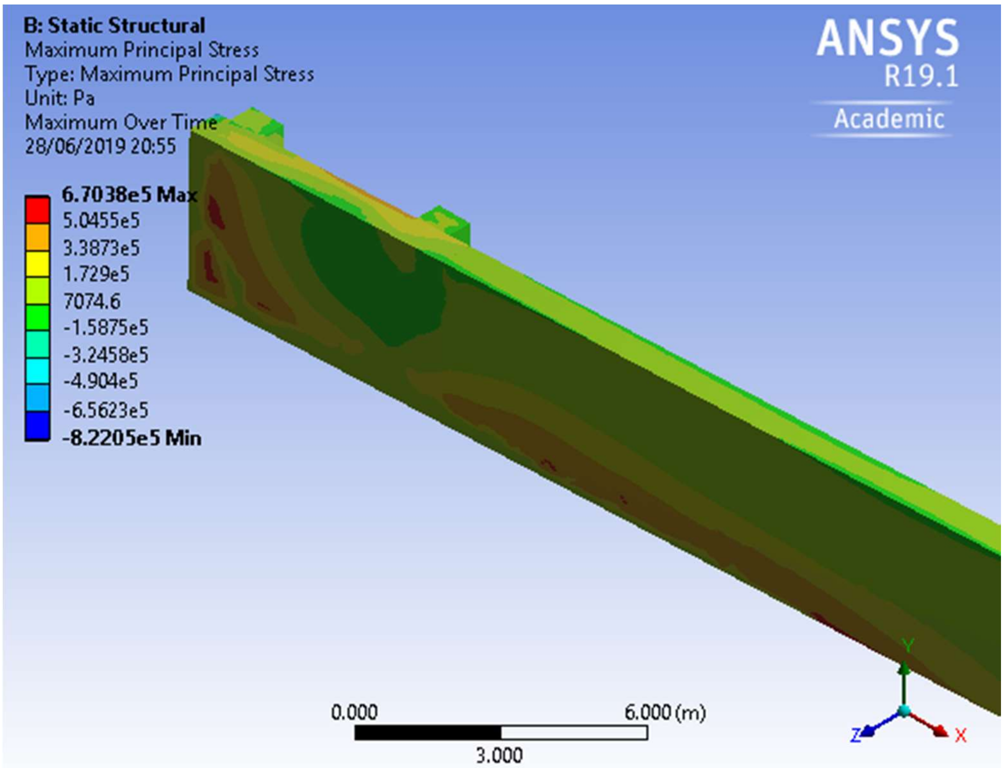

Figure 4.4.2 Maximum principal stress (old wall)

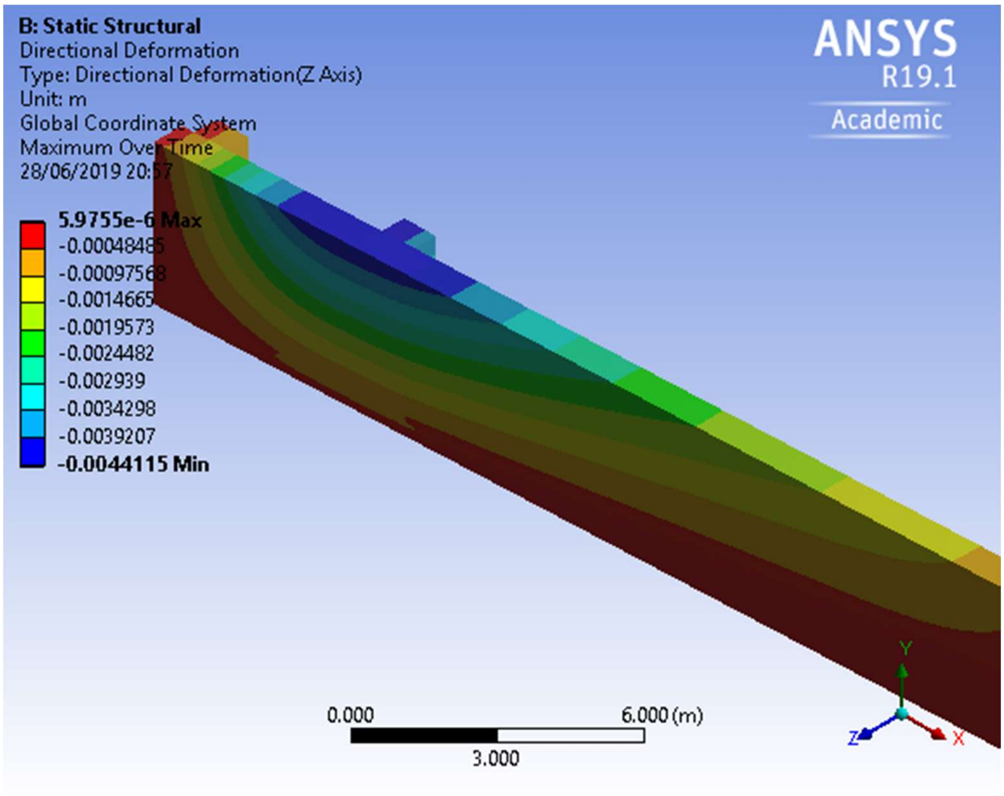

Figure 4.4.3 Displacement (old wall)

The found load was then assigned to the new reinforced concrete wall giving the following results. Looking at the tensile and compressive stresses, they are below the concrete and steel strength and verifications are now satisfied. The wall does not enter into the plastic field during the analysis.

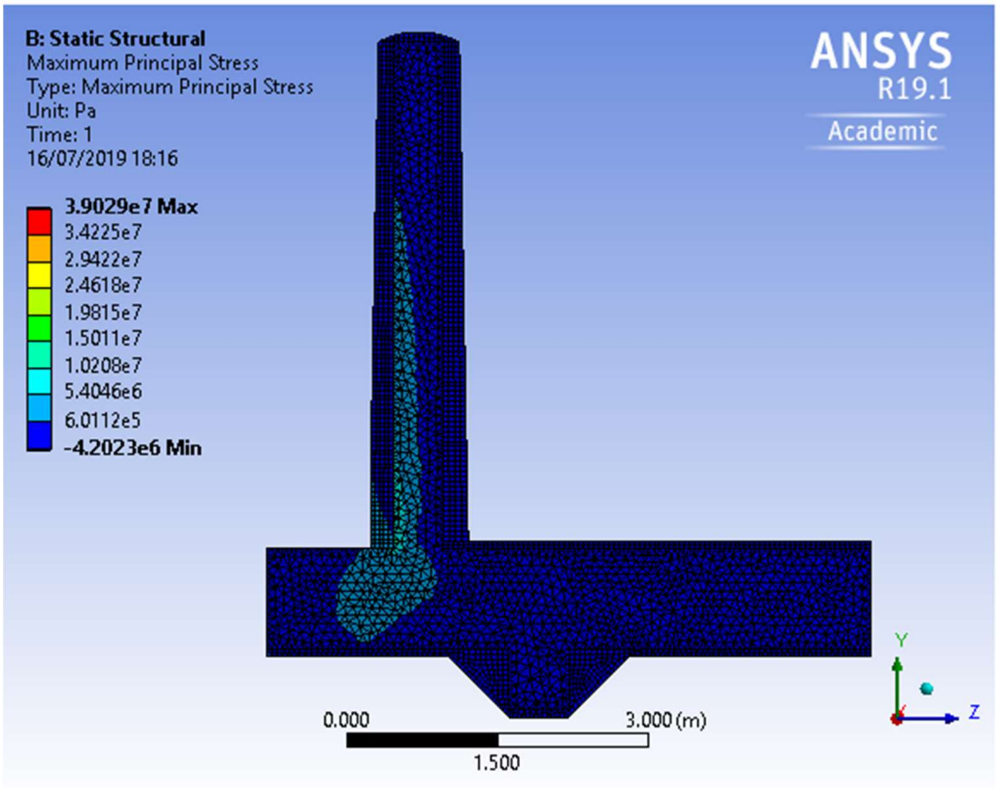

Figure 4.4.4 Maximum principal stress (new wall)

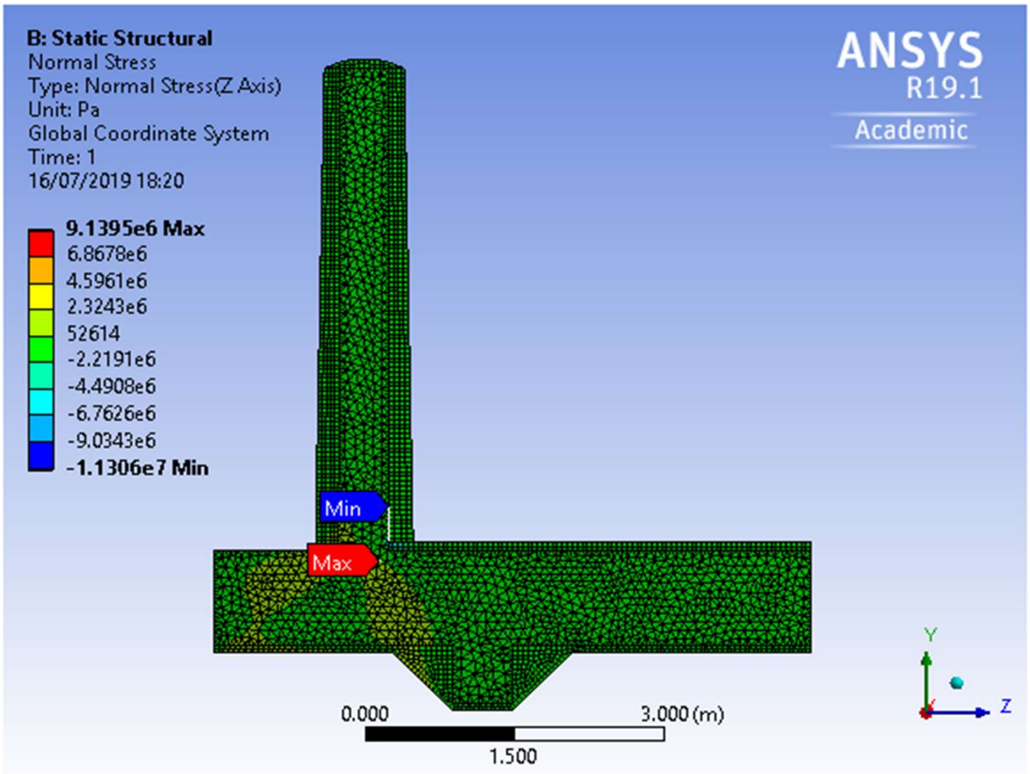

Figure 4.4.5 Normal stress (new wall)

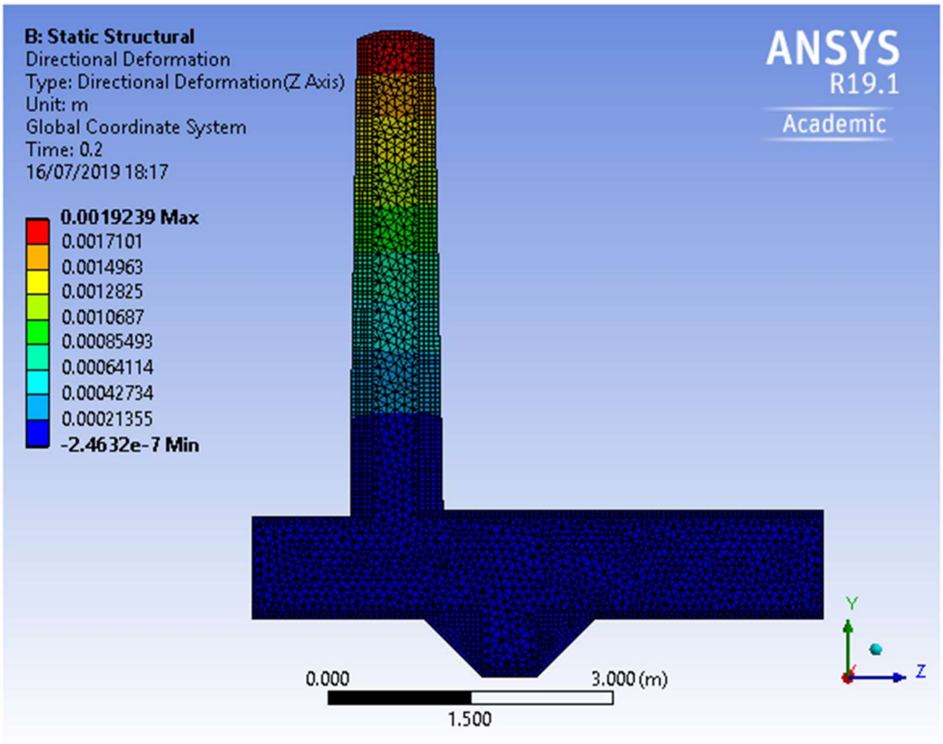

Figure 4.4.6 Displacement (new wall)

4.5. CFD analysis

In order to estimate the actual load on the wall due to the sea waves, a CFD (Computational Fluid Dynamics) analysis was run. The aim of the analysis is to get the pressure generated by the waves on the wall, therefore only the volume of fluid was modelled. As CFD software, OpenFOAM® (version 1906) has been used (OpenFOAM, 2019). It is an open source CFD toolbox. The software runs on a Linux system. It can also be run in other systems, e.g. Widows 10, by installing Bash on Ubunto on Windows. For this reason, the model is set and run by the command prompt Bash.

OpenFOAM has a lots of different "*tutorials*". Basically, they are examples already written of the most common cases. For each tutorial, there are sets of text files, written in C++, which define all the information required from the software in order to run the simulation (geometry, mesh, boundary conditions, initial values, calculation methods, equations, …).

For the case analysed in this study, the "*waterChannel*" and "*stokesII*" tutorials were used. Starting from the original files, they were edited in order to create the actual geometry and mesh, and also the boundary condition and the solution method files were edited according to the analysed problem. See Appendix A for some of the text files used for the analysis.

Each analysis run via OpenFOAM consists of a folder which contains 3 sub-folders where the text files must to be entered properly:

- *0* folder: contains all the scripts which define the initial condition (water and air domain, pressure, fluid velocity, viscosity, …);
- *Constant* folder: contains all the scripts which define the constant properties of the problem (gravity, turbulence properties, transport properties, mesh, …);
- *System* folder: contains all the scripts which define how to run the analysis (boundary condition assignments, solver properties, running time, …).

Once that all the files have been written by using a C++ language, it is possible to run the programme by command prompt. Hereby, a list of the most used prompt command:

- *blockMesh:* reads the *blockMeshDict* file and generates a folder with contains the meshed geometry files;
- *setFields:* generates files with the boundary conditions defined by scripts;
- *interFoam:* runs the analysis and generates a folder for each time-step which contains the result files;
- *touch <example_name>.foam:* generates a readable .foam file with the results.

The *.foam* file can be opened by a second software, ParaView®. ParaView® shows the results through a "classic" interface. Particularly, it can been run an animation which shows the motion of the waves along the time steps and the how the calculated properties (velocity magnitude, pressure, …) change along them.

Some of the boundary condition assigned and indicated into the text files in Appendix A, are here described:

- *zeroGradient:* also known as Neumann condition, assigns a null flow through a boundary (impermeable wall);
- *fixedValue:* also known as Dirichlet condition, assigns a fixed value at the boundary;

- *empty:* does not study the solution along the boundary where this condition is applied;

Moreover, it is common in CFD analysis to indicate with *inlet* the face where the flow comes from and with *outlet* the face where the flow goes out through.

4.5.1. Geometry of the problem

In order to get the pressure due to the waves on the portion of the wall under examination, the volume of fluid of only that part was modelled. The model considers an incoming flow from the inlet toward the outlet which fills the whole volume and generates a pressure on the wall side. The properties of the incoming flow depend from the bathymetry, from the wave geometric characteristics and from the wave theory adopted. For this reasons, theoretically, an initial coarse model should be created. This model should represents the bathymetry of the beach (250 m) and of the first 640 m (at least two times the wave length) of the sea bed, where the sea volume is filled with sea water. Moreover, the atmosphere domain should also be drawn over the sea level. At the "inlet" of this model should be generated waves with the geometric properties recorded during the storm and indicated in Table 4.1. For sake of simplicity, a simplified situation was considered. So, once the waves had propagated along the coarse model and had reached the "outlet" (which coincides with the inlet of the other model) all the flow properties were taken and used for the incoming flow at the inlet of the actual model.

The geometry of the volume of fluid at the sides of the wall is known since it is known the geometry of the wall, of the stairs next to it and of the car park (from the in situ survey and from the documents released by the Environment Agency, 2018). The geometry of the beach part was obtained from the LIDAR data (Channel Coastal Observatory, 2019), by using ArcMap while the bathymetry of the sea was obtained by the online tool EMODnet Bathymetry (2019). See Appendix A for some of the model properties, assignments and settings.

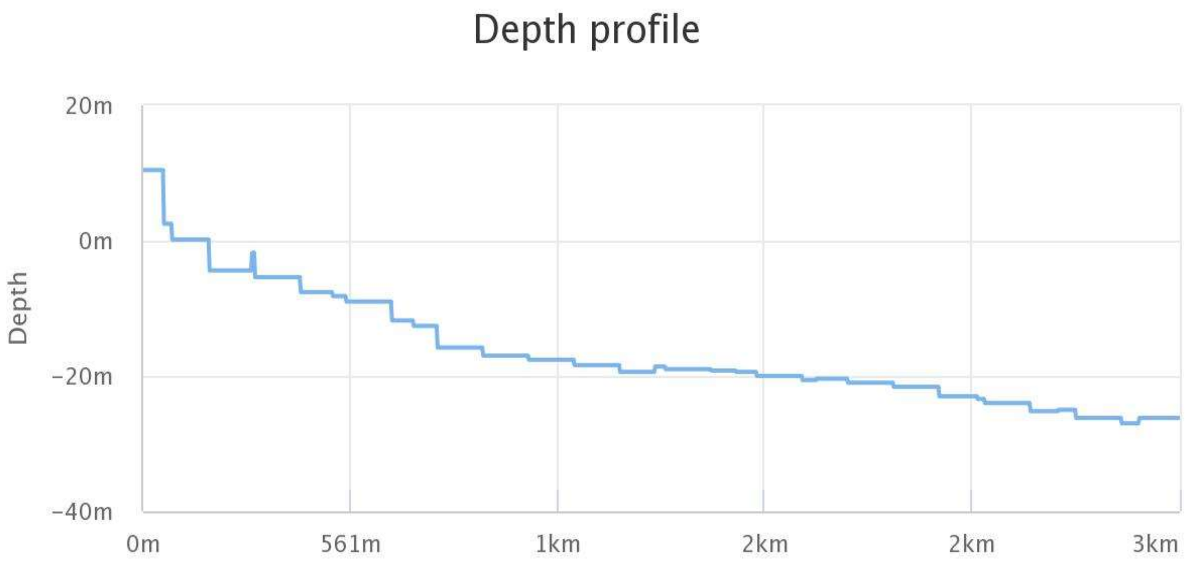

Figure 4.5.1. Bathymetry

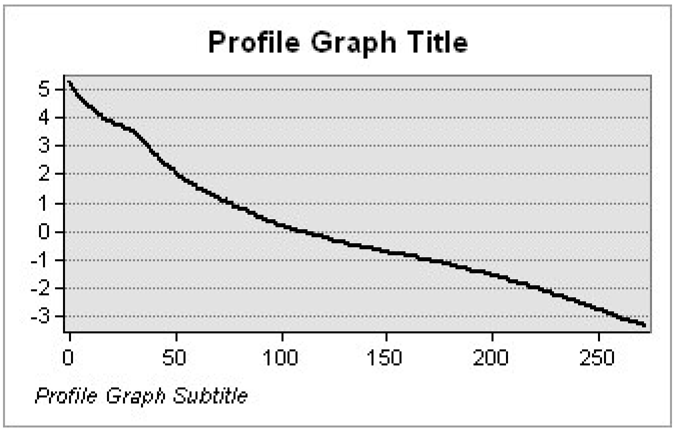

Figure 4.5.2. Beach profile

The geometry has been generated into the software by editing the *blockMeshDict* file. Vertices had to be defined in order that the first and second point generate the *x* axis, second and third point generate the *y* axis and fourth and fifth point generate the *z* axis. Numeration of vertices, faces and block must follow the right hand rule as indicated in the User Guide.

4.5.2. Wave theory

Le Mehaute diagram (Le Mehaute, 1969), in function of the wave height (H), the wave period (T), the seabed depth (h) and of the standard earth acceleration (g), indicates the wave theory which best model the wave scenario. For our case, Stokes 2nd order theory was used.

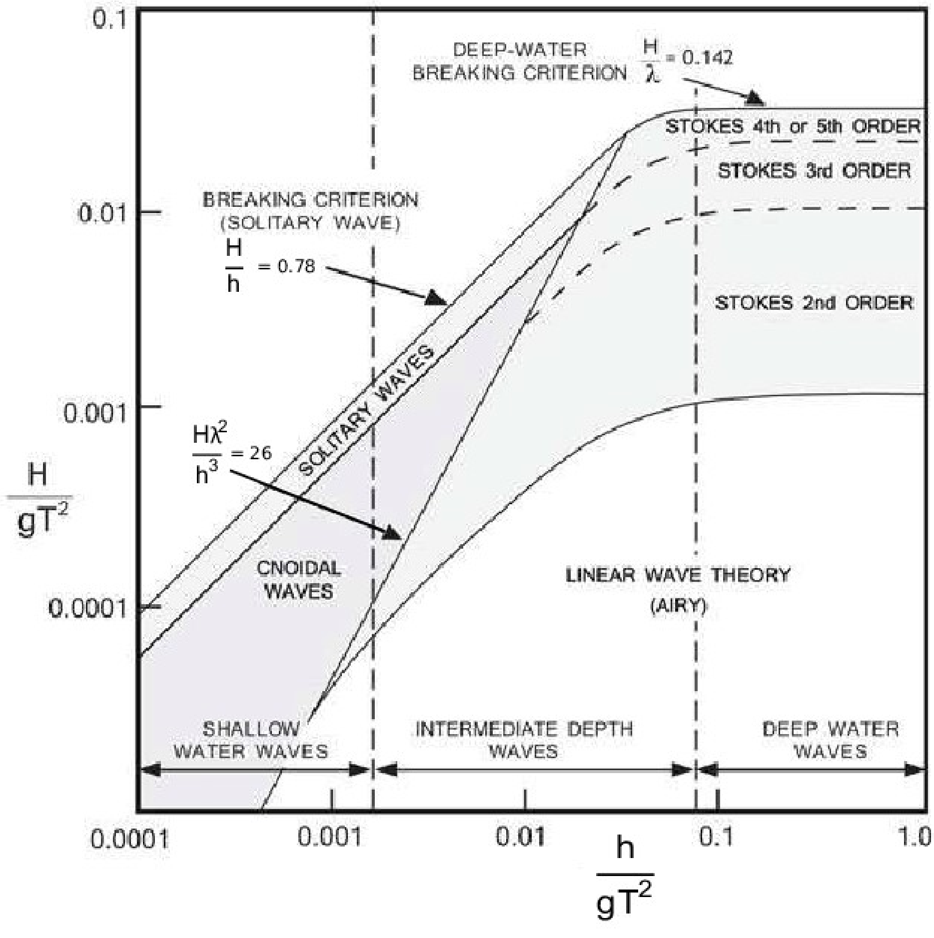

Figure 4.5.3. Le Mehaute's diagramm (Le Mehaute, 1969)

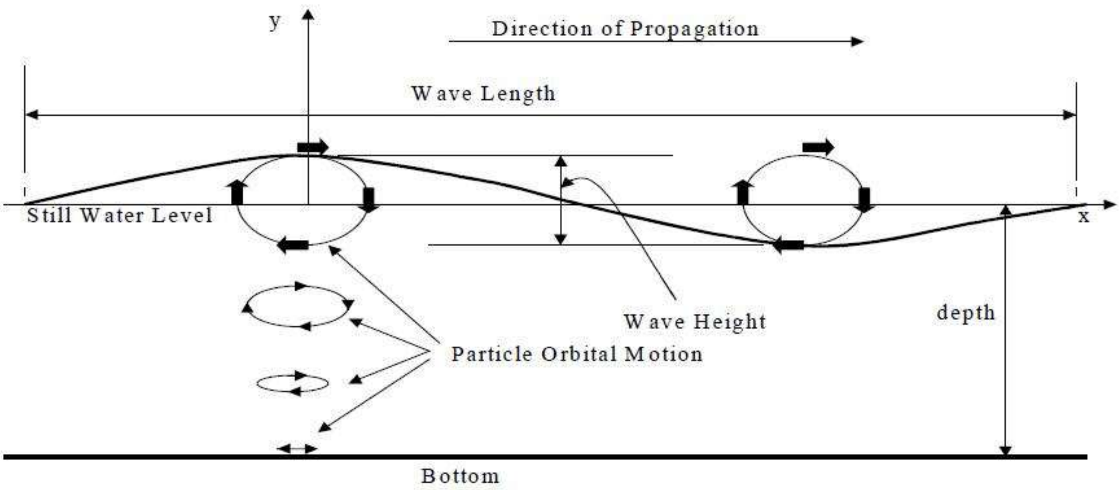

Figure 4.5.4.. Waves' geometric properties (Holmes, 2001)

A Stokes wave is a non-linear periodic surface wave (Wikipedia, 2019). The wave propagates over an inviscid fluid layer, with constant depth. According to Le Mehaute diagram, this theory works for waves on intermediate and deep water, as the case at the inlet of the coarse model, where the waves are considered to be generated. Particularly, the wave length must to be not large in comparison with the depth.

Stokes solved the problem of the unknown boundary condition, which must to be known in order to solve the wave differential equation (non-linear wave problem), by expanding all the potential flow quantities on a Taylor series around the still surface elevation. In this way, it is just necessary to define a quantity at the still surface elevation in order to define the boundary conditions. Therefore, Stokes defined a perturbation series (Stokes expansion) in terms of an unknown small parameter which can be solved sequentially. In function of the order of the perturbation expansion, there are different Stokes wave theories.

The velocity flow is described as the gradient of the velocity potential Φ:

$$u = \nabla \Phi \quad (26)$$

by assuming an incompressible flow, the velocity potential satisfies Laplace's Equation:

$$\nabla^2 \Phi = 0 \ (27)$$

In the case of a surface gravity wave, the boundary conditions for the free surface consist of a kinematic and a dynamic boundary condition. The boundary conditions are applied at the unknown free surface elevation $z = \eta(x, z, t)$. By considering a fixed constant elevation ($z = 0$), the flow field is expanded around this elevation by use of the Taylor series expansions. The expanded terms, are combined with the perturbation series:

$$\eta = \varepsilon\eta_1 + \varepsilon^2\eta_2 + \varepsilon^3\eta_3 + \cdots \ (28)$$

$$\Phi = \varepsilon\Phi_1 + \varepsilon^2\Phi_2 + \varepsilon^3\Phi_3 + \cdots \ (29)$$

$$u = \varepsilon u_1 + \varepsilon^2 u_2 + \varepsilon^3 u_3 + \cdots \ (30)$$

The perturbation $\boldsymbol{\varepsilon} \ll 1$ is proportional to the wave slope (ka). By skipping all the mathematical treatment, for Stokes 2nd order theory the following equations are got:

$$\Phi(x,z,t) = a\frac{\omega}{k}\frac{1}{sinh\ kh}\left\{cosh\ k(z+h)sin\ \vartheta + ka\frac{3cos\ \ \ 2h(z+h)}{8sinh^3\ kh}sin\ 2\vartheta\right\} +$$

$$-(ka)^2\frac{1}{2sinh\ 2kh}\frac{gt}{k} + o((ka)^3) \quad (31)$$

$$\eta(x,t) = a\ \left\{cos\ \vartheta + ka\frac{3-\sigma^2}{4\sigma^3}cos2\vartheta\right\} + o((ka)^3) \quad (32)$$

$$c = \frac{\omega}{k} = \sqrt{\frac{g}{k}\sigma} + O((ka)^2) \quad (33)$$

Where:

$$\sigma = tanh\ kh \quad (34)$$

$$\vartheta(x,t) = kx - \omega t \quad (35)$$

a is the first order wave amplitude: $a = \frac{H}{2}$

k is the angular wavenumber: $k = \frac{2\pi}{L}$

ω is the angular frequency: $\omega = \frac{2\pi}{T}$

Looking at Equation 32 it is possible to see how the free surface is the superposition of two different harmonics: the first harmonic (proportional to $\cos\vartheta$), which is the first order solution, and the second harmonic (proportional to $\cos 2\vartheta$), which is the second order solution. The second harmonic depends from the first one. Solution also contains the non-linear terms of the problem.

4.5.3. Results

Once the velocity field was got from the coarse model, by using the Stokes 2nd order theory, it was applied to the actual model and the following results were obtained. Looking at the "p_rgh" values (Figure 4.5.6)(which indicates the pressure over the wall minus the hydrostatic pressure, and so the additional load defined in Figure 4.3.1.), it is clear that the highest value (5.5 kPa), is quite smaller than the failure load found through the parametric analysis (30 kPa), and it is also smaller than the load which started generating the plastic areas (10 kPa). Hence, also for this second part of the wall, it can be said that the failure occurred because of the extended loading time during the storm. Moreover, it is quite likelihood that the degradation of the material and in general the wall state was worse of the one supposed in the analysis.

The velocity field, expressed in terms of flow rate, is here indicated for a wave period (14 s):

Table 4.5.1. Flow rate

Time[s]	**0,0**	**1,6**	**3,1**	**4,7**	**6,2**	**7,8**	**9,3**	**10,9**	**12,4**	**14,0**
Flow rate [m^3/s]	6,4	6,4	3,7	6,7	9,0	5,3	7,0	9,0	8,5	7,1

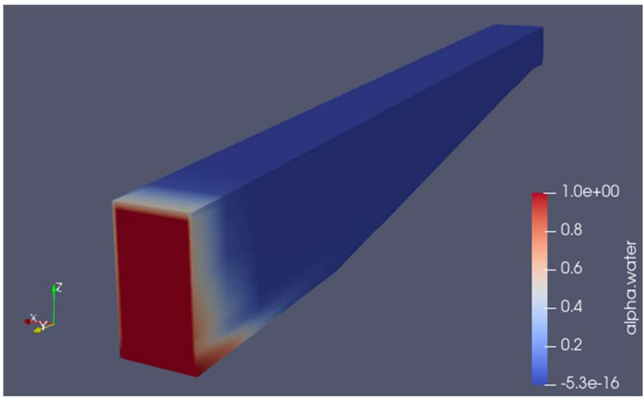

Figure 4.5.5.a Water domain, t=1s

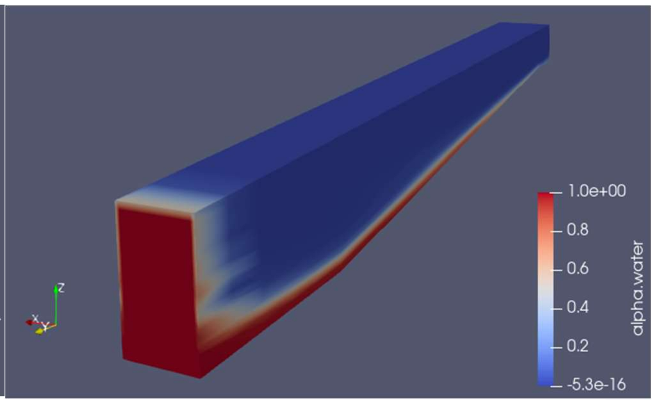

Figure 4.5.5.b Water domain, t=5s

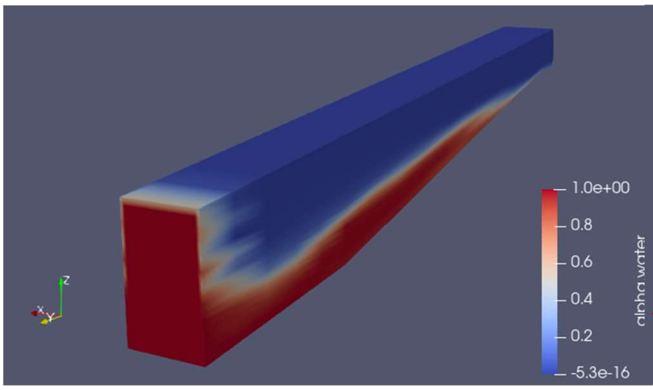

Figure 4.5.5.c Water domain, t=10s

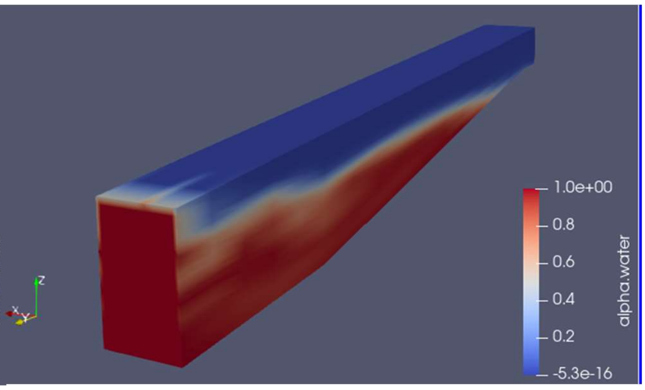

Figure 4.5.5.d Water domain, t=15s

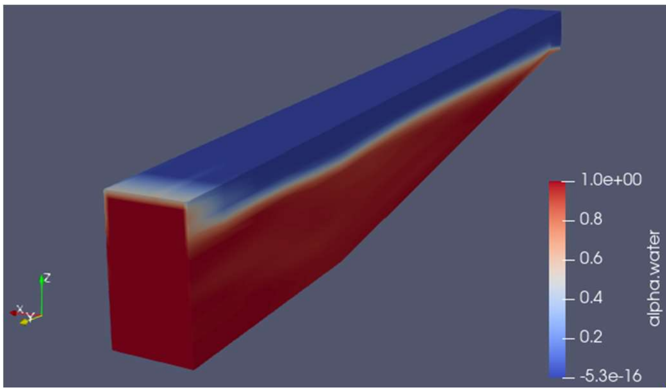

Figure 4.5.5.e Water domain, t=20s

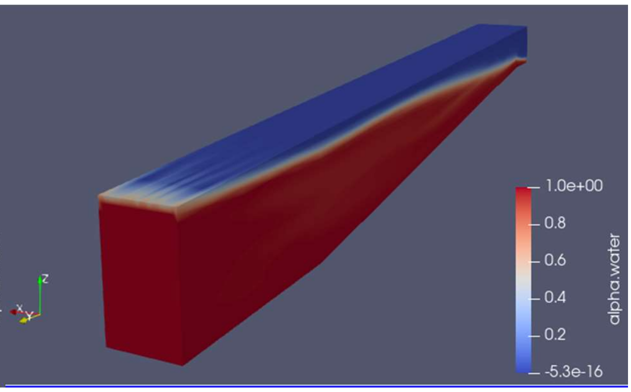

Figure 4.5.5.f Water domain, t=25s

Figure 4.5.5. shows the propagation of the waves into the domain. After 25 s, and so after less than 2 waves, the domain is already full of water (wave period is 14 s). Looking at Figure 4.5.6 it is worth observing how the pressure still increases after that the domain is full of water while it does not change while the first waves are filling the domain. Moreover, the pressure decreases once that the flow stops moving along the domain. The analysis was run for 84 s, hence 6 waves were considered. Obviously, due to the dynamic response of the wall, the dynamic wave load generates on the structure a higher pressure of the one here indicated.

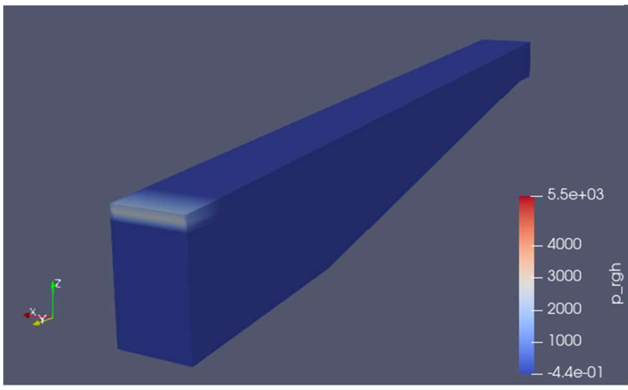

Figure 4.5.6.a. Total pressure minus the hydrostatic pressure, t=1s

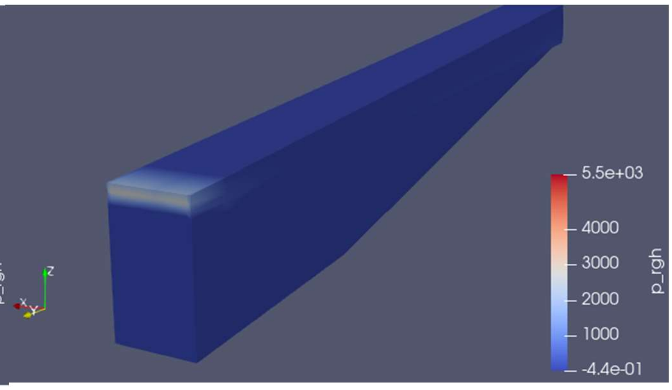

Figure 4.5.6.b. Total pressure minus the hydrostatic pressure, t=15s

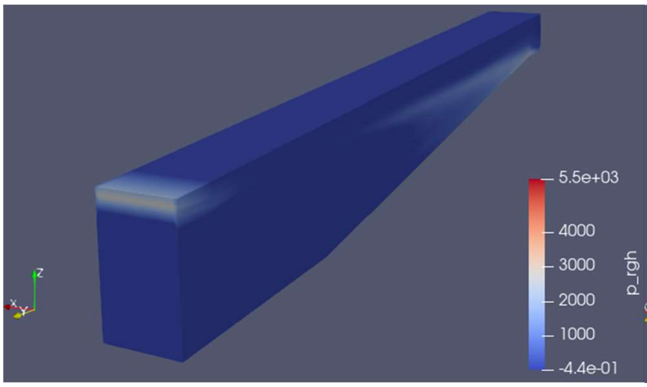

Figure 4.5.6.c. Total pressure minus the hydrostatic pressure, t=20s

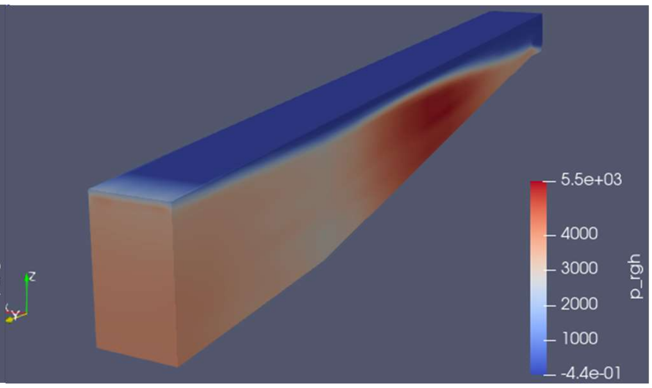

Figure 4.5.6.d. Total pressure minus the hydrostatic pressure, t=25s

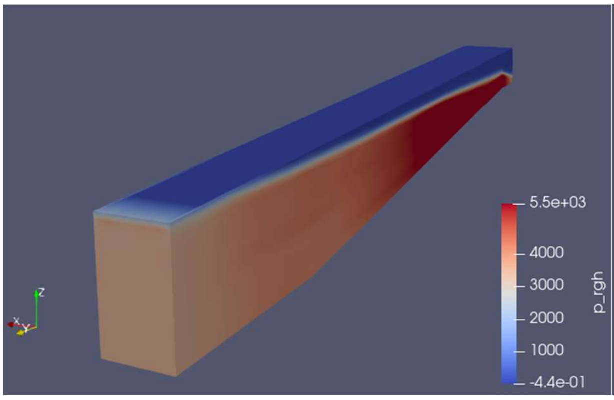

Figure 4.5.6.e. Total pressure minus the hydrostatic pressure, t=30s

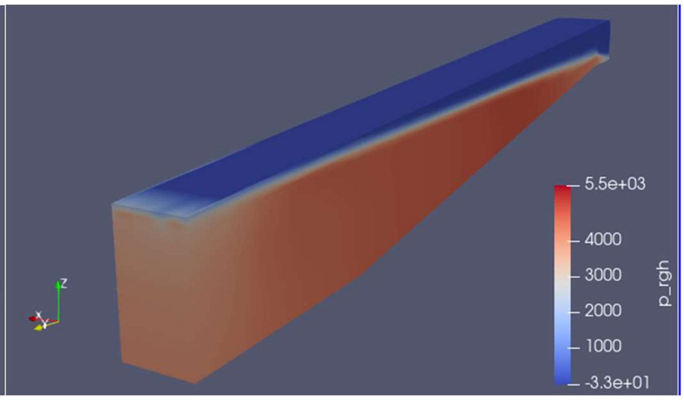

Figure 4.5.6.f. Total pressure minus the hydrostatic pressure, t=84s

5. Discussion and critical analysis

As it has been exposed in chapter 3 and 4, a failure mechanism was found for both the parts of the structure and both the structures were modelled and analysed.

5.1. The first part of the wall

For the first part of the wall, the damage to the Monkey Hut in 2014, were due to a progressive damage of the structure, which has been suffering the storm for one week. Same reason for the parapet. While no other damage were generated on the wall. On the contrary, the main structure has shown to be very stiff and it has been able to resist to the wave impact since today only showing an obvious degradation of the material. The degradation is not a big problem for the block, while it has almost destroyed the mortar layer. So, the main contribution in terms of strength is given by the blocks only.

The performance of the wall can be improved by increasing its stiffness using a shotcrete, as already has been done in a few parts. Moreover, also a cleaning and a restoration of the blocks should be useful: during the years a lots of small sea animals as well as the wave impact have damaged the block surface and also a superficial corrosion is diffused along the structure. As regards to the Monkey Hut, it should be more protected from the wave impact and the connection between it and the wall should be strong enough to resist to the wave impact. However it should also be elastic and ductile enough in order to permit the creation of a plastic hinge at the base and avoid the brittle failure of the connection. A good solution might be to insulate the Monkey Hut with an energy dissipation system.

Anyway, before of thinking to an intervention in order to protect the structure, it must be studied the behaviour of the wall for a future load scenario. A prediction of a future load and an analysis of the structure should be done taking into account a further degradation of the material.

It is worth observing that all the results got from this study are indicative. Lots of uncertain may have affected the results:

- FEM uncertain: even though the FEM model is the closest to the reality, it is anyway a model and all its solutions must be analysed. The model has shown to be stable to the small errors and convergent if the mesh resolution was increased. On the other hand, it is not possible to say if the model was accurate with complete certainty, since the actual result values have not been calculated with an appropriate theory. For further studies, a plate theory should be utilised in order to validate the model as discussed in part 3.5.1. Once that the model is validated, it will be possible to do a mesh sensitivity analysis with a bigger accuracy. The model can be created with a bigger accuracy as well. For example, the connection between the blocks can be modelled by springs with a stiffness equals to the stiffness of the mortar layer and in the same way the connection between the wall and the Monkey Hut. Moreover, if the interaction between the structure and the soil is required, the soil can be modelled as a volume element with its properties instead of using a support.
- Data uncertain: material properties were obtained with a very rough method. Eurocodes prescribed that a no-destructive method such as the Schmidt Hammer can be used in addition to other invasive tests but never as the only test for defining the material properties. In addition to this, using the Schmidt Hammer on rock in a

sea ambient, leads to other inaccuracies due to the method as discussed in part 1.2. Nevertheless, the found values have shown to be quite close to the expected values. For further studies, a set of appropriate tests should be performed in order to get the material properties, especially for the internal core of the wall at the moment almost completely unknown. Also the geometric data can be measured with a more accurate method.
- Load uncertain: Goda's Theory used for calculate the wave load is anyhow a theory and so approximations are inside. In addition, the wave information used for calculate the wave load, taken from the Channel Coastal Observatory, are not very accurate.

In the light of all these observations, this study is only a preliminary work with the intent to open the way to further studies about this before untreated argument.

5.2. The 3rd b part of the wall

For this last part of the wall it has been found that the asymmetric load, acting only on a triangular part of the wall, generated a shear strain between the two buttresses. The geometry and the material composition of the wall were so not able to resist under an exceptional event such as the one occurred in 2018. However, the wave load found by the CFD analysis is smaller than the failure load found with the parametric study. Hence, it can be said that the duration of the storm event and the structural degradation were the main causes of the failure. On the contrary, under the same failure load, the new reinforced concrete wall resisted. Even though the geometry of the top part is the same, the introduction of a big foundation made the wall stable respect the overturning and the use of the reinforced concrete increased a lot the strength of the structure in terms of shear, compression and tension. Moreover, also the connection of the wall with the remaining structure was improved as explained in paragraph 4. So, for this part, there are not further works to be suggested in order to protect the structure. Anyway, it might be useful studying the behaviour of the structure for a hypothetic future scenario.

As before, results are affected by uncertain:

- FEM uncertain: respect the previous case, for these models is easy to perform a validation and so to have an accurate result, as explained in paragraph 4.4. In the same way, the models have shown to be stable and convergent. The easy geometry of the wall also have not created problem for defining an accurate mesh. Nevertheless, the model can be improved either modelling the soil as a volume or modelling the connection with the remaining wall. Another approximation used in the model regards the masonry, modelled as a unique material. A model with blocks and mortar might be more accurate for further studies.
- Data uncertain: whereas in this case the geometry data were very accurate from the design drawing, the material data were unknown. No tests were performed on this part. Starting from the information available from the technical report, the material properties found with the Schmidt Hammer in a close area have been assumed, and so all the considerations made for the previous model are still valid.
- Load uncertain: this is the main uncertain for the model in analysis. No theories have been found in literature in order to compute the wave load for this scenario. Indeed, the aim of this part of the work was not to analyse the structure, but to get an order of the failure load and to understand the kind of failure of the structure. The wave load

got by the CFD analysis is anyway affected by uncertain: CFD analysis has the same uncertain described for the FEM analysis, moreover the model created in this phase of the work contains too simplification.

In the light of all these observations, also this study is a starting point for further analysis. A more accurate CFD analysis may give better results.

Conclusion

The Portreath Harbour wall is today what remains of the vital Portreath Harbour, one of the busiest harbours of Cornwall in the past. The structure was damaged during a storm in 2014, which washed away the iconic Monkey Hut at the top of the wall, and again in 2018 when storm Eleanor completely destroyed the toe of the structure. Repair works were undertaken during the years, which rebuilt the Monkey Hut, the destroyed part of the wall and increased the stiffness of the structure. Part of the information about the repair works were obtained through the different companies and also historical information were gotten. The geometry of the wall and the material properties were obtained by a field trip. Particularly, a Schmidt Hammer test was used for calculating the material properties and results were interpreted according to an appropriate literature. Information was integrated with the ones obtained from the LIDAR data.

Once all the information was collected, FEM models were created for both the damaged parts of the wall. For the first part a 3D model was created considering different blocks connected by a mortar layer. Results were compared with a homogeneous model. In this part it was found that the problem was the progressive damage of the connection between the Monkey Hut and the wall. Wave load was calculated by means of Goda's theory. Another 3D model was created for the destroyed part at the toe of the structure by considering a unique material. By a parametric analysis the failure load was found and then used for the verification of the rebuilt reinforced concrete wall, modelled through a 2D model. Shear and overturning failure mechanisms were found for the old wall, while the new one has not exhibited these problems. The actual wave load was subsequently computed and it was found a smaller load than the failure one. Hence, the progressive structural degradation and the long duration of the storm were the main failure causes. Results were discussed and critically analysed and a summary is given in Chapter 5. In conclusion, since tensile stresses are already close to the tensile strength of the material, it can be assumed that at some point (due to a progressive damage) the material cracked. Once the material cracked, and the material tensile strength started decreasing, the water which filled the fissure started spreading the crack width and as consequence the internal pressure increased too (according to the studies discussed in Chapter 1). Hence, the structural strength has been decreasing while the internal pressure has been increasing during the storms till the structures failed.

The results obtained from the present study are approximate and they are the base for further works. A future work regards a progressive damage analysis of the connection between the Monkey Hut and the wall in order to get both the fatigue failure of the structure and the degradation law of the material properties under periodic wave loading. For this purpose, it can be modelled a damage in the mortar connection by reducing the material properties. ANSYS has also an appropriate tool for fatigue analysis. For the other model, a specific and very accurate CFD analysis is required in order to get a realistic velocity field. Moreover, a structural analysis of the wall under the dynamic wave load may show a different result due to the structural dynamic response. The relative displacement between block and mortar can be better seen by using a discrete element model (DEM) instead of a FEM one. Anyway, cohesion and friction between blocks and mortar can be better modelled with appropriate laws also in the FEM model. An accurate way of modelling the structure may be to connect the blocks by springs with the mortar stiffness. The structure can be verified for a future load scenario in order to define a protection work.

Acknowledgements

I wish to acknowledge all the people who have helped me throughout the writing of this dissertation: prof. Alison Raby, for presenting to me this challenging research project and for following and suggesting me, week by week; Dr Darshana Dassanayake for introducing me into the interesting coastal engineering world, for all the help in the wave load calculation and for giving me a big job opportunity; prof. Long-yuan Li for his help and his experience in the FEM and in the structural field; prof. Cecilia Surace for encouraging, and accepted to follow, my experience abroad. A special thanks also to Eng. Rinto Roy, for the huge help with the CFD analysis.

I would also like to thank everyone who has somehow given a precious contribution to my work: Nick Ely from the Environment Agency, for providing all the drawings and the technical report of the new rebuilt reinforced concrete wall; Colin Higgs from the Portreath Harbour Association, for providing all the historical documents regard the structure; Mr Tony Tapp from the Brunel Laboratory, for providing all the instruments used during the field trip and for explaining to me the Schmidt Hammer working.

In addition, many thanks to my family and to everyone who has been closest to me during the hardest, but the most amazing, experience of my life.

Thank you all,

Luigi

APPENDIX A

- **A1. Geometry and mesh**

```
/*--------------------------------*- C++ -*----------------------------------*\
| =========                 |                                                 |
| \\      /  F ield         | OpenFOAM: The Open Source CFD Toolbox           |
|  \\    /   O peration     | Version:  v1906                                 |
|   \\  /    A nd           | Web:      www.OpenFOAM.com                      |
|    \\/     M anipulation  |                                                 |
\*---------------------------------------------------------------------------*/
FoamFile
{
    version     2.0;
    format      ascii;
    class       dictionary;
    object      blockMeshDict;
}
// * * * * * * * * * * * * * * * * * * * * * * * * * * * * * * * * * * * * * //
scale   1;
vertices
(
    (0 0 0) // 0
    (2.4 0 0) // 1
    (0 1.61 0) //2
    (2.4 1.61 0) // 3
    (0 20.61 -3.2) // 4
    (2.4 20.61 -3.2) // 5
    (0 27.9 -3.52) //6
    (2.4 27.9 -3.52) // 7
    (0 0 1.7) // 8
    (2.4 0 1.7) // 9
    (0 1.61 1.63) //10
    (2.4 1.61 1.63) // 11
    (0 20.61 0.8) // 12
```

```
    (2.4 20.61 0.8) // 13
    (0 27.9 0.48) //14
    (2.4 27.9 0.48) //15
 );
 blocks
 (
    hex (0 1 3 2  8  9 11 10) (20  5 20) simpleGrading (1 1 1)
    hex (2 3 5 4 10 11 13 12) (20 10 20) simpleGrading (1 1 1)
    hex (4 5 7 6 12 13 15 14) (20  5 20) simpleGrading (1 1 1)
 );
edges
 (
 );
boundary
 (
    inlet
    {
       type patch;
       faces
       (
                    (6 7 15 14)
       );
       }
    walls
    {
       type wall;
       faces
       (
                    (0 1 3 2)
                    (4 5 7 6)
                    (2 3 5 4)
```

```
            (3 5 13 11)
            (0 2 10 8)
            (2 4 12 10)
            (5 7 15 13)
            (4 6 14 12)
            (1 3 11 9)
        );
    }
    outlet
    {
        type patch;
        faces
        (
                        (0 1 9 8)
        );
    }
    atmosphere
    {
        type patch;
        faces
        (
            (8  9 11 10)
            (10 11 13 12)
            (12 13 15 14)
        );
    }
);
// ************************************************************************* //
```

- **A2. Velocity field**

```
/*--------------------------------*- C++ -*----------------------------------*\
| =========                 |                                                 |
| \\      /  F ield         | OpenFOAM: The Open Source CFD Toolbox           |
|  \\    /   O peration     | Version:  v1906                                 |
|   \\  /    A nd           | Web:      www.OpenFOAM.com                      |
|    \\/     M anipulation  |                                                 |
\*---------------------------------------------------------------------------*/
```

FoamFile

{

version 2.0;

format ascii;

class volVectorField;

object U;

}

// * //

dimensions [0 1 -1 0 0 0 0];

internalField uniform (0 0 0);

boundaryField

{

inlet

{

type flowRateInletVelocity;

volumetricFlowRate table ((0 6.4094) (1.56 6.4483) (3.11 3.7089) (4.67 6.6722) (6.22 9.0222) (7.78 5.2797) (9.33 9.7265) (10.89 9.0114) (12.44 8.5172) (14 7.1364)

(15.56 6.4094) (17.11 6.4483) (18.67 3.7089) (20.22 6.6722) (21.78 9.0222) (23.33 5.2797) (24.89 9.72651) (26.44 9.0114) (28 8.5172) (28.1 7.1364)

(28.2 6.4094) (29.56 6.4483) (31.11 3.7089) (32.67 6.6722) (34.22 9.0222) (35.78 5.2797) (37.33 9.7265) (38.89 9.01142) (40.44 8.5172) (42 7.1364)

(42.1 6.4094) (43.55 6.4483) (45.11 3.7089) (46.67 6.6722) (48.22 9.0222) (49.78 5.2797) (51.33 9.7265) (52.89 9.0114) (54.44 8.5172) (56 7.1364)

(56.1 6.4094) (57.56 6.4483) (59.11 3.7089) (60.67 6.6722) (62.22 9.0222) (63.78 5.2797) (65.33 9.7265) (66.89 9.0114) (68.44 8.5172) (70 7.1364)

```
                         (70.1 6.4094) (71.56 6.4483) (73.11 3.7089) (74.67 6.6722)
(76.22 9.0222) (77.78 5.2797) (79.33 9.7265) (80.89 9.0114) (82.44 8.5172) (84
7.1364));
    }
    walls
    {
        type            noSlip;
    }
    atmosphere
    {
        type            pressureInletOutletVelocity;
        value           uniform (0 0 0);
    }
    outlet
    {
        type            inletOutlet;
        inletValue      uniform (0 0 0);
        value           $internalField;
    }
}
// ************************************************************************* //
```

- **A3. Turbolence properties (RAS model)**

```
/*--------------------------------*- C++ -*----------------------------------*\
| =========                 |                                                 |
| \\      /  F ield         | OpenFOAM: The Open Source CFD Toolbox           |
|  \\    /   O peration     | Version:  v1906                                 |
|   \\  /    A nd           | Web:      www.OpenFOAM.com                      |
|    \\/     M anipulation  |                                                 |
\*---------------------------------------------------------------------------*/
FoamFile

{
    version     2.0;
    format      ascii;
    class       volScalarField;
    object      k;
}
// * * * * * * * * * * * * * * * * * * * * * * * * * * * * * * * * * * * * * //
dimensions      [0 2 -2 0 0 0 0];
internalField   uniform 0.0001;
boundaryField
{
    inlet
    {
        type            fixedValue;
        intensity       0.05;
        value           $internalField;
    }
    walls
    {
        type            kqRWallFunction;
        value           $internalField;
    }
    ".*"
    {
        type            inletOutlet;
        inletValue      $internalField;
        value           $internalField;
    }
}
// ************************************************************************* //

FoamFile
{
    version     2.0;
    format      ascii;
    class       volScalarField;
    location    "0";
    object      nut;
```

```
}
// * * * * * * * * * * * * * * * * * * * * * * * * * * * * * * * * * * * * //
dimensions      [0 2 -1 0 0 0 0];
internalField   uniform 0;
boundaryField
{
   walls
   {
      type          nutkWallFunction;
      value          uniform 0;
   }
   ".*"
   {
      type          calculated;
      value          uniform 0;
   }
}
// ************************************************************************* //

FoamFile
{
   version     2.0;
   format      ascii;
   class       volScalarField;
   object      omega;
}
// * * * * * * * * * * * * * * * * * * * * * * * * * * * * * * * * * * * * //
dimensions      [0 0 -1 0 0 0 0];
internalField   uniform 0.003;
boundaryField
{
   inlet
   {
      type          fixedValue;
      value          $internalField;
   }
   walls
   {
      type          omegaWallFunction;
      value          $internalField;
   }
   ".*"
   {
      type          inletOutlet;
      inletValue     $internalField;
      value          $internalField;
   }
}
```

```
// ************************************************************************* //

FoamFile
{
   version     2.0;
   format      ascii;
   class       volScalarField;
   object      s;
}
// * * * * * * * * * * * * * * * * * * * * * * * * * * * * * * * * * * * * * //

dimensions      [0 0 0 0 0 0 0];

internalField   uniform 0;

boundaryField
{
   inlet
   {
      type          fixedValue;
      value          uniform 0;
   }
   walls
   {
      type          zeroGradient;
   }
   outlet
   {
      type          zeroGradient;
      value          uniform 0;
   }
   atmosphere
   {
      type          inletOutlet;
      inletValue     uniform 0;
      value          uniform 0;
   }
}
// ************************************************************************* //
```

- **A4. Pressure**

```
/*--------------------------------*- C++ -*----------------------------------*\
| =========                 |                                                 |
| \\      /  F ield         | OpenFOAM: The Open Source CFD Toolbox           |
|  \\    /   O peration     | Version:  v1906                                 |
|   \\  /    A nd           | Web:      www.OpenFOAM.com                      |
|    \\/     M anipulation  |                                                 |
\*---------------------------------------------------------------------------*/
FoamFile
{
    version     2.0;
    format      ascii;
    class       volScalarField;
    object      p_rgh;
}
// * * * * * * * * * * * * * * * * * * * * * * * * * * * * * * * * * * * * * //

dimensions      [1 -1 -2 0 0 0 0];
internalField   uniform 0;
boundaryField
{
    atmosphere
    {
        type            totalPressure;
        p0              uniform 0;
    }
    ".*"
    {
        type            fixedFluxPressure;
        value           uniform 0;
    }
}
// ************************************************************************* //
```

- **A5. Fluid properties**

```
/*--------------------------------*- C++ -*----------------------------------*\
| =========                 |                                                 |
| \\      /  F ield         | OpenFOAM: The Open Source CFD Toolbox           |
|  \\    /   O peration     | Version:  v1906                                 |
|   \\  /    A nd           | Web:      www.OpenFOAM.com                      |
|    \\/     M anipulation  |                                                 |
\*---------------------------------------------------------------------------*/
FoamFile

{
    version     2.0;
    format      ascii;
```

```
    class       dictionary;
    location    "constant";
    object      transportProperties;
}
// * * * * * * * * * * * * * * * * * * * * * * * * * * * * * * * * * * * * * //
phases (water air);
water
{
    transportModel  Newtonian;
    nu              1e-06;
    rho             1000;
}
air
{
    transportModel  Newtonian;
    nu              1.48e-05;
    rho             1;
}
sigma           0.07;
// ************************************************************************* //
```

List of References

Anastasaki, E., Latham, J.-P., & Xiang, J. (2015). Numerical modelling of armour layers with reference to Core-Loc units and their placement acceptance criteria. Ocean Engineering , 204-2018.

ANSYS, (2019). CONT174. [Online] Available at: https://www.sharcnet.ca/Software/Ansys/16.2.3/en-us/help/ans_elem/Hlp_E_CONTA174.html

ANSYS, (2019). SOLID186. [Online] Available at: https://www.sharcnet.ca/Software/Ansys/16.2.3/en-us/help/ans_elem/Hlp_E_SOLID186.html

ANSYS, (2019). Structural analysis for every application and experience level. [Online] Available at: https://www.ansys.com/en-gb/products/structures

ANSYS, (2019). SURF154. [Online] Available at: https://www.sharcnet.ca/Software/Ansys/17.0/en-us/help/ans_elem/Hlp_E_SURF154.html

Archive, The Quarterly Journal for British Industrial and Transport History. 1st March 1994 (ISBN 1352-7991).

BBC, (2018). *Portreath: The village at the centre of the storm*. [online] Available at: https://www.bbc.co.uk/news/uk-england-cornwall-42555005

Bird, P.A.D., Crawford, A.R., Hewson, P.J., Bullock, G.N. (1998). An instrument for field measurement of wave impact pressures and seawater aeration. Coastal Engineering, 103-122.

Bredmose, H., Bullock, G.N., Hogg, A.J. (2015). Violent breaking wave impacts. Part 3: Effects of scale and aeration. J. Fluid. Mech., vol. 765, pp 82-113

Bredmose, H., Peregrine, D.H., Bullock, G.N. (2009). Violent braking wave impacts. Part 2: modelling the effect of air. J. Fluid. Mech., vol. 641, pp. 389-430

British Oceanographic Data Centre, 2019. [Online] Available at: https://www.bodc.ac.uk/data/hosted_data_systems/sea_level/uk_tide_gauge_network/processed/

British Railway Journal Number 33. (Wild Swan Publications Didcot 1990).

Bullock, G.N., Crawford A.R., Hewaon, P.J., Walkden M.J.S., Bird P.A.D. (2001). The influence of air and scale on wave impact pressures. Coastal Engineering, 191-312.

Bullock, G.N., Obhrai, C., Peregrine, D.H., Bredmose H. (2007). Violent breaking wave impacts. Part 1: Results from large-scale regular wave tests on vertical and sloping walls. Coastal Engineerin, 602-617

Carpinteri, A. (1993). *Scienza delle costruzioni 1.* 2nd ed. Bologna: Pitagora Editrice srl

Channel Coastal Observatory, 2019. [online] Available at: https://www.channelcoast.org/

CORMAC, (2018). *Portreath harbour wall recovery continues***.** [Online] Available at: https://www.cormacltd.co.uk/latest-news/2018/january-2018/portreath-harbour-wall-recovery-continues/

Cornwall Council, (2014). *The winter storms of 2014: How Cornwall fared*. [online] Available at: https://www.cornwall.gov.uk/media/9058197/Cornwall-storms-2014.pdf

Cornwall Live, (2018). *Portreath harbour wall destroyed by Storm Eleanor near the Waterfront Inn.* [online] Available at: https://www.cornwalllive.com/news/cornwall-news/portreath-harbour-wall-destroyed-storm-1003331

EMODnet Bathymetry, (2019). [online] Available at: https://portal.emodnet-bathymetry.eu/

Environment Agency, (2018). *Portreath sea wall repair work starts.* [Online] Available at: https://www.gov.uk/government/news/portreath-sea-wall-repair-work-starts
Environment Agency, (2018). *Portreath Sea Wall Trial Hole Report.* ENV0001457C-MMD-XX-00-RP-GT-0108001-S2-P01-A0800-EA3-LOD3

Environment Agency, (2018). ENV0001457C-MMD-DW-3AS-DR-C-0213002 - *Reinforcement Layout;* ENV0001457C-MMD-DW-3AS-DR-C-0213004 - *Wall General Arrangement;* ENV0001457C-MMD-DW-3AS-DR-C-0213006 - *Details (Sheet 2 of 2);* ENV0001457C-MMD-XX-00-RP-GT-0108001-S2-P01-A0800-EA3-LOD3 - *Portreath Sea Wall Trial Hole Report.*

Goda, Y., (2000). *Random seas and design of maritime structures.* 1st ed. Singapore: World Scientific

Goudie, A. S., (2006). The Schmidt Hammer in geomorphological research. *Progress in Physical Geography: Earth and Environment, 30(6), 703-718*

Guo, L., Latham, J.-P., & Xiang, J. (2015). Numerical simulation of breakages of concrete armour units using a three-dimensional fracture model in the context of the combined finete-discrete element method. Computers and Structeres , 117-142.

Hack, H., Huisman, M., (2002). Estimating the intact rock strength of a rock mass by simple means. *Proceeding of the 9th congress of the International Association for Engineering Geology and the Environment: Engineering geology for the developing countries,* 1971-1977

Historical Atlas of South West England, (1999). University of Exter press, ISBN 0 85989 434 7

Holmes, P.,(2001). *Coastal defence systems I, Chapter 5.* CDCM Professional Training Programme

ICE, (2016). *Portreath Finger Pier Repairs Project.* [Online] Available at: https://www.ice.org.uk/ICEDevelopmentWebPortal/media/Documents/Regions/UK%20Regions/portreath-finger-pier-pepairs-project.pdf

Katz, O., Reches, Z., Roegiers, J-C., (2000). Evaluations of mechanical properties using a Schmidt Hammer. *International Journal of Rock Mechanics and mining science 37,* 723-728

Latham, J.-P., A., Mindel, J., Xiang, J., Guises, R., Garcia, X., Pain, C., Gorman, G., Piggot, M. & Munjiza A. (2008). Coupled FEMDEM/Fluids for coastal engineers with special reference to armour stability and brakage. Geomechanics and Geoengineering: An International Journal , 4:1, 39-53, DOI: 10.1080/17486020902767362.

Latham, J.-P., Munjiza, A., Mindel, J., Xiang, J., Guises, R., Garcia, X., Pain, C., Gorman, G., Piggot, M. (2008). Modelling of massive particulates for breakwater engineering using coupled FEMDEM and CFD. Particuology 6, 572-583.

Le Mehaute, B. (1969). Introduction to Hydrodynamics and Water Waves, Vol.1- Fundamentals, Vol. 2- Water Wave Theories. Volume 118 of Us Dept. of Commerce ESSA technical Report Erl

Loraux, C. (2013). Comportement structural des phares en mer. Rapport de synthese du Projet de Master de C. Loraux sous la direction du Dr. E. Denarié, MER & du Prof. Dr. E. Bruhwiler, Ecole Polytechnique Federale de Lausanne.

McCall, B. Concrete Test Hammer N, operating instruction. *Proceq*

Min, K.B., Jing, L., (2003). Numerical determination of the equivalent elastic compliance tensor for fractured rock masses using the distinct element method. *Rock Mechanics and Mining Sciences 40,* 795-816

Mol, L., (2014). Measuring rock hardness in the field. *Geomorphological Techniques, Chap. 1, Sec. 3.2*

OpenFOAM, (2019). *User Guide, version 7.* [Online] Available at: http://foam.sourceforge.net/docs/Guides-a4/OpenFOAMUserGuide-A4.pdf

Pappas, A., D'ayala, D., Antonini, A., Brownjohn, J., Raby, A., (2017). Numerical modelling of Fastnet Lighthouse based on experimental dynamic identification. *71st RILEM Week & ICAMS*

Portreath Harbour Association, (2019). *Harbour History*. [online] Available at: http://www.portreath-harbour.org/harbour-history/

Portreath Harbour Association, (2019). *Photo Gallery.* [Online] Available at: http://www.portreath-harbour.org/photo-gallery/

R. Lancellotta, J. Calavera, (2016). *Foundations.* McGraw-Hill Education

Viles, H., Goudie, A., Grab, S., Lalley, J., (2011). The use of the Schmidt Hammer and Equotip for rock hardness assessment in geomorphology and heritage science: a comparative analysis. *Earth Surface Processes and Landforms 36, 320-333*

Wikipedia, (2019). *Stokes wave.* [online] Available at: https://en.wikipedia.org/wiki/Stokes_wave

Wolter, G., Muller, G., Bullock, G., Obhrai C., Peregrine H., Bredmose H. (2004). Field and large scale model tests of wave impact pressure propagation into cracks. Coastal Engineering, 4027-4039

YouTube, 2019. *Portreath loss update*. [online] Available at: https://www.youtube.com/watch?v=4StaUYrMJmI